ASYMMETRIC MULTIPLE QUANTUM WELL LIGHT SOURCES FOR OPTICAL COHERENCE TOMOGRAPHY

ASYMMETRIC MULTIPLE QUANTUM WELL LIGHT SOURCES FOR OPTICAL COHERENCE TOMOGRAPHY

By

JINGCONG WANG, B. Sc, M.SC, M.A.Sc.

A Thesis
Submitted to the School of Graduate Studies
in Partial Fulfillment of the Requirements
for the Degree
Doctor of Philosophy

McMaster University

DOCTOR OF PHILOSOPHY MCMASTER UNIVERSITY

(Engineering Physics) Hamilton, Ontario

TITLE: Asymmetric Multiple Quantum Well Light Sources for Optical Coherence Tomography

AUTHOR: Jingcong Wang, B. Sc. (Northeast Normal University of China)
M. Sc. (University of Science and Technology of China)
M. A. Sc. (McMaster University)

SUPERVISOR: Professor D. T. Cassidy

NUMBER OF PAGES: xi, 93

ABSTRACT

Asymmetric multiple quantum wells (AMQWs) can provide broad and flat gain spectra. Broadly tunable diode lasers can be realized with AMQW active regions and without the need for antireflection coatings on cleaved facets.

This thesis reports the application of AMQW broadly tunable lasers with uncoated facets for Fourier domain and synthesized optical coherence tomography (OCT). A depth resolution of 13 μm in air was obtained with a test bed OCT system that used diffractive optical elements, short external cavities, and AMQW InGaAsP/InP broadly tunable lasers as the light sources for the Fourier domain and the synthesized OCT measurements. The centre wavelengths of the broadly tunable sources were 1550 nm and the tunable ranges were ≤ 117 nm.

The features of broad and flat gain spectra of AMQWs also make AMQWs ideal candidates for broad spectral width superluminescent diodes (SLDs). 1300 nm AMQW InGaAsP/InP SLDs were designed and fabricated for application to time domain OCT. For the design of the active region, it was found by simulation of gain and the comparison of two growths that the transition carrier density (TCD) has to be reasonably high to achieve high power SLDs. A transfer matrix method was used to solve for the modes of planar optical waveguides with arbitrary layers and the thicknesses of these layers were optimized with a Marquardt nonlinear fitting method. With the optimization of the optical waveguide and with AMQWs with high TCDs, the output power of SLDs could reach 2 mW with > 90 nm spectral width. It is shown by time domain OCT measurements that the depth resolution of the OCT measurements could reach 7.85 μm in air with double section SLDs.

Two dimensional OCT images of a glass cover slip were built with the imageSC function in Matlab™. Image enhancement with blind/not-blind deconvolution was performed based on the measured point spread function (PSF) of the OCT setup. A

Richardson-Lucy algorithm was used as the blind deconvolution method and a not-blind version of a Jansson-Van Cittert method was used.

ACKNOWLEDGEMENTS

I would like to express my gratitude to my supervisor, Dr. Daniel T. Cassidy, for his guidance and support throughout the course of this work. I would especially thank Dr. Zhilin Peng for his training in the cleanroom processing for my SLD. Thank Dr. Brad J. Robinson for the MBE growth of my sample and Maxime Poirier who works in CMC for his assistant in my mask design. I would thank Dr. Doug Bruce for my near field, PL peak measurement of my devices and the valuable discussions on my research. Ms. Doris V. Stevanovic and Graham Pearson are always happy to offer help whenever needed either in the training or providing apparatus. I really appreciate it.

I would also like to thank my labmates Hesham M. Enshasy and Ferdous K. Khan for the valuable discussions and the pleasures we have had together.

My parents especially my mom deserve the most thanks of all. They take care of my family and provide me support as much as they can during my Ph.D. study. Without their support, I would not have been able to finish this work. I would dedicate this work to my parents.

TABLE OF CONTENTS

1 Introduction - 1 -
  1.1 Optical Coherence Tomography (OCT) - 1 -
    1.1.1 Configuration of OCT - 2 -
      1.1.1.1 Time Domain OCT - 2 -
      1.1.1.2 Fourier Domain OCT - 5 -
    1.1.2 Requirement for the Light Sources - 6 -
  1.2 Broad Gain Profile AMQW Devices - 7 -
  1.3 Organization of the thesis - 9 -
2 Broadly Tunable AMQW Lasers for Optical Coherence Tomography - 10 -
  2.1 Introduction - 10 -
  2.2 AMQW DOE SXC Laser - 10 -
    2.2.1 Diffractive Optical Element (DOE) - 10 -
    2.2.2 AMQW Broad Gain Semiconductor Laser - 12 -
  2.3 Theory for OCT resolution - 16 -
    2.3.1 Coherence Function of Broad-band SLDs - 17 -
    2.3.2 Coherence Function of a Multimode Diode Laser - 18 -
    2.3.3 Wavelength Tuning Fourier Domain OCT with a Tunable Diode Laser - 21 -
  2.4 Application to Fourier Domain OCT - 23 -
  2.5 Application to Synthesized OCT (SOCT) - 25 -
  2.6 Conclusion - 30 -
3 Waveguide Optimization for SLD - 31 -
  3.1 Introduction - 31 -
    3.1.1 Ridge Waveguide Structure - 32 -
    3.1.2 Refractive Index of InGaAsP Layers - 33 -
    3.1.3 Confinement Factor - 34 -
  3.2 Confinement Factor Calculation - 35 -
  3.3 Optimization of the Confinement Factor - 40 -
  3.4 Conclusion - 49 -
4 Active Region Design Considerations for AMQW Broad Spectral Width SLDs and Measurements of SLDs - 50 -
  4.1 Introduction - 50 -
  4.2 AMQW SLD active region design consideration - 51 -
  4.3 Model Descriptions - 53 -
  4.4 Experimental Results - 59 -
  4.5 Conclusion - 63 -
5 OCT Measurements and OCT Image Processing - 64 -
  5.1 Introduction - 64 -
  5.2 Comparison of OCT Measurements - 64 -
    5.2.1 Time Domain OCT Measurement of a Glass Cover Slip - 64 -
    5.2.2 Fourier Domain OCT Measurement of Glass Cover Slip - 67 -
    5.2.3 Synthesized OCT Measurement of Glass Cover Slip - 67 -

5.3 OCT Image Processing—Blind/non-blind Deconvolution - 68 -
  5.3.1 Describing OCT Setup as a Linear Shift Invariant (LSI) System - 68 -
  5.3.2 Noise Analysis of Our OCT System - 70 -
  5.3.3 Deconvolution with Jansson Van Cittert's Method - 71 -
  5.3.4 Blind Deconvolution with Richardson-Lucy Algorithm - 71 -
  5.3.5 Discussion - 77 -
5.4 Conclusion - 77 -
6 Conclusion - 78 -
6.1 Summary of the Thesis - 78 -
6.2 Suggestion for Future Work - 79 -
  6.2.1 1.3 μm Tunable Laser Diode - 79 -
  6.2.2 SLD Waveguide with Low Beam Divergence Far Field - 79 -
  6.2.3 FPGA for Blind Deconvolution on OCT Setup - 79 -

LIST OF FIGURES

Figure 1.1 Components of a time domain OCT system - 3 -
Figure 1.2 Simulated interferogram, used the layer parameters given in the table above. - 4 -
Figure 1.3 Schematic of Fourier domain OCT. - 5 -
Figure 1.4 Schematic of single QW laser diode - 7 -
Figure 2.1 Comparison of the DOE external cavity and the lens-grating external cavity in a Littrow configuration - 11 -
Figure 2.2 Front view of the DOE: a Fresnel zone plate with a surface topography proportional to cos(αr^2) - 11 -
Figure 2.3 Schematic of the FP mode for acquisition of the gain spectra. - 15 -
Figure 2.4 (a) RG product of the AMQW laser. (b) spectral range of operation of the AMQW DOE SXC laser. - 16 -
Figure 2.5 (a) Assumed time-averaged laser power spectrum (its envelope is corresponding to S (v) in Eq. (2.16)). (b) Simulation result of the autocorrelation function of 7 longitudinal modes - 20 -
Figure 2.6 Schematic of Fourier domain OCT - 24 -
Figure 2.7 (a) Schematic of reflection from a glass cover slip (b) Interferogram of the glass cover slip by tuning the AMQW laser from 1488 nm to 1605 nm over 119 modes (c) Recovered signal from an interferogram from a cover slip obtained with a laser with a mode spacing of 1 nm (d) Recovered signal from an interferogram obtained with a laser with a mode spacing of ~0.5 nm - 25 -
Figure 2.8 Schematic diagram of a DOE enabled tunable AMQW diode laser for synthesized OCT - 26 -
Figure 2.9 When the tuning range of the external cavity laser is larger, the coherence length will be shorter. (a) Interference fringe by scanning the reference mirror over a wide range for SOCT. (b) Record of the central peak over a path difference of -70 μm to 70 μm for averaging over a FWHM of 30 nm. (c) Record of the central peak of the interference fringe to show the depth resolution is around 34 μm for averaging over a FWHM of 30 nm. (d) Depth resolution is around 20 μm for averaging over a FWHM of 56 nm. (e) Depth resolution is around 15 μm for averaging over a FWHM of 72 nm. - 29 -
Figure 2.10 Measurement result of a glass cover slip for synthesized OCT with averaging over FWHM of 80nm - 29 -
Figure 3.1 Ridge waveguide InGaAsP/InP SLD - 32 -
Figure 3.2 Schematics of solving 2-D ridge waveguide with arbitrary layers in the growth direction - 35 -
Figure 3.3 General form of a multilayer structure. Each layer (j) is of uniform index n_j. A_j and B_j are forward and backward propagation wave amplitudes. W_j is the layer thickness - 36 -
Figure 3.4 Plot of α_4 vs. index - 37 -
Figure 3.5 Electric field in the y direction (a) ridge area. (b) shoulder area - 38 -
Figure 3.6 Electrical field in x direction - 39 -
Figure 3.7 Improvement of confinement factor starting from #4177 - 41 -

Figure 3.8 Improvement of confinement factor starting from table 3.4 - 45 -
Figure 3.9 PL peak of wafer M 0446 - 46 -
Figure 3.10 Schematic of double-Section Angled-Stripe Structure - 47 -
Figure 3.11 spectrum of double section SLD cleaved from M0446 with power of 1.04mW; FWHM: 75nm. (b)spectrum of double section SLD cleaved from wafer #4177 with power of 0.533mW;FWHM: 75nm. - 48 -
Figure 4.1 Depiction of the transition carrier density concept - 52 -
Figure 4.2 AMQW active regions of Structure 1 (a) and Structure 2 (b) - 55 -
Figure 4.3 Calculated gain spectra for Structure 1 (wafer# 3979) at three carrier densities - 56 -
Figure 4.4 Calculated gain spectra for Structure 2 (wafer# M0446) at three carrier densities - 56 -
Figure 4.5 Simulated carrier density verse injected current in QW at the p-side for Structure 2 - 57 -
Figure 4.6 Model spectra for Structure 1 with cavity length of 450 μm - 58 -
Figure 4.7 Model spectra for Structure 2 with cavity length of 250 μm - 58 -
Figure 4.8 Measured Spectra for Structure 1 with 450 μm cavity length - 59 -
Figure 4.9 Measured output spectra for Structure 2 with 400μm cavity length - 60 -
Figure 4.10 LI curve of Structure 2 F700/B400 μm SLD pumping front section - 61 -
Figure 4.11 Effect of double section SLD (F750μm /B400μm) of Structure 2 - 62 -
Figure 4.12 Ripple of F750μm /B400μm of Structure 2 by pumping the front section only - 62 -
Figure 5.1 Schematic of the time domain OCT - 65 -
Figure 5.2 (a) One longitudinal scanning of a glass cover slip. (b) Envelope of (a). (c) Autocorrelation function of the 1.3 μm SLD - 66 -
Figure 5.3 Fourier domain OCT measurement of single point on a cover glass slip - 67 -
Figure 5.4 (a) One longitudinal scanning with synthesized OCT of a cover glass slip (b) Envelope of (a). (c) Autocorrelation function of SOCT with the 1.55 μm tunable laser working as a incoherent source. - 68 -
Figure 5.5 Point spread functions for (a) time domain OCT, (b) Fourier domain OCT, and (c) synthesized OCT - 70 -
Figure 5.6 Demonstration of Jansson's deconvolution method and Richardson-Lucy algorithm. (a) Simulated PSF (b) Simulated blurred image with the third peak merged with a small peak. (c) Deconvolved with Jansson's method. (d) Deconvolved with Richardson-Lucy algorithm. - 73 -
Figure 5.7 Deconvolution with Gaussian white noise on the synthesized image. (a) Synthesized image with Gaussian white noise of standard deviation 0.005. (b) Deconvolved with Jansson's method. (c) Deconvolved with the Richardson-Lucy algorithm. - 74 -
Figure 5.8 Blind deconvolved PSF for (a) time domain OCT. (b) Fourier domain OCT. and (c) Synthesized OCT. - 75 -
Figure 5.9 Effect of image enhancement with Richardson-Lucy algorithm - 76 -

LIST OF TABLES

Table 1.1 Development of Medical Imaging - 1 -
Table 2.1 Structure of compositionally AMQW laser (wafer # 4381) - 14 -
Table 3.1 Structure of an SLD centered at 1300 nm (wafer # M0446) - 33 -
Table 3.2 Structure of wafer #4177 - 42 -
Table 3.3 Structure for nonlinear fitting result which started with #4177 - 43 -
Table 3.4 Varied structure with two SCH layers as a starting point for the nonlinear fitting - 44 -
Table 3.5 Optimized structure with two SCH layers - 45 -

1 Introduction

1.1 Optical Coherence Tomography (OCT)

Optical coherence tomography (OCT) is an emerging biomedical, non-invasive three-dimensional imaging technique, capable of producing high-resolution cross-sectional images for the internal microstructure of living tissue. An OCT imaging system mainly consists of a light source, a free-space or fibre-optic based interferometer, a detector, and low noise detection techniques. In OCT imaging, interference fringes, which encode cross-sectional or depth information of the sample, are only observed when the optical path lengths of the reference and sample arms are matched to within the coherence length of the light source.

Minimally invasive imaging techniques such as X-ray (1885), ultrasound (1965), computed tomography (CT, 1973), magnetic resonance imaging (MRI, 1983), and radioisotope imaging (position emission tomography, PET, 1999) have revolutionized diagnostic medicine during the past decades, e.g., see Table 1.1.

Table 1.1 Development of Medical Imaging

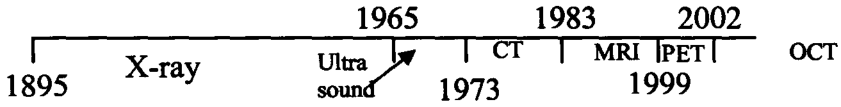

The existing minimally invasive techniques permit three-dimensional visualization; however, their spatial resolution is typically limited to a few millimeters in standard clinical practice. OCT should achieve resolutions of 2 to 15 μm to a depth of 2 mm with the use of low-coherence light sources. The depth resolution of OCT is inversely proportional to the full-width-half-maximum (FWHM) (spectral width) of the light source.

D. Huang *et al*[1] first applied OCT to diagnostic medicine, but the roots of OCT lie in early work on white-light interferometry that led to the development of optical coherence-domain reflectometry (OCDR).[2] Since the original work, a large number of papers have been published regarding all aspects of OCT. The group of Dr. G. Fujimoto at MIT,[3] the group of Dr. A. F. Fercher at the University of Vienna, Austria[4] and the group of Dr. J. M. Schmitt[5] are a few of the top leaders in research on OCT. The research covers general physics, optics, material sciences, and a wide variety of specific medical areas such as ophthalmology, neurology, and endoscopy. Review papers have been published on various aspects of OCT.[6,7]

Ophthalmology was the first field of application of OCT. The lens and fluid of the eye are essentially transparent over broad spectral ranges, transmitting light with only minimal optical attenuation and this provides easy optical access to the retina, which makes the *in vivo* imaging of a biological sample possible. The potential of OCT to perform noninvasive, high-resolution biometry of intraocular distance has been utilized in studies of the cornea,[8] intra-ocular lenses,[9] and recovery after cataract surgery as well as in research of the development of myopia.[10] A prototype ophthalmic OCT system has developed into a clinical instrument by Carl Zeiss Meditec Inc. of California, US.

OCT has now advanced to a powerful imaging technology for a large range of clinical diagnostic applications in other medical fields that have highly scattering tissue, such as imaging of subsurface structures in the upper gastrointestinal (GI) tract,[11] and intravascular imaging.[12] Most recently, a couple of articles in Laser Focus World revealed the progress of research in OCT applications, including OCT imaging of the developing heart *in vivo,*[13] dental diagnostics with time domain OCT,[14] 3-D imaging of living cells by MIT researchers[15] and classical dispersion-cancellation of OCT by the group of Dr. Bizheva.[16]

Functional OCTs were developed as extensions of OCT technology. Real-time Doppler OCT was investigated[17] to measure a wide range of low velocities such as detecting *in vivo* blood flow. Polarization OCT[18] was developed to provide spatially resolved imaging of materials that have strong birefringence.

1.1.1 Configuration of OCT

Based on how the depth information is acquired, OCT is divided into two categories – *time domain OCT* and *frequency domain OCT* (or Fourier domain OCT). I also worked on *synthesized OCT* in my Ph.D. research, but in the way of acquiring signals, synthesized OCT belongs to the category of time domain OCT. The difference between synthesized OCT and standard time domain OCT is in the operation of the light source: time domain OCT uses broad spectral width light sources such as super-luminescent diodes (SLDs) or ultra-short laser pulses; synthesized OCT uses broadly tunable lasers.

1.1.1.1 Time Domain OCT

Figure 1.1 shows a schematic diagram of a typical time domain OCT. The heart of the system is a Michelson interferometer illuminated by a broad spectral width light source, which is either an SLD or an ultra-short pulsed laser. The interferometer splits the light from a broad spectral width source into a reference arm and a sample arm. The light from the sample arm is focused through the scanning optics and objective lens to some point below the surface of the sample. The light scattered back from the sample, marked as E'_s, will interfere with the light field that is reflected from the reference mirror E_r in the Michelson interferometer. The Michelson interferometer is built with a beam splitter for free space OCT or with a 50/50 fiber coupler for fiber based OCT. The output of the interferometer is detected by the photo-detector. The position of the scattering center is measured by the scanning position of the reference mirror because the fringes are formed only when the path difference of the two arms is within the coherence length of the source. The scanning of the reference mirror is called the longitudinal scan. The amplitude of the interference fringe is a measure of the strength of the scattering center.

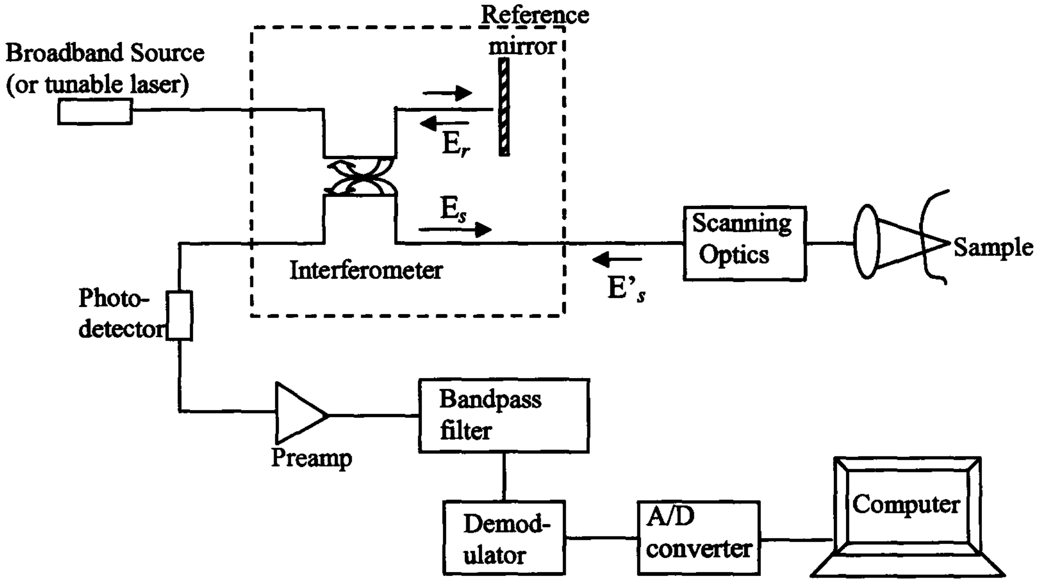

Figure 1.1 Components of a time domain OCT system

The strengths of the scattering centers are usually weak. A high sensitivity is achieved by using optical heterodyne detection techniques. The light in the arms of the interferometer are frequency shifted by a Doppler effect, which is caused by scanning of the reference mirror and by an applied modulation of the length of the reference arm. The output of the photo-detector is filtered in the demodulator to separate the desired interferometric signal from noise outside the signal bandwidth.

To acquire data for a two-dimensional image, the optical beam in the sample arm is laterally translated between longitudinal scans. The lateral resolution is limited by the beam diameter inside the sample. The data is then digitized and built into 3-D image by the computer.

A simulated interferogram (i.e., the output of the interferometer as a function of position of the reference mirror) for a single longitudinal scan of a three layer reflector is shown in Figure 1.2. The table above the figure shows that there are three reflection surfaces: between layers 1 and 2, between 2 and 3, and between 3 and 4. The displacement of the reference mirror reflects the depth of the reflector from the sample surface. The power spectral density (PSD) of the light source was assumed to have a Gaussian shape with a full width half maximum (FWHM) of 200 nm and a center wavelength of 1300 nm.

Layer *j*	Refractive index *n*	Layer thickness (μm)
1	1.00	15 μm
2	1.30	20 μm
3	1.50	95 μm
4	1.00	20 μm

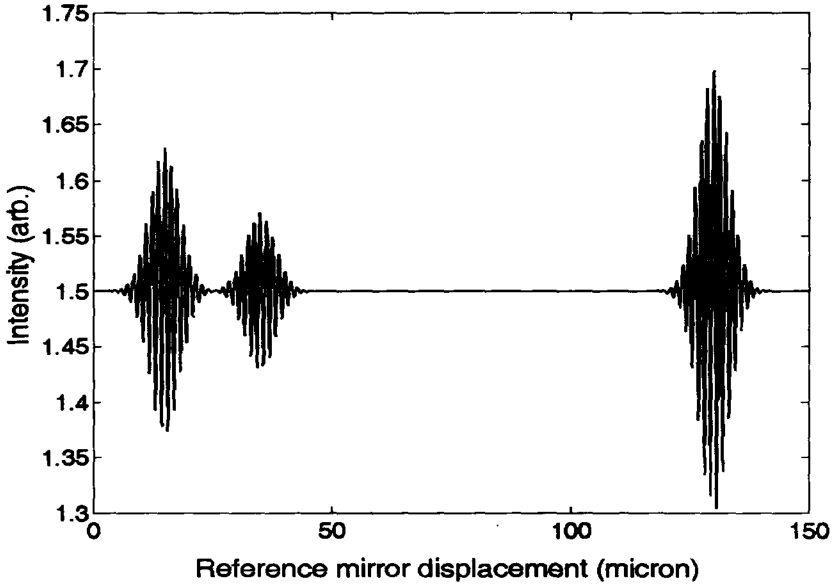

Figure 1.2 Simulated interferogram, used the layer parameters given in the table above.

The depth resolution of time domain OCT is determined by the width, usually measured as the FWHM, of the autocorrelation of the electric field from the source, which is also the coherence length of the light source.[19] This is an important and also a basic parameter of a time domain OCT system. The width of the coherence function of broad spectral width SLDs and thus the depth resolution δz of a time domain OCT is inversely proportional to the spectral width $\Delta\lambda$ of the source:

$$\delta z = \frac{c}{n_g}\frac{\delta\tau}{2} = \frac{2\ln 2}{\pi n_g}\frac{\lambda_o^{\ 2}}{\Delta\lambda} \tag{1.1}$$

where c is the speed of light in free space, $\delta\tau$ is the relative time delay of light between the two arms of the interferometer, n_g is the group index of the sample, and λ_0 is the centre wavelength of the source. Therefore, the broader the spectral width of the source, the higher is the depth resolution of OCT.

1.1.1.2 Fourier Domain OCT

Compared with time domain OCT, Fourier domain OCT (FD OCT) does not need to scan the reference mirror to acquire the depth information of the sample. It has been demonstrated that the signal-to-noise ratio (SNR) for a Fourier domain OCT system could be greater than the SNR for a time domain OCT system.[20]

There are two types of Fourier domain OCT – spectral interferometry FD OCT and wavelength tuning FD OCT, as shown in Fig. 1.3. They both acquire the depth reflectivity information by Fourier transformation of the interferogram. The differences between the two methods are associated with the choice of the light source or the detector. Spectral interferometry OCT utilizes a broad spectral width light source such as an SLD, a diffraction grating, and a CCD for the detection. The advantage of this method is that the light source is easy to obtain, but the drawback is that CCD arrays for certain wavelength ranges are not available and, if CCD arrays are available, they are more expensive than point detectors such as photodiodes. In addition, a CCD may cause a problem associated with phase washout by changes in the sample arm length during the pixel integration time.[4]

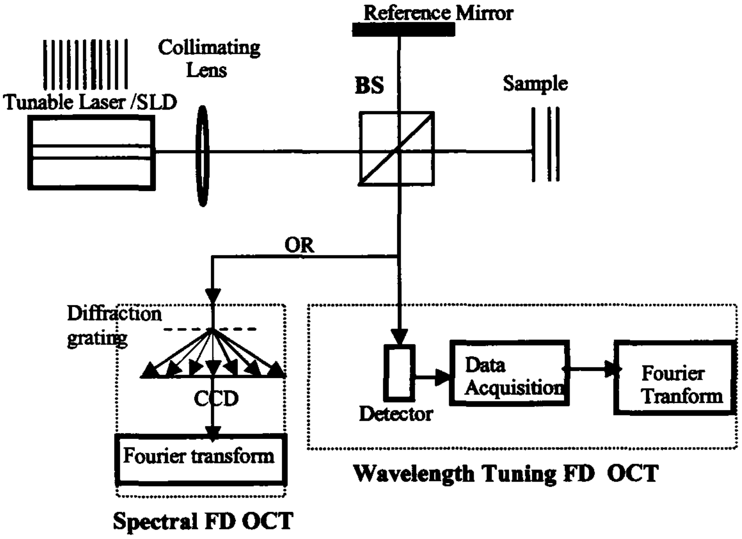

Figure 1.3 Schematic of Fourier domain OCT.

Therefore, wavelength tuning FD OCT has been more widely used than the spectral interferometric technique. In this method, a broadly tunable laser is applied as a light source and a conventional photodetector is used for detection of the interference fringes. Fourier transformation is performed after the data acquisition. In this set-up, instead of scanning the reference mirror, the light source is tuned and the depth scattering information is encoded in the spectral interferogram. The depth resolution of Fourier domain OCT is proportional to the FWHM of the tuning range of the source. The derivation of the relation of depth resolution to the tuning range for wavelength tuning FD OCT is given in Chapter 2.

1.1.2 Requirement for the Light Sources

To obtain high depth resolution for an OCT system, the broad spectral width source is by far the most important. Two types of light sources are normally adopted for time-domain OCT systems: superluminescent diodes (SLD) or solid-state femto-second lasers such as a Ti: sapphire laser. Compared with short-pulse lasers, SLDs have the advantage of emitting light with extremely low amplitude noise, thus the use of an SLD as the light source can increase the signal-to-noise ratio. The other requirement for the light source is the shape of the spectrum. The ideal light source for OCT would have a Gaussian spectral shape to avoid the presence of the secondary peaks on the coherence function. An SLD would also fit for this requirement. Therefore, an SLD with broad spectral width is often a better choice than ultra-short solid state laser pulses.

For Fourier domain OCT, a broadly tunable laser is required. Similar to time-domain OCT, the resolution for Fourier domain OCT is determined by the tunable range of the light source. It will be shown in this thesis that the short-external-cavity (SXC) broadly tunable diode laser could cover over 100 nm of tunable wavelength range. This device is thus a good fit for the light source requirements for Fourier domain OCT.

The choice of the center wavelength of an OCT system depends on the absorption of the sample, the penetration depth, and particularly in biomedical applications, the maximum permissible light exposure at this wavelength. Centre wavelengths of 800 nm, 1060 nm and 1300 nm have been applied in ophthalmic OCT until recently. Basically a shorter centre wavelength will achieve higher resolution compared with a source with a longer centre wavelength for the same spectral width (see Eq. 1.1). The absorption profile of water has a minimum at 800 nm. Because ophthalmic OCT takes images of the retina, the water absorption in the eye is of concern for the intensity loss of the signal. However, ophthalmic OCT with a light source with a centre wavelength of 800 nm has a low penetration depth in the retina and the permissible exposure for the eye is low at 800 nm.[21] The absorption of water shows a local minimum at 1060 nm and a second local minimum at 1300 nm. At these two wavelengths, the retinal penetration depth will be higher and is suitable for ophthalmic OCT. The high permissible exposure at these wavelengths will compensate the loss caused by the water absorption. Thus 1300 nm and 1060 nm are widely used for ophthalmic OCT. The researches in this thesis will focus on the realization of a 1300 nm SLD for use in OCT. For Fourier domain OCT and synthesized OCT, a broadly tunable diode laser centered at 1.55 μm was used for demonstrating the results in this thesis.

Devices with asymmetric multiple-quantum wells (AMQWs) exhibit broad gain spectra. It has been shown in our research group that AMQW short external cavity lasers are broadly tunable laser sources. In this thesis, I will show that AMQWs also make broad spectral width SLDs. Therefore, AMQW SLDs and lasers could be used as light sources for time domain OCT, Fourier domain OCT, and synthesized OCT, respectively.

1.2 Broad Gain Profile AMQW Devices

Semiconductor lasers operate by the process of carrier recombination in the active region of the device. Quantum well (QW) laser diodes are p-i-n junctions containing thin layers of varying bandgap material, which form a quantum well of low bandgap, sandwiched between layers of higher bandgap in the intrinsic region. Under forward bias, electrons will be injected from the n-side while the holes are injected from the p-side, with carrier recombination occurring inside the quantum well layer in the active region, producing light.

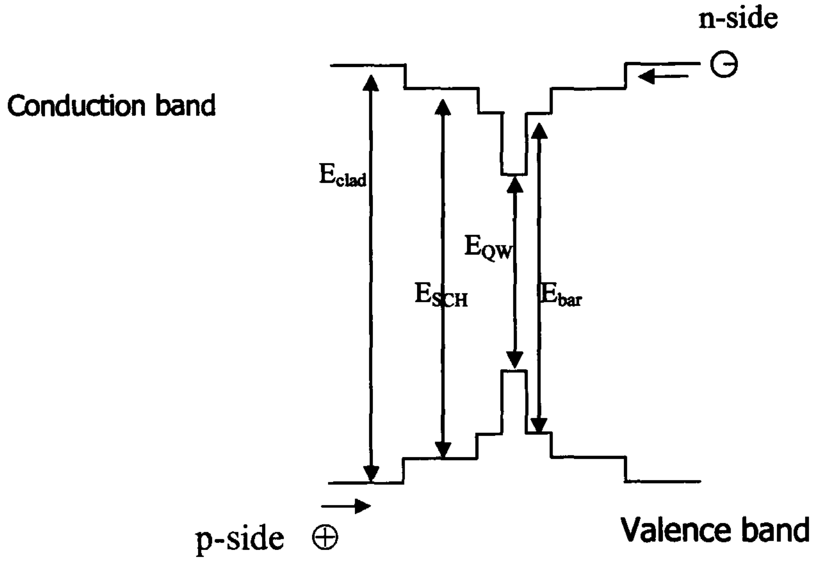

Figure 1.4 Schematic of single QW laser diode

A typical energy diagram of an InGaAsP/InP single QW diode laser is shown in Fig. 1.4. The separate confinement heterostructure (SCH) layers are used to establish an optical waveguide in the growth direction of the laser structure and to help establish single spatial mode operation of the laser.

The energy bandgaps of the various layers are set by the composition of the $In_{1-x}Ga_xAs_yP_{1-y}$ material. The $In_{1-x}Ga_xAs_yP_{1-y}$ system can be designed to have a bandgap, as measured by the wavelength of emission, in the range of 1.0 – 1.7 µm by varying the x and y material parameters while maintaining lattice-matching to the InP substrate.

Soon after the development of the QW laser, it was found that by proper design of the heterostructure layers in the active region, it was possible to inject carriers into multiple QWs (MQW) and thereby enhance the amount of gain material experienced by the optical field. The strength of the MQW laser is that each QW can have a different wavelength of operation, and the output gain spectrum of the laser will be a sum of the gain contributions from all of the wells in the active region. Lasers that employ MQWs with more than one operating wavelength are called asymmetric multiple quantum well (AMQW) lasers. AMQW lasers have quantum wells (QWs) of varying thickness and/or composition in a single active region. We define AMQW devices with QWs of varying thickness as *dimensionally asymmetric* MQW devices and those with QWs of varying composition as *compositionally asymmetric* MQW devices. Because each QW has a different wavelength of operation, the gain profile of the AMQW active region will be broad and flat under certain injected carrier densities.

The broad gain profile of the AMQW laser is essential for realizing a broadly tunable diode laser. The research on this characterization was first done by Dr. Michael J. Hamp in our group.[22] It was reported that the AMQW lasers only exhibit broad wavelength tuning ranges near a specific cavity length, which is called the transition cavity length (TCL). The TCL was defined as the cavity length below which a cleaved AMQW laser operates at short-wavelengths at threshold and above which the laser operates at long-wavelengths at threshold. For lasers that have cavity lengths that are shorter or longer than the TCL, the tunability of the laser is the same as that of a traditional (i.e., the QWs are all the same) quantum-well laser. Research on the difference of the TCL of mirror image AMQW laser structures showed that the carrier distribution in the QWs from the p-side to the n-side is not uniform. Thus the sequence of QWs does matter for AMQW device design.

Dr. S. C. Woodworth[23] showed experimentally an InGaAsP AMQW laser which could be tuned in a short external cavity over a 172-nm range. This laser was designed on the idea of a TCL. Theoretical modeling of the AMQW laser gain spectrum was performed by Dr G. B. Morrison, Dr. S. C. Woodworth, and Dr. H. Wang in our group.[24] They started with the band structure calculation using a Galerkin method, and then calculated the transition matrix element and finally the total gain by summing up the gain profile for each QW. Dr. S. C. Woodworth finally integrated the calculation into an application named *k·p sim* with a user-friendly interface which we could use to design AMQW devices easily by calculating the gain spectrum.

Traditional short external cavity tunable laser diodes include a collimated lens and a diffraction grating. Cassidy *et al* [25] designed a diffractive optical element (DOE) which combined the function of the lens and grating to realize the short external cavity. It will be shown in Chapter 2 in this thesis that the broad-gain AMQW laser combined with the DOE is a suitable light source for Fourier domain OCT and for synthesized OCT.

The broad gain of an AMQW active region also makes AMQW active regions ideal candidates for SLDs. Early work to produce broad spectral width SLDs mainly focused on the design of the active region[26] with symmetric multiple quantum wells.[27] Lin *et al*[28] used asymmetric multi-quantum wells (AMQW) for SLDs but they only reported experimental results. Until now, there has been no theoretical direction for the design of the AMQW active region for a broad spectral width SLD. Based on the theoretical modeling of the AMQW gain spectrum, research targeting the design of the active region of AMQW SLDs was investigated in this thesis. This thesis includes waveguide optimization of AMQW SLDs to obtain both broad spectral outputs and reasonable emitting powers.

1.3 Organization of the thesis

My thesis is organized as follows: after the introduction of Chapter 1, the application of broadly tunable AMQW lasers for both Fourier domain OCT and synthesized OCT is presented in Chapter 2. Based on the experience of our research group, it has been found that it is important to optimize the confinement factor of the laser waveguide. This enhances the interaction efficiency of the light that is confined in the active region with the carrier inversion. A transfer matrix method was applied to solve for the modes in the waveguide and then least-square nonlinear fitting was used to optimize the confinement factor. These results are presented in Chapter 3. In Chapter 4, the active region design considerations for an AMQW SLD are introduced.

Based on the light sources that were developed in this project, I demonstrate in Chapter 5 the operation of a Michelson interferometer based OCT system with broadly tunable AMQW laser diodes and with AMQW SLDs. In addition, a comparison of the resolution obtained with the different sources and categories of OCT is presented in Chapter 5. An image processing technique of blind deconvolution was studied to enhance the images obtained from Fourier domain, time domain, and synthesized OCT. Chapter 6 consists of conclusions and a discussion of future work.

2 Broadly Tunable AMQW Lasers for Optical Coherence Tomography

2.1 Introduction

I report in this chapter the application of a broadly tunable asymmetric multiple-quantum-well (AMQW) laser in an external cavity for both time-domain and Fourier-domain optical coherence tomography (OCT). The AMQW laser was custom designed and fabricated to have a large tuning range when operated with no facet coatings in a diffractive optical element (DOE) short external cavity (SXC). Single-mode operation and broad wavelength tunability from AMQW lasers have been demonstrated.[22] With a tunable AMQW laser diode as a light source, Fourier domain OCT and synthesized OCT were investigated by measuring the reflectivity of a glass cover slip. The depth resolution of Fourier domain OCT was found to be as short as 13 μm in air with the 117 nm tuning range (FWHM of 80 nm) of the AMQW DOE SXC source.

For synthesized OCT, which is an implementation of time-domain OCT, I simulated the coherence function of the source and detection scheme. Experimentally, the synthesis of the coherence function is performed by increasing the averaging time of the detector. I demonstrated synthesized OCT with the DOE SXC AMQW sources and found that the depth resolution is set, as expected, by the tuning range of the AMQW DOE SXC laser.

2.2 AMQW DOE SXC Laser

2.2.1 Diffractive Optical Element (DOE)

An external cavity configuration that employs a DOE to tune the wavelength of an uncoated Fabry-Pérot diode laser was first reported by Dr. Cassidy and Michael Hamp (1999).[25] As shown in Fig.2.1, the DOE was designed to replace the combination of a collimating lens and a diffraction grating in a Littrow configuration. The DOE SXC provides the dual function of a focusing element for high coupling efficiency into the active region and of wavelength selectivity for single longitudinal mode operation. The DOE has several advantages over the lens-grating external cavity, such as one external cavity, ease of alignment, and a linear tuning motion of the DOE. These features are ideal for the light source requirement of Fourier domain OCT and synthesized OCT, as will be shown in this chapter.

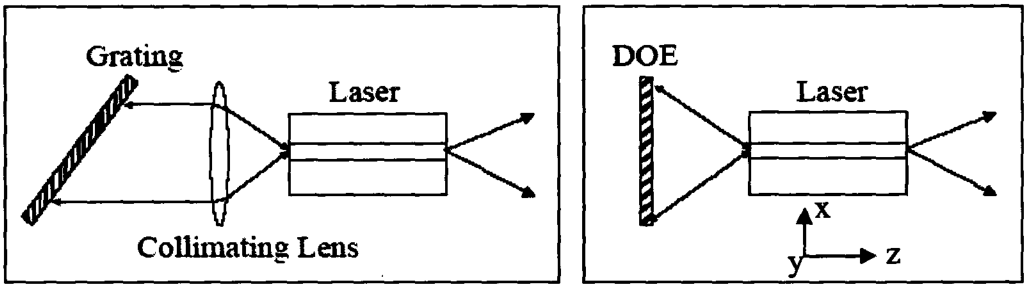

Figure 2.1 Comparison of the DOE external cavity and the lens-grating external cavity in a Littrow configuration[29]

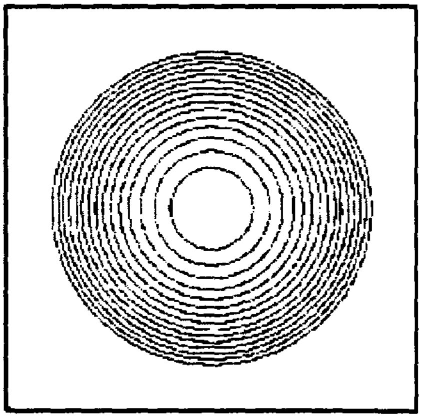

Figure 2.2 Front view of the DOE: a Fresnel zone plate with a surface topography proportional to cos(αr^2)

The principle of operation of the DOE can be understood from an analysis of a simple transmissive Fresnel zone plate[30] as shown in Fig. 2.2. The positive focal length of a Fresnel zone plate with transmissivity of

$$t(x,y)=\frac{1}{2}\{1+\cos[\alpha(x^2+y^2)]\} \tag{2.1}$$

is

$$f=\frac{\pi}{\lambda\alpha} \tag{2.2}$$

where α is a constant that is set by the physical characteristics of the zone plate. For the DOE that is used in my work, the designed focal length is 0.25 cm at $\lambda = 1.4$ μm and $\alpha = 8.98\times10^8\,\mathrm{m}^{-2}$.

The zone plate can be thought of as a diffraction grating with a grating period such that constructive interference occurs for a certain wavelength at one point along the optic axis (*z* axis in Fig. 2.1) of the optical system. Thus the zone plate acts as a lens with strong chromatic aberration; wavelengths are focused to unique distances along the optic axis. Higher diffraction efficiency can be obtained by sculpting the surface of the optical element to create a phase grating rather than an amplitude transmission grating. The DOE used in this work is a reflective phase zone plate. The surface topography was etched to eight discrete levels.

The working distance of the DOE is twice the focal length. Thus for the DOE that I used, the DOE was positioned z_{DOE} ~0.5 cm behind the back facet of the AMQW laser and was aligned to be parallel to the laser facet. The distance Δz_{DOE} that the DOE must be moved back and forth to change the wavelength that is focused on to the laser facet is given by:

$$\frac{\Delta z_{DOE}}{\Delta\lambda} \approx -\frac{z_{DOE}}{\lambda} \tag{2.3}$$

According to this equation, to tune $\Delta\lambda = 1$ nm at $\lambda = 1550$ nm, a translation of $\Delta z_{DOE} \approx 3.22$ μm is required. A DOE SXC AMQW laser centered at 1550 nm operated single mode, with a side mode suppression ratio (SMSR) of 30 dB, from 1488 nm to 1605 nm. Thus a linear translation of the DOE of $\Delta z_{DOE} \approx 376$ μm was required to tune over the full range. The 117 nm tuning range corresponds to an 80 nm FWHM envelope of an approximately Gaussian shaped power spectral density (PSD).

2.2.2 AMQW Broad Gain Semiconductor Laser

The AMQW laser that I used was a compositional asymmetric quantum well (AMQW) laser with wells of 50 Å and with barriers of 100 Å. The laser was compositionally asymmetric in that the quantum well materials of the active region differ so that the active region is not symmetric. A dimensionally AMQW laser would have wells of different thicknesses but the same composition.[23]

There are advantages to using a compositionally AMQW as opposed to a dimensionally AMQW structure. The optical gain is a function of the magnitude of the overlap of the quantum well with the optical mode. Dimensionally asymmetric AMQW devices thus have optical gains that vary, owing to the optical confinement factor, with the wavelength of emission of the well. Since the quantum wells in a dimensionally AMQW device that are designed to emit at short wavelengths will be thin, these short wavelength wells will exhibit lower modal gain than the long wavelength wells. Additional short wavelength wells can be added to compensate for the loss of modal gain owing to the confinement factor decrease, but this makes strain balancing more difficult. In addition, any carrier processes that are a function of the thickness of the well, such as carrier capture, will also need to be compensated. Compositionally AMQW structures have wells of the same thickness and thus do not require these compensations.

The compositions of the wells are chosen to give a broad and flat gain peak. An eight-band $\boldsymbol{k}\cdot\boldsymbol{p}$ Galerkin-based simulator was used in the design of the active region.[31,24] The Galerkin method takes into account coupling of the electron wave functions between wells and uses simple analytic solutions for the wave functions for each well as basis functions. The wave functions for the entire structure are found as sums over the basis functions. The analytic nature of the basis functions means that overlap integrals that are required to compute the optical gain can be performed analytically as opposed to numerically. This feature is an advantage in computation of the gain.

The models for the gain of a semiconductor laser are accurate in the region of the gain peak. However, the net modal gain at short wavelengths depends on the gain of the short wavelength wells and on gain from the long wavelength wells. For a broadly tunable laser, the difference in wavelengths between the long wavelength wells and the short wavelengths wells is large enough that the models do not accurately predict the contribution of the long wavelength well to the modal gain at short wavelengths. An AMQW will lase up to 50 nm on the long wavelength side of the gain peak of the short wavelength wells. This is because of the absorption by the long wavelength wells.[32] This absorption is underestimated by the gain models and must be taken into account in the design of the active region.

A second physical mechanism, which is not accurately described in the model, is the non-uniform injection of carriers into the wells of the active region.[33,34] For InP based materials, the conduction band offset is such that the holes see a greater impediment to movement than do the electrons. As a result, the holes tend to stay near the p-side and the wells near the p-side may have greater gain than the wells near the n-side of the active region. For GaAs based material, the conduction band offset is such that the electrons see a greater impediment to movement and the wells near the n-side should show greater gain than the wells near the p-side. The eight-band ***k·p*** Galerkin-based simulator, which we use to design AMQW structures, uses a phenomenological approach to account for the non-uniform injection. Thus experience and intuition must be used to supplement the design.

The compositionally AMQW design that I used to make the OCT measurements reported here has five quantum wells with PL peaks at 1.599 μm, 1.458 μm, 1.430 μm, 1.430 μm, and 1.599 μm from the p-side to the n-side at 300 K. Table 2.1 shows the structure of the AMQW laser. Fabry-Pérot AMQW lasers were cleaved based on the theory of a transition cavity length (TCL).[22] When laser cavity lengths are near the TCL, a broad-flat gain curve is observed. It was found that it is necessary to cleave the laser a bit longer than the TCL. In this case, the AMQW laser will operate at threshold on long wavelength transitions. By increasing the injection current, the short wavelength transitions will appear and the two wavelengths will lase simultaneously. At even higher currents, the long wavelength peak will disappear and only the short wavelengths keep lasing. Lasers from wafer # 4381 were characterized and the TCL was measured to be around 700 to 800 μm. An 800 μm cavity length is an optimum length for single longitudinal mode tunability. A measure of the non-uniform injection is obtained from the difference in the TCLs for mirror image structures.[22] Mirror image structures have the sequence of wells reversed in going from the n-side to the p-side and *vice versa*.

Table 2.1 Structure of compositionally AMQW laser (wafer # 4381)

Layer type	Thickness (Å)	$In_{1-x}Ga_xAs_yP_{1-y}$ composition		PL peak at 300.0K (nm)
		x	y	
SCH	1500.0	0.0	0.0	
SCH	700.0	0.109	0.238	
Barrier	235.0	0.225	0.305	
Well	100.0	0.225	0.800	1599.1
Barrier	50.0	0.225	0.305	
Well	100.0	0.225	0.710	1458.5
Barrier	50.0	0.225	0.305	
Well	100.0	0.225	0.690	1430.4
Barrier	50.0	0.225	0.305	
Well	100.0	0.225	0.690	1430.4
Barrier	50.0	0.225	0.305	
Well	100.0	0.225	0.800	1599.1
Barrier	235.0	0.225	0.305	
SCH	700.0	0.0	0.0	
SCH	1500.0	0.0	0.0	

The reflectance gain (RG) product of the AMQW laser[35]could be obtained by measuring the depth of modulation introduced into the spontaneous emission spectrum by the Fabry-Pérot resonances. A max/min method was first introduced by Hakki and Paoli.[36] A modified method named mode sum/min was introduced by Dr. Cassidy to improve the accuracy of the gain measurement. The mode sum/min technique reduces the effect of the response function of the spectrometer used in the measurement on the estimated RG product. According to mode sum/min method, the mth mode single pass gain G_m ($G_m = \exp(g_m L)$, where g_m is the model gain and L is the laser cavity length) is:

$$G_m = \frac{1}{\sqrt{R_f R_b}}\left(\frac{p-1}{p+1}\right) \qquad (2.4)$$

where $p = \frac{c}{2l}p'$, and p' is the ratio of the m^{th} mode sum to the m^{th} minimum, which are obtained by the FP modulation introduced into the spontaneous emission spectrum. Figure 2.3 is a plot of FP modes and shows the quantities required in the mode sum/min method.

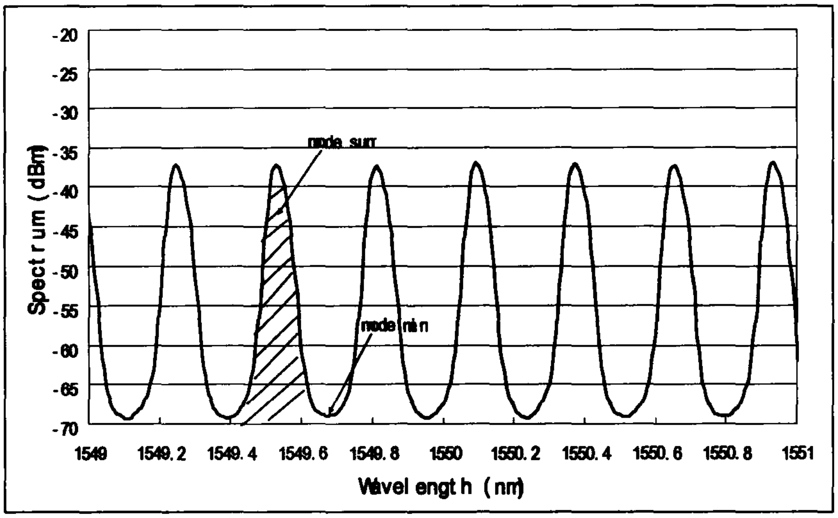

Figure 2.3 Schematic of the FP mode for acquisition of the gain spectra.

The RG product for an AMQW laser calculated using the mode sum/min method is shown in Fig. 2.4 (a) based on the F-P modulation spectra taken below threshold. The tunability of the AMQW laser in a DOE short external cavity is shown in Fig. 2.4 (b). The figure shows the spectra for some positions of the DOE behind the back facet. A broad tunability was achieved for a single laser injection current of 160 mA. The DOE SXC AMQW laser could be operated on all of the longitudinal modes from 1488 nm to 1605 nm. The longitudinal mode spacing is given by the well known equation: $\Delta\lambda = \lambda^2 / 2L_{cav} n_g$, where n_g is the effective group index of the laser waveguide and L_{cav} is the cavity length. If we take $n_g = 3.52$, $L_{cav} = 800$ μm, the mode spacing is 0.426 nm. Because of the flat gain over a broad range of wavelengths, broad tunability could be achieved without AR coating of the laser facet that faces the DOE. Figure 2.4 (b) demonstrates the relative power and the tuning range that can be obtained with the DOE SXC AMQW laser. At this current, single mode laser outputs of 17 mW could be obtained.

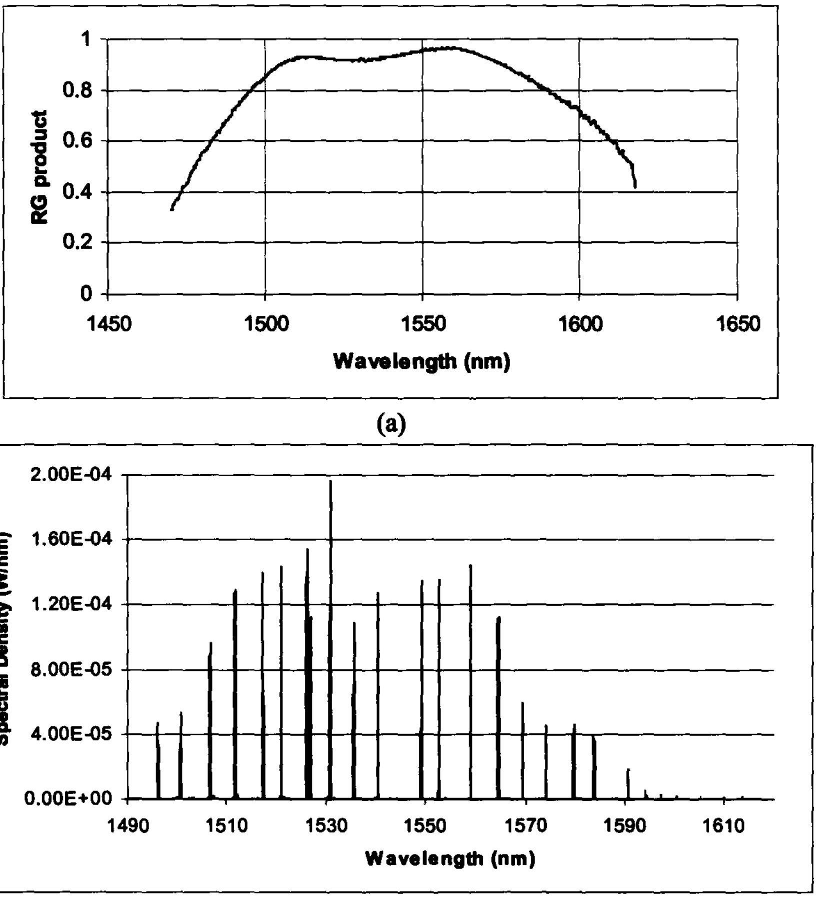

(a)

(b)

Figure 2.4 (a) RG product of the AMQW laser. (b) spectral range of operation of the AMQW DOE SXC laser.

2.3 Theory for OCT resolution

The depth resolution, i.e., the minimum resolvable distance between two reflectors, of an OCT system is proportional to the coherence length of the optical source. The coherence functions for the SLD and diode laser sources that are typically used for time-domain, Fourier domain, and synthesized OCT are significantly different. The coherence functions and hence depth resolutions for SLDs and multimode diode lasers are given in the next two sections. A relationship involving the desired depth resolution and the design of an AMQW source for wavelength tuning Fourier domain OCT is also given. The coherence functions for the sources are developed from an analysis of the output of a Michelson interferometer,[37] which is a description of a simple OCT measurement system.

2.3.1 Coherence Function of Broad-band SLDs

The electric field at the detector for two beam interference is

$$E(t, r_R, r_O) = a_R E_1(t - nr_R / c) + a_O E_1(t - nr_O / c) \tag{2.5}$$

where $t_R = t - nr_R/c$ and $t_O = t - nr_O/c$ are the retarded times which take into account the propagation delay over the different path lengths r_R and r_O in the two arms of the interferometer; n is the refractive index; c is the speed of light in vacuum; $\Delta r = r_R - r_O$ is the path length difference between the two beams; a_R is the reflection coefficient for the reference beam; and, a_O is the reflection coefficient for an object in the object arm. The detector, owing to the finite bandwidth of the electronics, performs a time averaging operation, which is denoted by $\langle\cdot\rangle$. The signal from the detector is a function of the relative time delay $\tau = t_R - t_O = 2n\Delta r/c$ between the two arms of the interferometer and is proportional to

$$I(\tau) = \left\langle | a_R E_1(t_R) + a_O E_1(t_O) |^2 \right\rangle \tag{2.6}$$

The time averaged bilinear products in the expansion of (2.6) are autocorrelation functions defined as $\Gamma_{11}(\tau)=\langle E_1(t_R)E_1^*(t_O)\rangle = \langle E_1(t')E_1^*(t'+2n(r_R-r_O)/c)\rangle = \langle E_1(t')E_1^*(t'+\tau)\rangle$. If $I_R = a_R a_R^*\Gamma_{11}(0)$ and $I_O = a_O a_O^*\Gamma_{11}(0)$ are the time averaged irradiances from the reference arm and from the object arm, $a_R a_O^*\Gamma_{11}(0) = \sqrt{I_R I_O}$ and the complex degree of coherence is $\gamma_{11}(\tau) = \dfrac{\Gamma_{11}(\tau)}{\Gamma_{11}(0)}$,[37] Eq.(2.6) becomes:

$$I(\tau) = I_R + I_O + 2\sqrt{I_R I_O}\,\mathrm{Re}[\gamma_{11}(\tau)] \tag{2.7}$$

The complex degree of coherence is written as

$$\gamma_{11}(\tau) = |\gamma_{11}(\tau)| \exp\{-j[\overline{\omega}\tau - \alpha(\tau)]\}$$

where $\overline{\omega}$ is the mean frequency of the light and α (τ) is a fringe phase function. This form of complex degree of coherence is chosen to give the cosinusoidal fringes that are observed in the measured signals, i.e., in the interferograms. Equation (2.7) can be rewritten in terms of the average irradiance $I_0 = I_R + I_O$ and the fringe visibility $K(\tau) = \dfrac{I_{\max} - I_{\min}}{I_{\max} + I_{\min}} = \dfrac{2\sqrt{I_R I_O}}{I_R + I_O} |\gamma_{11}(\tau)|$ as:

$$I(\tau) = I_0[1 + K(\tau)\cos(\overline{\omega}\tau - \alpha(\tau))] \tag{2.8}$$

The depth resolution of OCT is often taken (arbitrarily) as the full-width-half-maximum (FWHM) of the coherence function and thus the FWHM of the autocorrelation function. The autocorrelation function is the Fourier transform of the power spectral density (PSD) of the source S (ν):[37]

$$\Gamma(\tau) = \int_0^{\infty} 4S(\nu) e^{-j2\pi\nu\tau}\, d\nu \tag{2.9}$$

If the PSD of the source has a Gaussian shape with a full-width-half-maximum (FWHM) of $\Delta\nu$, then

$$S(\nu) = \frac{2\sqrt{2\ln 2}}{\sqrt{\pi}\,\Delta\nu}\exp[\,-(2\sqrt{\ln 2}\,\frac{\nu-\bar{\nu}}{\Delta\nu})^2\,] \qquad (2.10)$$

and from the Fourier transform relationship shown in Eq. (2.9), the complex degree of coherence is found to be

$$\gamma(\tau) = \Gamma_{11}(\tau)\,/\,\Gamma_{11}(0) = \exp[\,-(\frac{\pi\Delta\nu\tau}{2\sqrt{\ln 2}})^2\,]\exp(\,-j2\pi\bar{\nu}\tau\,) \qquad (2.11)$$

a Gaussian function with a FWHM of $\delta\tau = 4\ln 2\,/\,\pi\Delta\nu = 0.882/\Delta\nu$.

The depth resolution δz is the physical distance between two just resolvable reflectors. Since the reflected light travels twice through the object arm, the depth resolution should be half of the FWHM of the coherence function.[38] Thus the depth resolution δz for a reflective OCT system with a source that has a Gaussian line shape (i.e., a Gaussian PSD) is given by:

$$\delta z = \frac{c}{n_g}\frac{\delta\tau}{2} = \frac{2\ln 2}{\pi n_g}\frac{\lambda_o^{\,2}}{\Delta\lambda} \qquad (2.12)$$

where λ_o is the centre wavelength of the source, $\Delta\lambda$ is the FWHM of the power spectral density (PSD) of the source, and n_g is the group refractive index of the sample. To obtain the depth resolution, it was assumed that a Gaussian function that is displaced by one FWHM of a similar Gaussian function can be distinguished.

2.3.2 Coherence Function of a Multimode Diode Laser

The coherence function for a multimode diode laser is different than for a broad band source.

The above threshold output of a Fabry-Pérot laser is composed of a continuous spontaneous emission spectrum superimposed with peaks at the longitudinal modes of oscillation. Figure 2.5 (a) shows an idealized example as a plot of the logarithm of the output power as a function of wavelength. The modes of the laser are easily identified as the spikes that rise above the broad band spontaneous emission. For a Michelson interferometer system illuminated with such a source, the time averaged irradiance at the detector will be:

$$I(\tau) = \left\langle |\, a_R[E_s(t_R) + \sum_{i=-m}^{m} E_i(t_R)] + a_o[E_s(t_O) + \sum_{i=-m}^{m} E_i(t_O)]\,|^2 \right\rangle \qquad (2.13)$$

where t_R and t_O are the retarded times as defined near Eq.(2.5). E_s is the electric field for the spontaneous emission and E_i is the electric field for one of the $2m + 1$ modes.

The cross terms, $\langle E_s(t)E_i(t')\rangle, \langle E_i(t)\cdot E_j(t')\rangle, j \neq i,$ in Eq. 2.13 will average to zero owing to a lack of a time-independent phase relation between the *E* fields. Thus the output irradiance as a function of the delay time τ between the two arms of a two-beam interferometer illuminated by a multimode laser can be written as:[39]

$$I(\tau) = I_s[1 + K_s(\tau)\cos(2\pi\bar{v}_s\tau - \alpha_S(\tau))] + \sum_{i=-m}^{m} I_i[1 + K_i(\tau)\cos(2\pi\bar{v}_i\tau - \alpha_i(\tau))] \tag{2.14}$$

where I_s is the time averaged irradiance of the broadband spontaneous emission; $K_s(\tau)$ is the fringe visibility function for the spontaneous emission; $\bar{v}_s$ is the optical frequency at the peak of the spontaneous emission; I_i is the time averaged irradiance of mode *i*; $K_i(\tau)$ is the fringe visibility function for mode *i*; and, $\bar{v}_i$ is the optical frequency at the centre of mode *i*. For modes with a Lorentzian line shape, $K_i(\tau)$ is proportional to $\exp(-|\tau|/t_i)$ where t_i is the coherence time of the mode. If the spontaneous emission has a Gaussian shape, then K_s is proportional to $\exp[-\pi/2(|\tau|/t_s)^2]$ where t_s is the coherence time of the spontaneous emission. The α terms are the fringe phase functions and are zero for symmetric and smooth line shapes.

Equation 2.14 can be recast in the form of Eq. (2.8). The result is an overall fringe visibility (or coherence function, since the two are related) given by: [39]

$$K(\tau) = I_s K_s' + \sum_{i=-m}^{m} I_i K_i \cos(2\pi i\delta v\tau) \tag{2.15}$$

where δv is the mode spacing between longitudinal modes. Equation (2.15) can be manipulated to reveal the periodic nature of the coherence function. For a uniform distribution of mode intensities (i.e., $I_i = I_o$ and taking $K_i = K$), the fringe visibility looks similar to the far field of a uniformly illuminated diffraction grating and can be simplified in the same manner. The cosine functions in Eq. (2.15) can be written as complex exponentials and the sum over the modes can be evaluated as a geometric series. The fringe visibility for a laser with a mode spacing of δv and all $(2m + 1)$ modes of intensity I_o is found to be:

$$K(\tau) = I_s K_s' + I_o K\left\{\frac{\sin[(2m+1)\pi\delta v\tau]}{\sin(\pi\delta v\tau)}\right\} \tag{2.16}$$

Equation (2.16) has the periodic $\sin(Nx)/\sin(x)$ nature of a diffraction grating. The non-uniform intensities of the modes can be taken into account at the expense of a simple analytic expression. For a Gaussian distribution of modes intensity, the fringe visibility will be similar to the far field of an apodized diffraction grating.

The fringe visibility is plotted in Fig. 2.5(b) for a laser with a central wavelength of 1.55 μm and a mode spacing of 1.0 nm (125 GHz), parameters which are similar to the AMQW lasers that were used. The modal line width of each longitudinal mode was taken to be 0.05 nm (7 GHz). Seven longitudinal modes were used in the simulation shown in Fig. 2.5(b). A Gaussian-shaped spontaneous emission bandwidth of 117 nm (14.6 THz) was assumed.

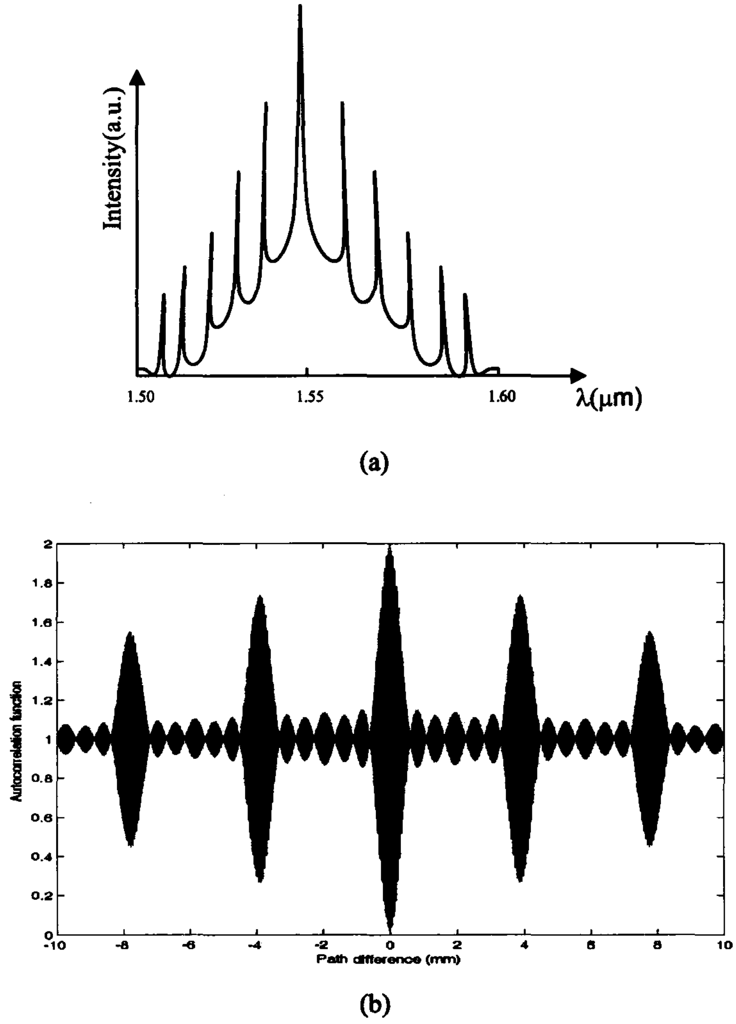

Figure 2.5 (a) Assumed time-averaged laser power spectrum (its envelope is corresponding to S (ν) in Eq. (2.16)). (b) Simulation result of the autocorrelation function of 7 longitudinal modes

Note that instead of having one central peak, as found for the autocorrelation function of an SLD, the coherence function has multiple peaks with a definite spacing. The coherence function for the 'sampled' output (the output of a multimode diode laser is not uniformly distributed in wavelength) is then a periodic function in depth. The coherence function of the envelope is replicated at each period owing to the periodic sampling by the modes. In analogy with the sampling of analog signals, the maximum depth of the sample, i.e., the measuring range Δz, is bounded. Therefore, when the source for an OCT system is a multimode laser, special attention has to be paid to the measuring range to determine unambiguously the depth information.

2.3.3 Wavelength Tuning Fourier Domain OCT with a Tunable Diode Laser

In wavelength-tuning Fourier domain OCT, the interferogram is recorded as a function of wavelength (λ) or equally wave number ($k = 2\pi/\lambda$) while the reference mirror is held in one position. In the wavelength-tuning Fourier domain OCT measurements that are reported here, a diffractive optical element (DOE) short external cavity (SXC) was used to step the emission wavelength of the AMQW laser over the longitudinal modes of the laser. Thus an essentially single frequency source is being used to make measurements of the interference between the reflectors in the sample and the reference mirror at a finite number of wavelengths. Depth discrimination is made by taking an inverse Fourier transform of the interferogram obtained by stepping the wavelength over the modes of the laser.

Since a single longitudinal mode has a well defined frequency, the electric field of the k^{th} mode is written as $E_k(t)e^{j\omega_k t}$. $E_k(t)$ is taken as a function of t to allow for amplitude and frequency fluctuations. If the reflectors in the sample are allowed to be distributed in depth (i.e., allow $a_O(z)$ to be a function of z), then the detected signal I_k for a given wave number k is

$$I_k = \left\langle \left| a_R E_k(t_R) e^{j\omega_k t_R} + \int_0^\infty a_O(z) E_k(t_O) e^{j\omega_k t_O} dz \right|^2 \right\rangle \tag{2.17}$$

where t is the relative time delay. Expansion of Eq. (2.17) leads to

$$I_k = a_R^2 \left\langle E_k^2(t_R) \right\rangle + \left\langle \left| \int_0^\infty a_O(z) E_k(t_O) e^{j\omega_k t_O} dz \right|^2 \right\rangle + 2\mathrm{Re}\left\langle \int_0^\infty a_R^* a_O(z) E_k^*(t_R) E_k(t_O) e^{j\omega_k (t_O - t_R)} dz \right\rangle \tag{2.18}$$

The first term yields the time averaged irradiance from the reference arm. The second term is the time average of the interference of the light that is reflected from the reflectors in the object arm. The third term is the interference of the light from the reference arm with the light from the object arm. A change of variables from $t = 2nz/c$ to path length difference z yields:

$$I_k = a_R^2 S_k + \int_0^\infty \int_0^\infty a_O(z) a_O^*(z') \Gamma_{11}(z - z') e^{-j2kn(z-z')} dz dz' + 2\mathrm{Re}(a_R^* \int_0^\infty \Gamma_{11}(z) a_O(z) e^{-j2knz} dz) \tag{2.19}$$

where S_k is the power spectral density for the k^{th} mode of the laser.

To determine the depth information in the sample $a(z)$ by Fourier transformation, $a(z)$ is replaced with the symmetric expansion $\hat{a}(z) = a_O(z) + a_O(-z)$.[40] Equation (2.19) becomes

$$I_k = a_R^2 S_k + \frac{1}{4} \int_{-\infty}^{\infty} \int_{-\infty}^{\infty} \Gamma_{11}(z - z') \hat{a}(z) \hat{a}(z') \exp^{-j2kn(z-z')} dz dz' + \mathrm{Re}(a_R^* \int_{-\infty}^{\infty} \Gamma_{11}(z) \hat{a}(z) \exp^{-j2knz} dz) \tag{2.20}$$

The second term is a convolution, and thus Eq. (2.20) can be written as

$$I_k = a_R^2 S_k + \frac{1}{4}\int_{-\infty}^{\infty}\Gamma_{11}(z)[\hat{a}(z)\otimes\hat{a}(z)]\exp^{-j2knz}dz + \mathrm{Re}(a_R^{*}\int_{-\infty}^{\infty}\Gamma_{11}(z)\hat{a}(z)\exp^{-j2knz}dz) \tag{2.21}$$

where ⊗ indicates convolution. It is clear that the three terms are in the form of Fourier transforms (the first term is the Fourier transform of a delta function). The depth information $\hat{a}\,(z)$ of the sample is obtained by taking the inverse Fourier transform of the sequence of numbers I_k, where the sequence is obtained by recording the output of the interferometer for each mode of the laser and for the reference mirror fixed in one plane. Here $\Gamma_{11}(z)$ is the autocorrelation function of the light source. For a single longitudinal mode, $\Gamma_{11}(z)$ is the same as S_k in the first term of Eq.(2.21), if one ignores the time-related noise from the light source. Thus, the inverse Fourier transform of the sequence of numbers I_k yields:

$$F^{-1}\{I_k\} = F^{-1}\{S_k\}\otimes[a_R^2\delta(z) + \frac{1}{8}\hat{a}(z)\otimes\hat{a}(z) + \frac{1}{2}\mathrm{Re}(\hat{a}(z))] \tag{2.22}$$

The first term in the square bracket is a delta function. The second term is the autoconvolution of the signal $\hat{a}$ (z), which equals the autocorrelation. The third term $\hat{a}$ (z) is the desired signal, which is related to the reflectance from the object as a function of the depth z. All of the three terms in the bracket are convolved with the inverse Fourier transform of the PSD of the source S_k, which is proportional to the complex degree of coherence of the source as shown in Eq. (2.11). Both the first and second terms locate around $z = 0$ in the plot of backscattering amplitude *vs.* depth from the surface of the sample. To avoid the signal term (the third term) overlapping with these two terms, it is necessary to place the reference mirror a distance ($z \cong 50$ μm) in front of the surface of the sample so that the desired signal $\hat{a}$ (z) and the central peak will be separated.

Because of the Fourier transform relation between the interferogram and the cross-section reflectance *a(z)*, and the discrete nature of the measurements at the wavelengths corresponding to the longitudinal modes of the laser, an unambiguous measuring range is determined by the mode spacing of the tunable laser. According to the Nyquist sampling theorem[41], one must sample at least twice per period of the largest frequency in the object to avoid aliasing and hence to reconstruct the object. In wavelength tuning Fourier domain OCT, the interferogram is measured (i.e., sampled) at the optical frequencies (or wave numbers; the modes are roughly uniformly spaced in wave number or equivalently optical frequency) corresponding to the modes of the laser. A single reflector located a distance Δz behind the reference mirror will create a fringe of $\cos(2kn\Delta z)$ in the interferogram. If two consecutive modes of the laser have wave numbers k_1 and k_2, then the maximum value of Δz, given that there must be at least two measurements per period in the interferogram, is given by

$$\Delta z < \frac{\pi}{2(n(k_2)\cdot k_2 - n(k_1)\cdot k_1)} \approx \frac{1}{4n_g}\frac{\lambda_o^2}{\delta\lambda} \tag{2.23}$$

where $n_g = n - \lambda dn/d\lambda$ is the group refractive index of the sample. The measuring range for a Fabry-Pérot laser with a centre wavelength of λ_o and a mode spacing of $\delta\lambda$ is thus

Δz. This places a requirement on the design of an AMQW laser source for wavelength tuning Fourier domain OCT.

The mode spacing $\delta\nu$ in Hz for a laser of length L and group refractive index (of the laser) n'_g is given by $\delta\nu = c/(2n'_gL)$. Using the relation $\delta\nu/\nu_o = -\delta\lambda/\lambda_o$, the mode spacing is found in terms of wavelength as $\delta\lambda = \lambda_o^2/(2n'_gL)$ nm. This expression for the mode spacing may be substituted in Eq.(2.23) to determine the minimum length of a laser L that is required for a given measuring range as $L = \Delta z\, 2\, n_g / n'_g$. A specified measuring range determines a minimum length for the AMQW laser. This impacts the design of the active region of the AMQW through the need to operate at or near the TCL for a maximum tuning range and hence for a minimum depth resolution δz as shown by the $1/(\Delta\lambda)$ in Eq.(2.12).

The depth resolution δz is determined by the width of the coherence function, which is the same result as for broad band sources. This is apparent from Eq. (2.22) where the coherence function is convolved with the depth information. Scattering centers that are closely spaced as compared to the width of the coherence function will be washed out and will not be obvious in the inverse Fourier transform of the interferogram.

2.4 Application to Fourier Domain OCT

Figure 2.6 is the schematic of the Fourier domain OCT imaging system that was used to test the AMQW lasers. An uncoated AMQW laser with cavity length of 800 μm was mounted onto a copper heat sink with temperature control provided by a thermoelectric cooler. The laser was operated under CW conditions at a DC bias current of 160 mA and at a temperature of 18 ^{0}C. The DOE was mounted on a piezoblock (PZT) behind the back facet of the laser and the PZT was then mounted on a micrometer stage with translational control in the x, y, and z directions and rotational control of angles. A He-Ne reflection off the back of the DOE was aligned to a reflection off the laser facet to fix the rotational degree of freedom. Thus the face of the DOE was aligned to be parallel to the laser facet. Next the x- and y-axis translational alignments were optimized by monitoring the single longitudinal mode operation with the aid of a scanning monochromator. Once single longitudinal lasing mode was achieved, the laser could be tuned by linearly translating the DOE position.

Detector 1, the lock-in amplifier, the PZT, and interconnections formed a phase sensitive feedback control loop that provided stable, single mode operation of the laser during the process of data acquisition.[42,43] A 10 kHz signal was applied to the piezo voltage for the modulation/demodulation technique in the feedback control loop. An integrator circuit was used to maintain lasing on the selected F-P mode using the output of a lock-in amplifier referenced to the DOE modulation frequency. The single longitudinal mode could be kept stable for long term under this feedback control loop.

The PZT with the DOE was translated by a stepper motor driven stage for the broad band tuning. The tuning wavelength was from 1.488 μm to 1.605 μm. The tuning wavelength could be read from the wavelength meter. The Michelson interferometer was built with a beam splitter (BS2) to give a reference arm and an object arm. The interferogram is constructed by the interference of the reflections from the object arm with light from the reference arm. Detector 2 converts the optical signal to an electrical signal.

I measured a glass cover slip with the wavelength tuning Fourier domain OCT setup and AMQW DOE SXC source. Figure 2.7 (a) shows the schematic of the reflections from the cover slip. The light impinges from the right and roughly 4% of the optical power reflects from the front and back surfaces of the glass. Provided that the thickness of the glass is $< \Delta z = 1.2$ mm, I expect to recover two reflections spaced by the thickness of the glass cover slip. As noted in Sec. 2.3.3, it is necessary to consider the depth of the coherence function and place the reference mirror a distance in front of the surface of the sample to separate the signal and the central peak. Figure 2.7 (b) shows the interferogram with the AMQW DOE SXC source by tuning from 1488 nm to 1605 nm over 119 modes by using every other single longitudinal mode spacing of $\delta\lambda \approx 1$ nm. Figure 2.7 (c) is the Fourier transform of the interferogram of Fig. 2.7 (b). Figure 2.7 (d) is the Fourier transform of the interferogram with a single longitudinal mode spacing of $\delta\lambda = 0.426$ nm. One can see the central peak in Fig. 2.7 (c) and (d), which is the Fourier transform of the source PSD spectrum and should be removed when building the final image.[40] The measuring range is doubled if the mode spacing is halved as shown in Eq. (2.23) and as demonstrated in Fig. 2.7 (d). The two peaks beyond the central peak correspond to the reflections from the front and back facets of the cover slip respectively. I estimate from the data of Fig. 2.7 (c) that the thickness of the cover slip is 144 μm ± 2 μm and from Fig. 2.7(d) that the thickness is 150 μm ± 4 μm, compared with the mechanical measurement of 146 μm ± 4 μm.

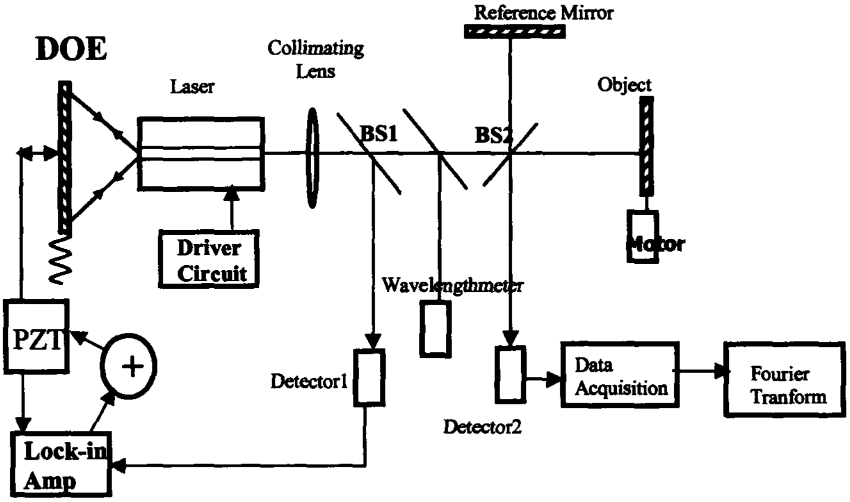

Figure 2.6 Schematic of Fourier domain OCT

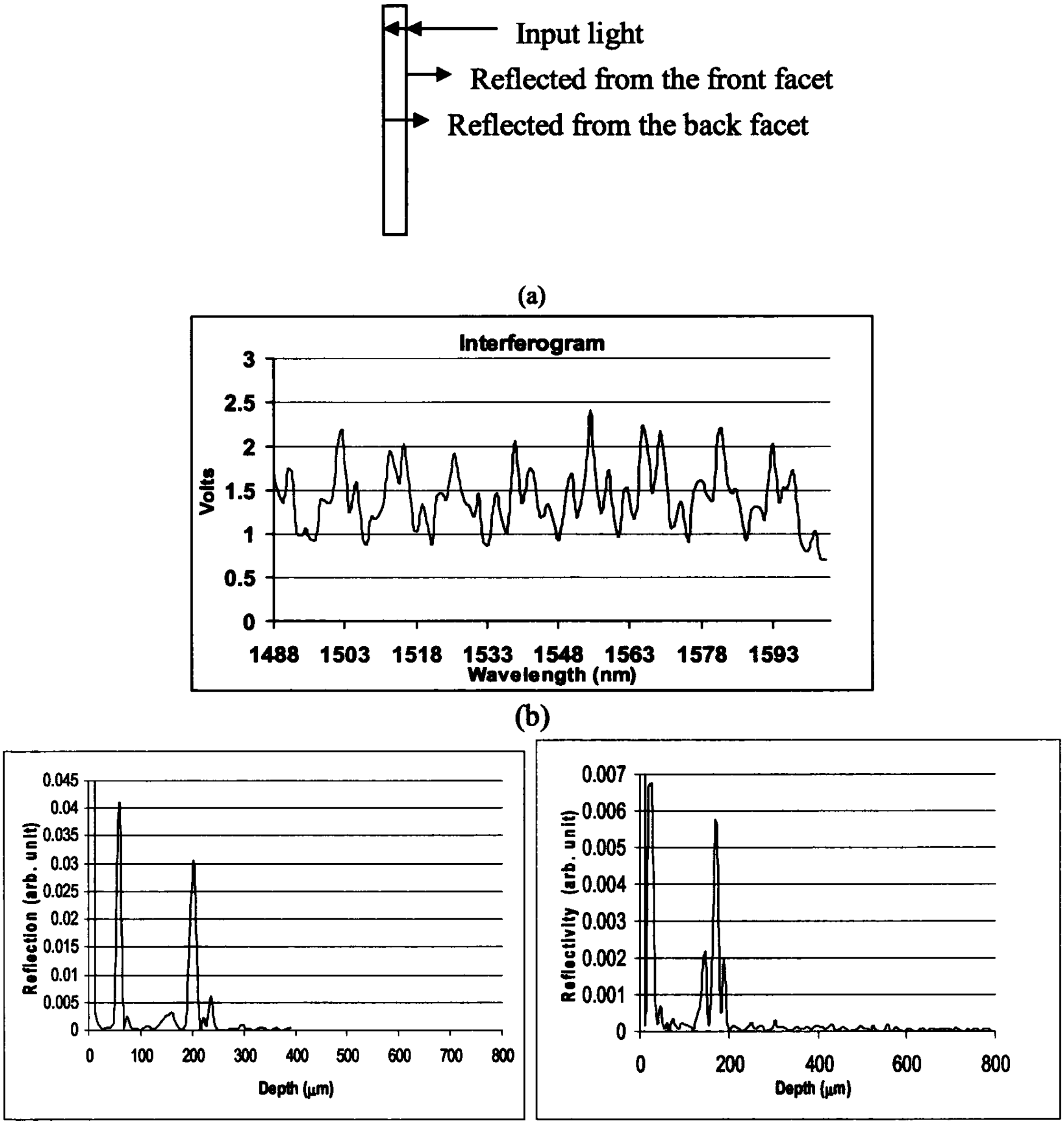

(a)

(b)

(c) (d)

Figure 2.7 (a) Schematic of reflection from a glass cover slip (b) Interferogram of the glass cover slip by tuning the AMQW laser from 1488 nm to 1605 nm over 119 modes (c) Recovered signal from an interferogram from a cover slip obtained with a laser with a mode spacing of 1 nm (d) Recovered signal from an interferogram obtained with a laser with a mode spacing of ~0.5 nm

2.5 Application to Synthesized OCT (SOCT)

The setup for SOCT is schematically shown in Fig. 2.8. The DOE was driven by an electrically controlled magnetic voice coil actuator which could be modulated up to 100 Hz while keeping the DOE well aligned. The lock-in amplifier worked as a low-pass filter to time-average the signal from the detector. When the time constant of the low-pass filter was longer than one period of the modulation of the SXC, the synthesis of a low coherence function from a coherent source was achieved. In SOCT, both depth scanning of the reference mirror and the lateral scanning are needed for 2D image construction. Compared with an SLD, a tunable laser as the source for SOCT provides higher power spectral density and higher brightness, which provide easier coupling to optical fibre.

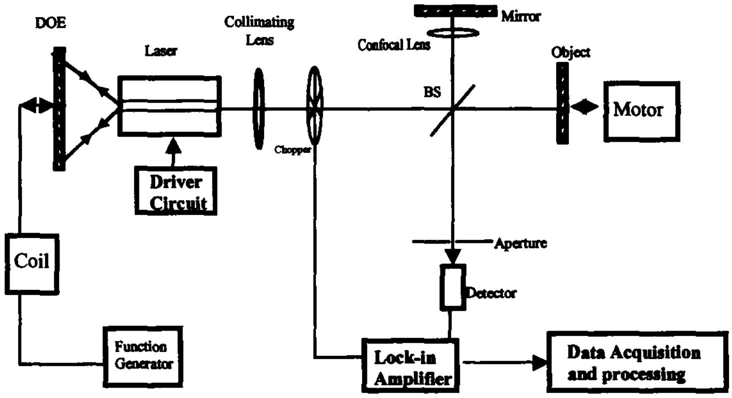

Figure 2.8 Schematic diagram of a DOE enabled tunable AMQW diode laser for synthesized OCT

The synthesized coherence function is multi-peaked with a definite spacing. Therefore the measuring range must be limited to avoid 'aliasing'. A confocal spatial filter, which is composed of a lens in the reference arm and an aperture in front of the detector, can be used to minimize the effects (i.e., the aliasing) of the secondary peaks in the coherence function on the depth resolution.[44]

Figure 2.9 shows an interferogram with mirrors in both the sample arm and reference arm. The DOE was modulated at a frequency of 100 Hz. The corresponding RC time constant on the lock-in amplifier was set to be 30 ms. The RC time constant, which is inversely related to the bandwidth of the low-pass filter of the lock-in amplifier, must be longer than the period of the DOE modulation for adequate averaging. Figure 2.9(a) shows the synthesized coherence function of the tunable DOE SXC AMQW laser measured with mirrors in both of the arms. It is clearly shown that the coherence function has multiple peaks when the displacement of the reference mirror is greater than several millimetres. Figure 2.9 (b) shows the central peak with a path length difference of −70 μm to +70 μm. The side-lobes are consistent with the side-lobes in the simulation result shown in Fig. 2.5 (b). Figures 2.9 (c)-(e) shows that when the tuning range of the external cavity laser is larger, the coherence length (l_c) will be shorter. Thus the depth resolution will be higher with a broader tuning range. The coherence length that I measured is consistent with the theoretical expectation for a Gaussian envelope of the intensities of the modes, which is given by Eq. (2.12) with a centre wavelength λ_o = 1550 nm and a corresponding tuning range.

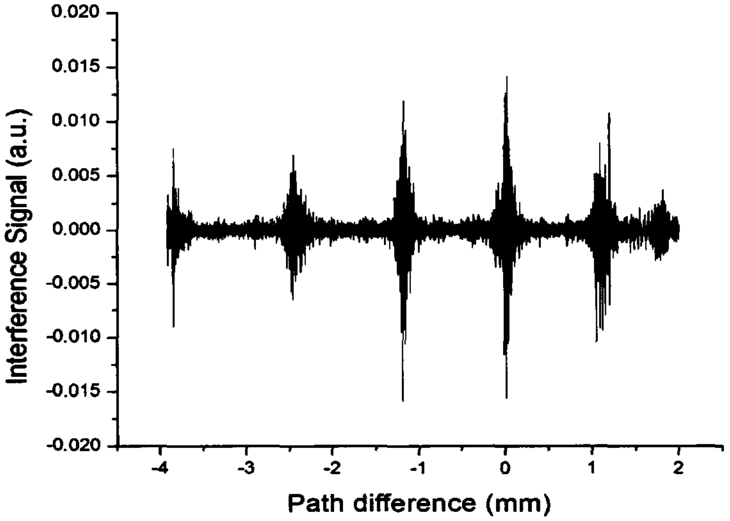

(a)

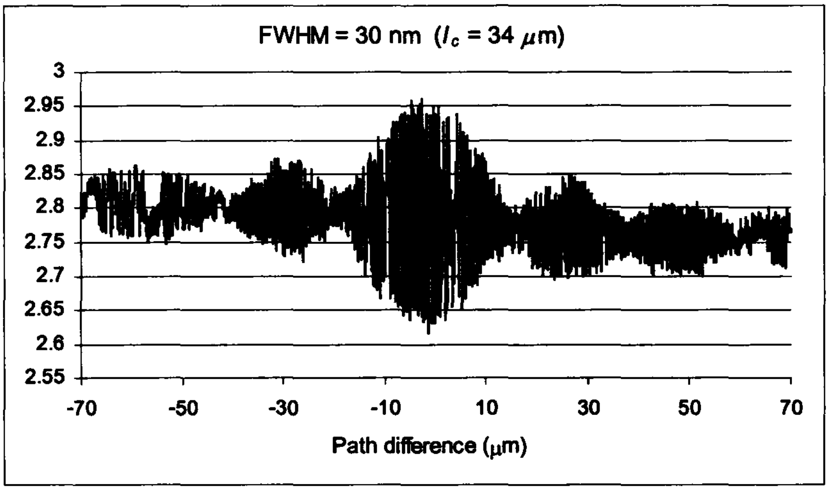

(b)

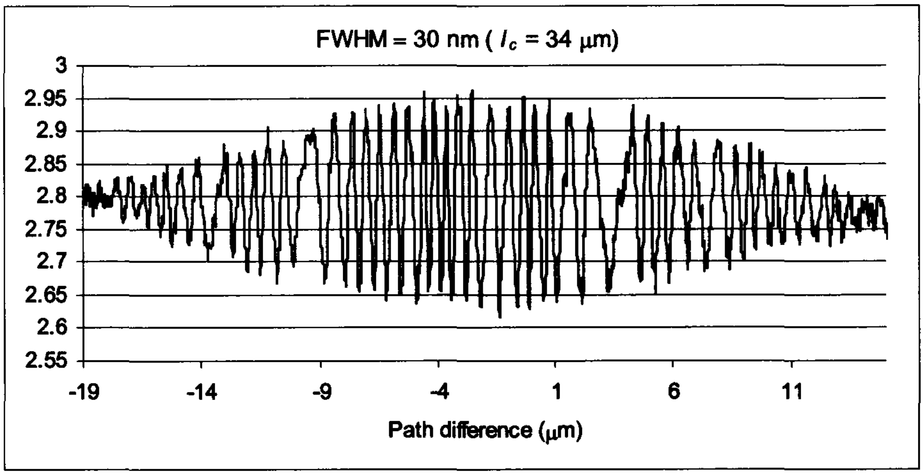
FWHM = 30 nm (l_c = 34 μm)
3
2.95
2.9
2.85
2.8
2.75
2.7
2.65
2.6
2.55
-19
-14
-9
-4
1
6
11
Path difference (μm)

(c)

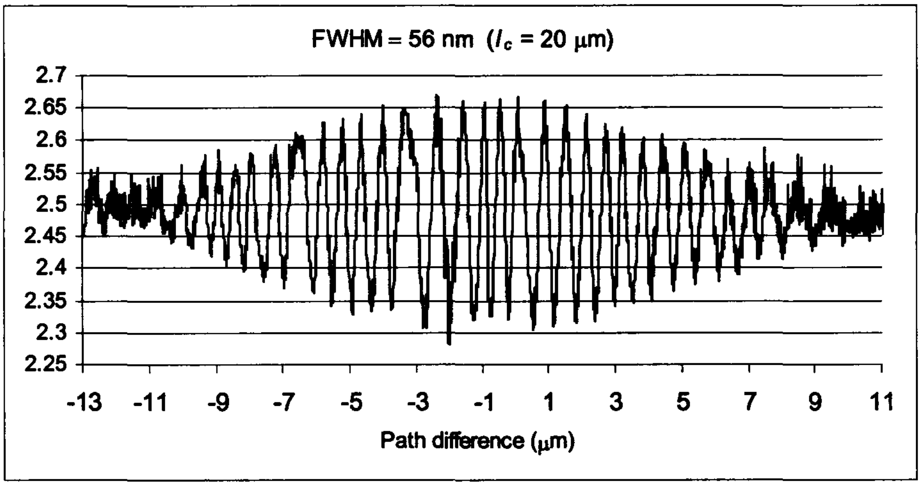
FWHM = 56 nm (l_c = 20 μm)
2.7
2.65
2.6
2.55
2.5
2.45
2.4
2.35
2.3
2.25
-13
-11
-9
-7
-5
-3
-1
1
3
5
7
9
11
Path difference (μm)

(d)

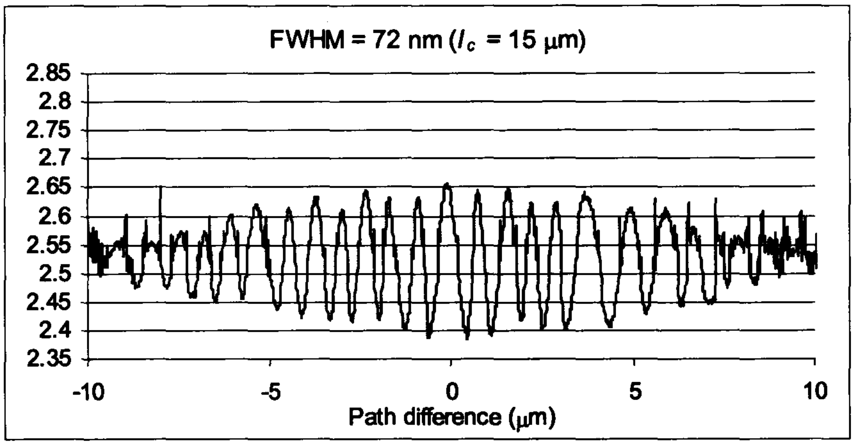

(e)

Figure 2.9 When the tuning range of the external cavity laser is larger, the coherence length will be shorter. (a) Interference fringe by scanning the reference mirror over a wide range for SOCT. (b) Record of the central peak over a path difference of -70 μm to 70 μm for averaging over a FWHM of 30 nm. (c) Record of the central peak of the interference fringe to show the depth resolution is around 34 μm for averaging over a FWHM of 30 nm. (d) Depth resolution is around 20 μm for averaging over a FWHM of 56 nm. (e) Depth resolution is around 15 μm for averaging over a FWHM of 72 nm.

The best depth resolution I could achieve with this particular design of an AMQW tunable laser is 13 μm in air corresponding to a FWHM of 80 nm. Figure 2.10 shows the results of measuring the same cover slip as I did for wavelength tuning Fourier domain OCT. The raw data was processed with a bandpass filter, rectifier, and finally a low pass filter, which were realized with software in the data processing. The distance between the two peaks shows the thickness of the cover slip. Both the wavelength tuning Fourier domain OCT and the synthesized OCT gave the thickness of the cover slip as 145 μm ± 5 μm.

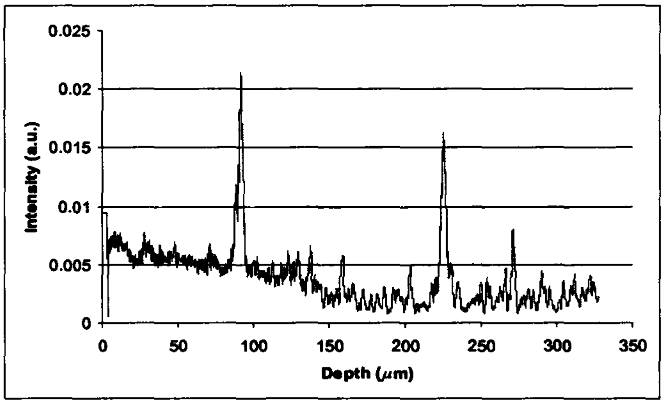

Figure 2.10 Measurement result of a glass cover slip for synthesized OCT with averaging over FWHM of 80nm

2.6 Conclusion

I applied a broadly tunable asymmetric multiple-quantum-well (AMQW) laser in a diffractive optical element (DOE) short external cavity (SXC) for both time-domain and Fourier-domain OCT. The depth resolution of synthesized OCT depended on the tuning range of the AMQW laser and could be as small as 13 μm in air corresponding to a FWHM of 80 nm (maximum tuning range of 117 nm) for this particular design of an AMQW laser. A tuning range of 117 nm is not the limit of the tuning range of AMQW lasers. A tuning range of 170 nm for a different AMQW design has been achieved.[23] Improvements in the ability to tune AMQW lasers should result in improvements in the performance of OCT based instruments.

Superluminescent diodes (SLDs) are required for time domain OCT. The broad gain profile of an AMQW active region also makes AMQW active regions ideal candidates for SLDs. The requirements for a time domain OCT light source include broad spectral width, reasonable output power, and low ripple. In Chapter 3, I introduce the work on the optimization of SLD waveguides. The goal of the optimization is to maximize the confinement factor of the SLD waveguide to improve the output power. A double section waveguide was chosen for the SLD structure. It is shown that the back section works as an absorber for the SLD; thus the ripples could be better suppressed. In Chapter 4, the design considerations for the active region of an AMQW SLD are introduced. Through calculations of gain, it was found that the transition carrier density (TCD) is a critical parameter to obtain high output power for an SLD.

3 Waveguide Optimization for SLD

3.1 Introduction

As discussed in Chapter 1, depth resolution and sensitivity are two important parameters in the design of a high resolution OCT system. For time domain OCT, compared with short pulse solid state lasers, superluminescent diodes (SLDs) have the advantages of low shot noise and near ideal Gaussian spectral shape. In the next two chapters, the work targeting the design and realization of broad spectral width and high power AMQW SLDs centered at 1300 nm is covered. This work can be divided into two parts: the waveguide optimization, which is discussed in Chapter 3, and the active region design and the measurements, which are presented in Chapter 4.

In this chapter, I introduce the research work on the waveguide structure optimization and double-section mask design for the AMQW SLD centered at 1300 nm. The waveguide structure optimization targets maximization of the optical confinement factor Γ. The optical confinement factor is defined as the fraction of the mode energy contained in the active region that is available for interaction with the injected carriers. A high confinement factor improves the modal gain. In a ridge-waveguide structure, the light output is in the form of a narrow beam with an elliptical cross section. The field distribution across the beam takes certain well-defined forms called spatial modes. A spatial mode is the specific solution of Maxwell's equations that satisfies all the boundary conditions imposed by the laser structure. In the general multimode case the optical field is denoted by E_{pq}, where p and q stands for the *transverse* and *lateral* modes specifying the field distribution in the direction perpendicular and parallel to the junction plane respectively. For the application for OCT, it is often desirable to design either semiconductor lasers or SLDs that emit light predominantly in the fundamental spatial mode because of high coupling efficiency of the fundamental mode into single mode fibres. For this reason, only the fundamental mode is considered in the optimization of the confinement factor in this chapter.

A ridge-waveguide structure was adopted for the SLD device which was designed and processed for application to OCT. The ridge-waveguide structure will be introduced in Section 3.1.1. The calculation of the refractive index and the approximations in the calculation are introduced in Section 3.1.2. To calculate the confinement factor, the optical field in a 2D dielectric waveguide was solved with the effective index method. This is realized by solving the effective index of the centre region and the shoulder region of the ridge-waveguide structure with a transfer matrix method. The multi-layer planar optical waveguide in the transverse (or y direction, in Fig. 3.1) direction is solved with a transfer matrix method, and then an effective index method was solved for the 3-layer waveguide in the lateral (x in Fig. 3.1) direction with a calculated effective index. Once the optical field is known, the confinement factor is calculated. This calculation is introduced in Section 3.2. Optimization of the confinement factor is done by a Marquardt nonlinear least-squares fitting method. In the nonlinear fitting procedure, the confinement factor is taken as a numerical function of the layer thickness in the growth direction.

3.1.1 Ridge Waveguide Structure

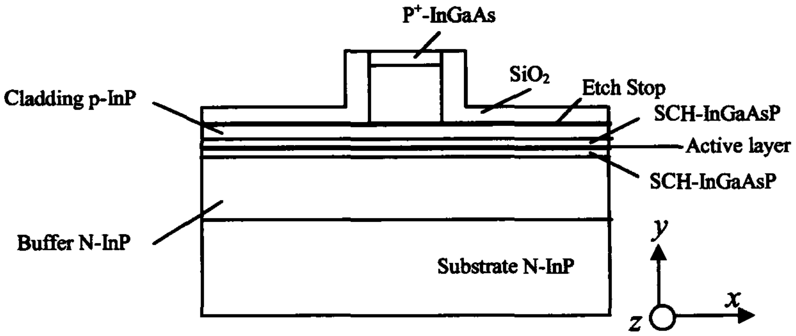

Figure 3.1 Ridge waveguide InGaAsP/InP SLD

A ridge-waveguide structure belongs to the group of weakly index guided waveguide structures[45]. The ridge stripe was tilted seven-degrees to minimize the reflectance from the cleaved facet. An inclined angle of seven degrees should theoretically reduce the facet reflectivity to < 10^{-6}.[46] A cross section of the structure of a conventional ridge waveguide heterostructure InGaAsP/InP MQW diode laser is shown in Fig. 3.1. The bottom of the structure is an InP substrate with n-type doping. Above the buffer layer, undoped separate confinement heterostructure (SCH) layers are grown surrounding an active region, which consists of quantum-wells and barrier layers. The top of the device is p-type InP cladding material. A ridge structure is etched into the cladding material until the etch stop layer to create an optical waveguide to confine the laser mode spatially. A SiO_2 layer, which is normally 0.1 μm thick, is re-grown on top of the etch stop layer in the shoulder region for the purpose of current isolation. Metal contacts are deposited on the top and bottom of the device for the injection of carriers into the active region.

Three SLD wafers centered at 1300 nm were grown and processed for the OCT application. Wafer #3979 and wafer #4177 were grown by gas-source, molecular beam epitaxy (MBE) at McMaster University, and wafer #M0446 was grown by metal-organic chemical deposition (MOCVD) at the CPFC through the CMC. The structures are shown in Appendix A. The layers for SLD wafer #M0446 are shown in Table 3.1 to demonstrate the calculation of the confinement factor in this chapter.

Table 3.1 Structure of an SLD centered at 1300 nm (wafer # M0446)

Layer type	Doping (cm^{-3})	Thickness (Å)	$In_{1-x}Ga_xAs_yP_{1-y}$ composition x	y	Strain (%)	Refractive index (λ = 1.3 μm)	PL peak at 300 K (nm)
Contact layer	P^{++}1E19	2000	0.47	1.0	0.01	3.55	
Cladding	P^{+} 1E18	12600			0	3.209	
Cladding	P 4E17	2000			0	3.209	
Etch stop	P 4E17	50	0.28	0.61	-0.01	3.52	
Cladding	P 3E17	800			0	3.209	
SCH	P 2E17	700.0	0.08	0.18	0	3.280	
SCH	P 1E17	700.0	0.14	0.31	0	3.336	
Barrier		200.0	0.17	0.32	0.16	3.338	
Well		50.0	0.17	0.62	-0.81	*3.573+*i* 0.053	1326.5
Barrier		75.0	0.17	0.32	0.16	3.338	
Well		50.0	0.17	0.54	-0.55	3.474	1246.4
Barrier		200.0	0.17	0.32	0.16	3.338	
SCH	N 1E17	700	0.14	0.31	0	3.336	
SCH	N 4E17	700	0.08	0.18	0	3.280	
Buffer	Si-n 1E18				0	3.209	
Substrate	S-n 1E18				0	3.209	

* explained in the text in section 3.1.2 marked as '*'

3.1.2 Refractive Index of InGaAsP Layers

The refractive index of $In_{1-x}Ga_xAs_yP_{1-y}$ depends on the wavelength, crystal composition, lattice mismatch, doping level, carrier density and temperature. For the quaternary $In_{1-x}Ga_xAs_yP_{1-y}$ that is lattice matched to the InP substrate, the composition of Ga and As has to obey the relation:[47]

$$x = 0.1894y/(0.4184 - 0.013y) \qquad (3.1)$$

According to B. Groberg and S. Lindgren,[48] the refractive index of $In_{1-x}Ga_xAs_yP_{1-y}$ lattice matched to InP in the transparent region follows:

$$n = [1 + \frac{E_d}{E_0} + \frac{E_d E^2}{E_0^3} + \frac{\eta E^4}{\pi}\ln(\frac{2E_0^2 - E_g^2 - E^2}{E_g^2 - E^2})]^{1/2} \qquad (3.2)$$

where

$$\eta = \pi E_d / 2E_0^3(E_0^2 - E_g^2),$$
$$E_0 = 0.595x^2(1-y) + 1.626xy - 1.891y + 0.524x + 3.391,$$
$$E_d = (12.36x - 12.71)y + 7.54x + 28.91,$$
$$E = 1.240/\lambda$$

where λ is the light wavelength in μm and *E* is the light energy in *Ev*. E_0 and E_d are the single oscillator parameters that are obtained from data for the four constituent binaries by interpolation with Vegard's rule. The equations fit for room temperature. The effect of strained layers such as the QWs and the barrier layers that are lower than ±1% is ignored because the thickness of these layers is << the wavelength of the light that is produced.

*The index of refraction in the active region layers needs a more sophisticated model that takes into account the band structure of the layers, interband transitions, as well as many body effects to calculate the complex dielectric constant above the transparent region[49]. However, the index variations in the QWs will only provide a small perturbation on the overall optical mode calculation because of the very small thickness of QW layers. Therefore, in this thesis, an approximation is made by averaging the index of the active region and ignoring the refractive index perturbation of the active region layers for above the transparent region.

The refractive indices at a wavelength of 1.3 μm are shown in Table 3.1 and were calculated with the above equations. The index of SiO_2 was taken as 1.46 at a wavelength of 1.3 μm. The calculation did not include the effects of free carriers and doping. Because the thicknesses of the QWs and barriers are < 10 nm and the wavelength of the light that is produced at 1.3 μm is much greater than the layer thicknesses, I use an average value of the index of the active region, computed as:

$$n_1 = \frac{\sum_i l_i \times n_i + \sum_k l_k \times n_k}{\sum_k l_k + \sum_i l_i} \tag{3.3}$$

where $l_{i,k}$ is the layer thickness, $n_{i,k}$ is the index of the corresponding layers, *i* labels the QW, and *k* labels the barriers. This approximation for the index of the active region takes an average over the thickness of all five quantum wells and four barrier layers, but does not include the outermost barriers or SCH layers.

3.1.3 Confinement Factor

The confinement factor is calculated from the expression by knowing the optical field distribution *E(x,y)*:

$$\Gamma = \frac{n_1}{n_{eff}} \frac{\int_{-a}^{a}\int_{-b}^{b} |E(x,y)|^2 dxdy}{\int_{-\infty}^{\infty}\int_{-\infty}^{\infty} |E(x,y)|^2 dxdy} \tag{3.4}$$

where n_I is the averaged refractive index of the active region calculated with Eq.(3.3) and n_{eff} is the effective index of the waveguide. The width × height of the active region is taken to be $2a \times 2b$.

3.2 Confinement Factor Calculation

The effective index method[50] was applied to determine the optical mode profile of the ridge waveguide as shown in Fig. 3.2.

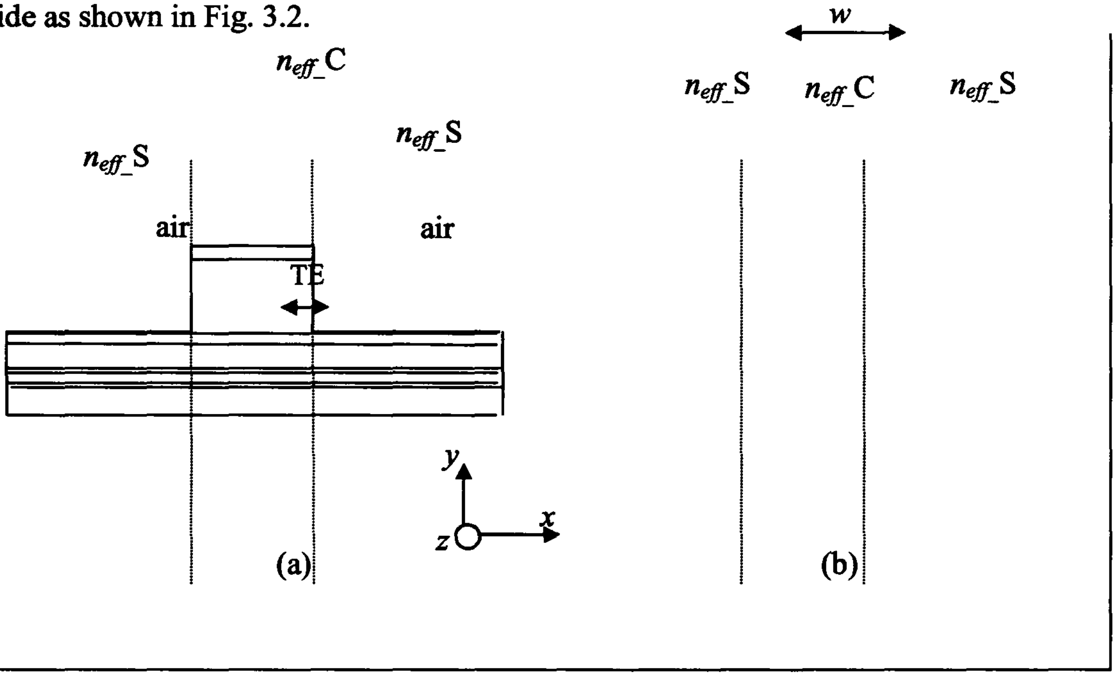

Figure 3.2 Schematics of solving 2-D ridge waveguide with arbitrary layers in the growth direction

The effective index method is an approximate method for solving 2-D rectangular waveguides and requires the solution for two slab waveguides. For the TE-polarized mode, the electric field E_x which is parallel to the lateral (x) direction is the dominant component. It was shown by Zory[51] that the TM gain in a compressively strained quantum well is drastically suppressed due to the effective removal of the LH subband transitions and thus TE polarization dominates in our SLD structure. To determine $E(x,y)$, first, a transfer matrix method[52] was first applied to find the fundamental spatial mode for the ridge area and the shoulder area respectively. Thus the electric field $G(y)$ for the fundamental mode is obtained and from this, the effective index in the ridge area n_{eff}_C and the effective index in the shoulder area n_{eff}_S, are obtained, as shown in Fig. 3.2(a). Next, a three layer slab waveguide problem is solved in the transverse direction as shown in Fig. 3.2 (b). This slab waveguide has three layers with indices n_{eff}_S, n_{eff}_C, and n_{eff}_S, with the E_x component perpendicular to the slab boundaries. Therefore, the guidance condition for the TM modes for the three layer slab waveguide is applied. The optical field distribution varies with both *x* and *y* direction, which is noted as *F(x,y)*. Thus the total optical field E_x is written as $E_x(x,y) \approx F(x,y)G(y)$.

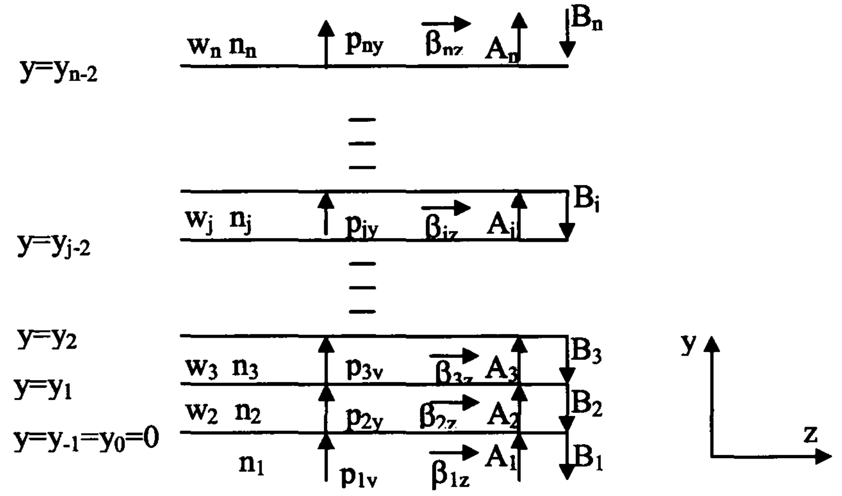

Figure 3.3 General form of a multilayer structure. Each layer (j) is of uniform index n_j. A_j and B_j are forward and backward propagation wave amplitudes. W_j is the layer thickness.

The transfer matrix method that was adopted in this thesis is described in Ref. 52. The method is for solving a planar optical waveguide which consists of stratified constant-index layers with parallel boundaries; see Fig. 3.3. p_{jy} is the propagation constant in y direction and β_{jz} is the propagation constant in z direction. The method is based on the assumption that, in order for the structure to behave as a waveguide, the energy flow has to be parallel to the layer boundaries. In the direction normal to the boundaries, the structure must behave as a resonator which means that there is no net energy flow in this direction.

Suppose that each layer has forward- and backward-propagating plane waves with amplitude A_i and B_i in the direction normal to the boundary, as shown in Fig. 3.3. The amplitude and the phase of these plane waves are related to the plane waves in the neighbouring layers by the continuity condition of the transverse electric and magnetic fields at the boundaries. This will build a matrix. When the boundary conditions are applied to the waves in the subsequent layers, and finally to the forward and backward waves of the unconfined superstrate and substrate regions, a 2×2 transfer matrix will be obtained relating the amplitude and the phases of the forward and backward waves in the superstrate region (A_1 and B_1) to those in the substrate region (A_n and B_n). In order to satisfy the resonance condition, the amplitude of the forward plane wave in the substrate A_1 and the amplitude of the backward plane wave in the superstrate B_n must have zero amplitude. This requirement will force one element in the transfer matrices to be zero, as shown in the following equation:

$$\begin{bmatrix} A_n \\ 0 \end{bmatrix} = \begin{bmatrix} \alpha_1 & \alpha_2 \\ \alpha_3 & \alpha_4 \end{bmatrix} \begin{bmatrix} 0 \\ B_1 \end{bmatrix} \tag{3.5}$$

Equation (3.5) can be satisfied only if the element α_4 of the matrix is equal to zero. α_4 is a function of the propagation constant β_z. Therefore, if the index profile of a waveguide is known, the effective index $n_{eff} = \beta_z/k_0$ of the waveguide can be determined by solving $\alpha_4(\beta_z/k_0) = 0$, where $k_0 = 2\pi/\lambda_0$ is the wave number in free space.

When this zero transfer-matrix element condition is satisfied, the propagation constants (in the direction normal to the boundary)of the two remaining nonzero waves in the substrate and the superstrate regions are imaginary. Thus the fields in these two regions are evanescent, which matches the requirement for guided-wave modes. Therefore, this method is also called the zero-element method.

To obtain the effective index n_{eff}, a numerical method was used to solve the equation $\alpha_4(\beta_z/k_0) = 0$. Because it is known that the effective index is in between the maximum index and minimum index of the layers, a plot of α_4 as a function of refractive index was achieved according to the transfer matrix method. There will be a point at which α_4 is real and is zero if the structure performs as a waveguide. Figure 3.4 shows the plot of α_4 *vs* refractive index. α_4 is complex when the refractive index is smaller than 3.225 and is not shown in the figure.

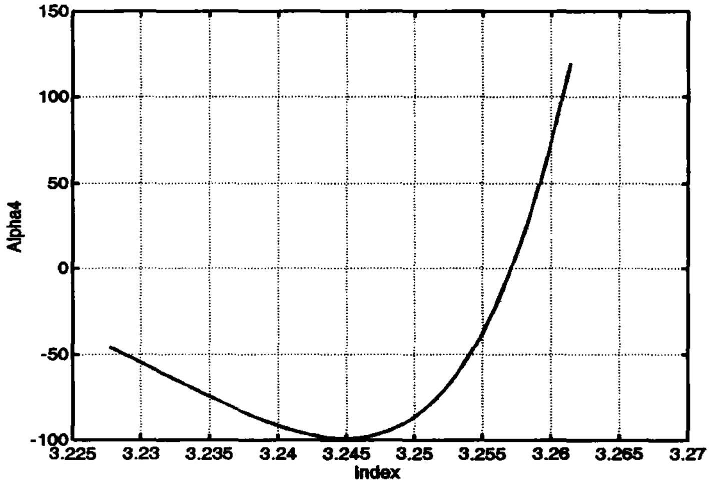

Figure 3.4 Plot of α_4 vs. index

The effective index of the ridge area for the structure shown in Table 3.1 is calculated to be $n_{eff}\_C = 3.2571$, and the effective index of the shoulder area is $n_{eff}\_S = 3.2343$. The electrical field for the ridge area and shoulder area are shown in Fig. 3.5 (a) and (b) respectively. Note that the electric field is evanescent at the substrate which shows that the layers are working as a waveguide.

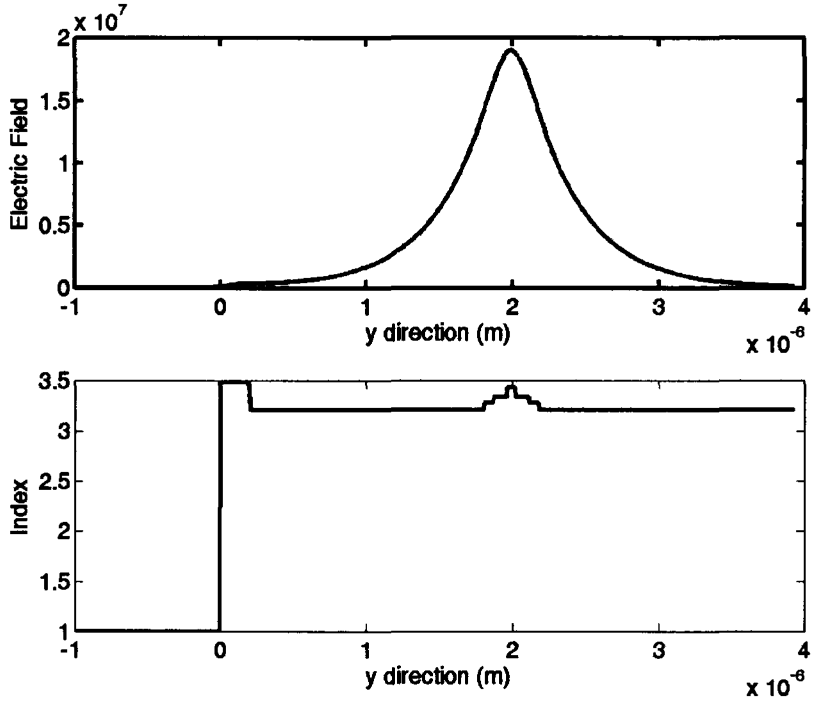

(a)

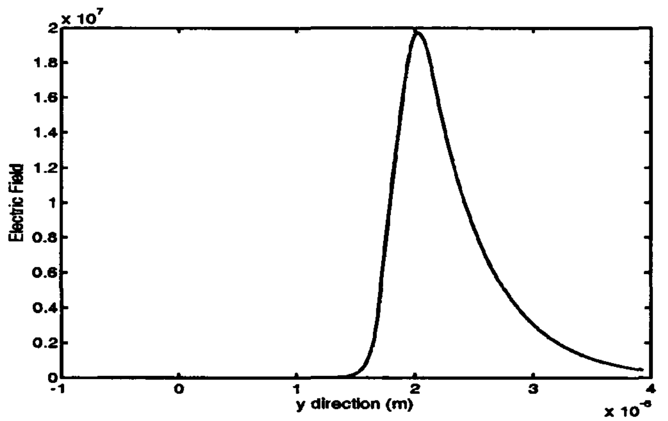

(b)

Figure 3.5 Electric field in the y direction (a) ridge area. (b) shoulder area

Next, the three-layer symmetric slab waveguide with indices of n_{eff}_S, n_{eff}_C, n_{eff}_S are solved. The thickness of the center layer is the ridge width w. In this step, one has to be aware that the E_x component is perpendicular to the slab boundaries; therefore, the guidance condition for the TM modes of the slab waveguide should be applied[50]. The eigenvalue equation is:

$$\alpha\frac{w}{2} = \frac{n_S^2}{n_C^2}(k_x\frac{w}{2})\tan(k_x\frac{w}{2}) \tag{3.9}$$

To solve k_x, the relation of k_x, β_z, and α is needed:

$$\begin{cases} k_x^2 + \beta_z^2 = k_0^2 n_C^2 \\ -\alpha^2 + \beta_z^2 = k_0^2 n_S^2 \end{cases}$$

By eliminating β_z, one obtains:

$$\alpha^2 + k_x^2 = k_0^2 (n_C^2 - n_S^2) \tag{3.10}$$

where k_x,, β_z, and α are derived from mode solutions of the form of the magnetic field:

$$H_y(x) = Ce^{i\beta_z z} \begin{cases} \cos(k_x \frac{w}{2}) e^{-\alpha(x-w/2)} & x \geq \frac{w}{2} \\ \cos(k_x x) & |x| \leq \frac{w}{2} \\ \cos(k_x \frac{w}{2}) e^{\alpha(x+w/2)} & x \leq -\frac{w}{2} \end{cases} \tag{3.11}$$

For the electric field, $\vec{E}_x(x) = \hat{x} \frac{1}{\omega\varepsilon_i}(\beta_z H_y)$, and the effective index of 2-D waveguide is $n_{eff} = \beta_z / k_0$. Figure 3.6 shows the electric field in the transverse direction for a ridge width of 1.5 µm. There are two discontinuous points in $E_x(y)$ because of the boundary condition for the TE mode in the transverse direction. The effective index for the 2D waveguide is 3.2479.

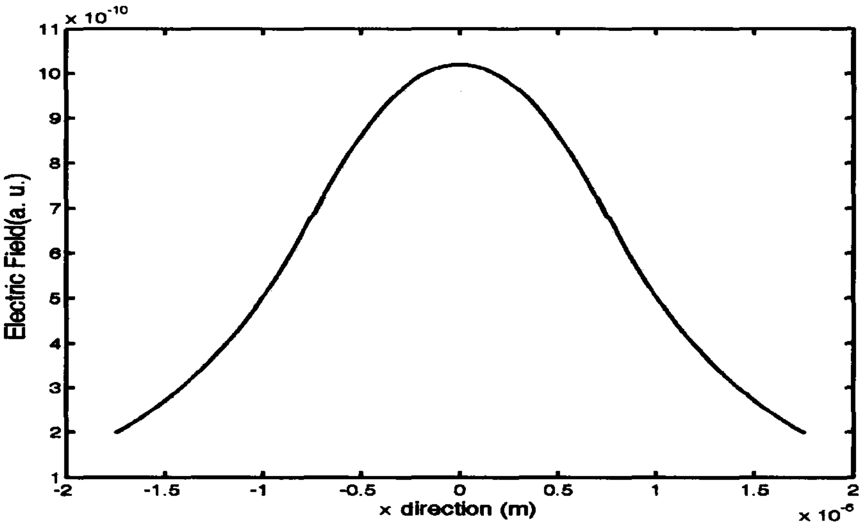

Figure 3.6 Electrical field in x direction

Once the optical field is calculated, the optical confinement factor is calculated with Eq. (3.3).

3.3 Optimization of the Confinement Factor

If the waveguide structure is designed properly, the peak of the optical field overlaps with the active region, which means that optical confinement factor is maximized in the ridge waveguide structure. To achieve the maximum optical confinement factor, it is necessary to optimize the thicknesses of various layers especially the ridge height, the thickness of the cladding layers and of the SCH layers. In this section I will introduce the work that targets the optimization of the confinement factor with a Marquardt least-square nonlinear fitting method.

The confinement factor can be taken as a nonlinear function of the layer thicknesses, i.e., $\Gamma(a_1, a_2, \ldots. a_n)$, as calculated in Section 3.2. a_1, $a_2, \ldots. a_n$ could be the thicknesses of the growth layers such as the ridge height, the thickness of the cladding layer, the SCH layers, and the outermost barriers. To find the maximum Γ, the goodness-of-fit parameter χ^2 was defined as $\chi^2 = 1 - \Gamma^2$. Thus my target is to find the minimum of χ^2 as a function of a_1, a_2, ... a_n.

A least-square method[53] is based on the theory of the *method of maximum likelihood* in fitting the analytical function (dependent variable y to be a function of independent variables x_i as $y(x_i)$) to the experimental measurements. The probability for the observed measurements to be the actual value is assumed to follow the Gaussian distribution with a standard deviation of σ. The maximum likelihood method maximizes the probability of the obtaining the measurements given the fitting parameters. Because a Gaussian function is the exponential of the negative of a sum of squares, maximizing the probability is equivalent to minimizing the sum in the exponential, which is called the goodness-of-fit parameter χ^2.

However, there is no true value in optimizing the confinement factor in my case. $\chi^2 = 1 - \Gamma^2$ is a numerical function of the layer thicknesses a_1, a_2, ... a_n. The target for the nonlinear fitting is to search the minimum of χ^2 in the parameter space a_1, a_2, ... a_n. A Marquardt nonlinear fitting method[53] is adopted for this work.

The optimization of the confinement factor for the SLD structure was started based on the known wafer structure #4177. I focused on the optimization of the thickness of the growth layers in the y direction. In theory, all of the 22 layers, including their growth thicknesses, could be set as independent variables. However, it was found in my calculations that the starting point of the nonlinear fitting is important because of the existence of local minima in the parameter space. Furthermore, it is not necessary to allow the thicknesses of all the layers to be independent variables. It was found from my experience that the ridge height, the thickness of the cladding layer underneath the etch stop, the SCH layers, and the two outermost barrier layers were the parameters that are most important. In the following calculation, I demonstrate the results of the optimization with the chosen parameter space.

The confinement factor for structure #4177 (which has one SCH layer on each side of the active region with thicknesses of 800 Å, as shown in Table 3.2) is calculated to be 6.42% with an n_{eff}_C = 3. 2422, n_{eff}_S = 3.2197, and $n_{\mathrm{eff}} = 3.2330$. Figure 3.7 shows the steps in a maximization of the confinement factor by choosing six variables as a_2 (ridge height), a_5 (cladding layer underneath the etch stop), a_6, a_{10} (SCH layers) and a_7, a_9 (the outermost barrier layers) as the fitting parameters. The final structure that gave Γ = 6.88% with n_{eff}_C = 3.2383, n_{eff}_S = 3.2189, and n_{eff} = 3.2298 is shown in Table 3.3. Compared with structure #4177, it was found that the ridge height was increased to 1.6 μm, the cladding layer a_5 was decreased to 0.118 μm, the SCH layer a_6, was decreased to 61 nm and a_{10} was increased to 147.6 nm . Through this calculation it was found that the layer thicknesses with small numbers such as the outermost barrier layers did not change much.

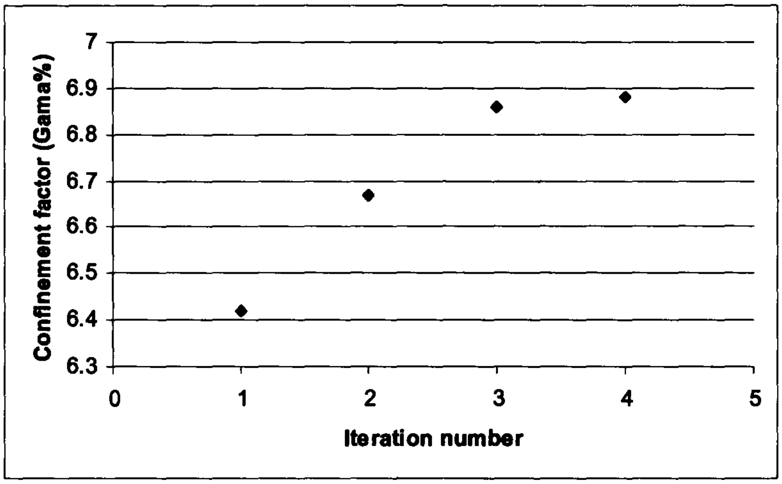

Figure 3.7 Improvement of confinement factor starting from #4177

Table 3.2 Structure of wafer #4177

Thickness	Composition
0.15 µm (a_1)	p-InGaAs contact layer
1.25 µm (a_2)	p-InP
0.15 µm (a_3)	p-InP
75 Å (a_4)	p-$In_{0.72}Ga_{0.28}As_{0.61}P_{0.39}$
0.15 µm (a_5)	p-InP
800 Å (a_6)	$In_{0.92}Ga_{0.08}As_{0.175}P_{0.825}$
300 Å (a_7)	$In_{0.828}Ga_{0.172}As_{0.316}P_{0.684}$
50 Å |	$In_{0.828}Ga_{0.172}As_{0.62}P_{0.38}$
75 Å |	$In_{0.828}Ga_{0.172}As_{0.316}P_{0.684}$
50 Å |	$In_{0.828}Ga_{0.172}As_{0.62}P_{0.38}$
75 Å |	$In_{0.828}Ga_{0.172}As_{0.316}P_{0.684}$
50 Å | (a_8)	$In_{0.828}Ga_{0.172}As_{0.62}P_{0.38}$
75 Å |	$In_{0.828}Ga_{0.172}As_{0.316}P_{0.684}$
50 Å |	$In_{0.828}Ga_{0.172}As_{0.62}P_{0.38}$
75 Å |	$In_{0.828}Ga_{0.172}As_{0.316}P_{0.684}$
50 Å |	$In_{0.828}Ga_{0.172}As_{0.54}P_{0.46}$
300 Å (a_9)	$In_{0.828}Ga_{0.172}As_{0.316}P_{0.684}$
800 Å (a_{10})	$In_{0.92}Ga_{0.08}As_{0.175}P_{0.825}$
0.6 µm (a_{11})	n-InP
n-InP substrate	

Table 3.3 Structure for nonlinear fitting result which started with #4177

Thickness	Composition
0.15 μm (a_1)	p-InGaAs contact layer
1.60 μm (a_2)	p-InP
0.15 μm (a_3)	p-InP
75 Å (a_4)	p-$In_{0.72}Ga_{0.28}As_{0.61}P_{0.39}$
0.118 μm (a_5)	p-InP
610 Å (a_6)	$In_{0.92}Ga_{0.08}As_{0.175}P_{0.825}$
300 Å (a_7)	$In_{0.828}Ga_{0.172}As_{0.316}P_{0.684}$
50 Å	$In_{0.828}Ga_{0.172}As_{0.62}P_{0.38}$
75 Å	$In_{0.828}Ga_{0.172}As_{0.316}P_{0.684}$
50 Å	$In_{0.828}Ga_{0.172}As_{0.62}P_{0.38}$
75 Å	$In_{0.828}Ga_{0.172}As_{0.316}P_{0.684}$
50 Å (a_8)	$In_{0.828}Ga_{0.172}As_{0.62}P_{0.38}$
75 Å	$In_{0.828}Ga_{0.172}As_{0.316}P_{0.684}$
50 Å	$In_{0.828}Ga_{0.172}As_{0.62}P_{0.38}$
75 Å	$In_{0.828}Ga_{0.172}As_{0.316}P_{0.684}$
50 Å	$In_{0.828}Ga_{0.172}As_{0.54}P_{0.46}$
300 Å (a_9)	$In_{0.828}Ga_{0.172}As_{0.316}P_{0.684}$
1476 Å (a_{10})	$In_{0.92}Ga_{0.08}As_{0.175}P_{0.825}$
0.6 μm (a_{11})	n-InP
n-InP substrate	

To step out of the local minimum that was obtained by the fit starting with the initial parameter associated with wafer #4177, another SCH layer was added as a new starting point. The compositions of the two SCH layers were chosen based on the principle of increasing the confinement factor. It was found by my calculation that, when the SCH layers close to the active region have high refractive indices, the confinement factor will be increased. Therefore, the inner SCH layers were chosen to have indices close to the indices of the outermost barrier layers. Table 3.4 shows the initial structure parameters. It was found that the confinement factor for this initial structure was 8.33% with n_{eff}_C = 3.2602, n_{eff}_S = 3.2464, and an effective index for the 2D waveguide structure for the fundamental TE mode of n_{eff}= 3.2531.

Table 3.4 Varied structure with two SCH layers as a starting point for the nonlinear fitting

Thickness	Composition
0.2 μm (a_1)	p-InGaAs contact layer
1.40 μm (a_2)	p-InP
0.1 μm (a_3)	p-InP
50 Å (a_4)	p-$In_{0.72}Ga_{0.28}As_{0.61}P_{0.39}$
0.15 μm (a_5)	p-InP
700 Å (a_6)	$In_{0.92}Ga_{0.08}As_{0.18}P_{0.82}$
700 Å (a_7)	$In_{0.86}Ga_{0.14}As_{0.31}P_{0.69}$
300 Å (a_8)	$In_{0.828}Ga_{0.172}As_{0.32}P_{0.68}$
50 Å |	$In_{0.828}Ga_{0.172}As_{0.62}P_{0.38}$
75 Å |	$In_{0.828}Ga_{0.172}As_{0.316}P_{0.684}$
50 Å |	$In_{0.828}Ga_{0.172}As_{0.62}P_{0.38}$
75 Å |	$In_{0.828}Ga_{0.172}As_{0.316}P_{0.684}$
50 Å | (a_9)	$In_{0.828}Ga_{0.172}As_{0.62}P_{0.38}$
75 Å |	$In_{0.828}Ga_{0.172}As_{0.316}P_{0.684}$
50 Å |	$In_{0.828}Ga_{0.172}As_{0.62}P_{0.38}$
75 Å |	$In_{0.828}Ga_{0.172}As_{0.316}P_{0.684}$
50 Å |	$In_{0.828}Ga_{0.172}As_{0.54}P_{0.46}$
300 Å (a_{10})	$In_{0.828}Ga_{0.172}As_{0.32}P_{0.68}$
700 Å (a_{11})	$In_{0.86}Ga_{0.14}As_{0.31}P_{0.69}$
700 Å (a_{12})	$In_{0.92}Ga_{0.08}As_{0.18}P_{0.82}$
0.75 μm (a_{13})	n-InP
n-InP substrate	

Starting with this structure and setting the parameter space as six variables (a_2, a_5, a_6, a_8, a_{10}, a_{12}), the confinement factor increased to 9.71% as shown in Fig. 3.8. It was found that the confinement factor converged to a stable number after 9 iterations. The final structure for this calculation is shown in Table 3.5. For the optimized structure, n_{eff}_C = 3.2571, n_{eff}_S = 3.2315, and the effective index of the 2D waveguide structure for the fundamental mode n_{eff} = 3.2474.

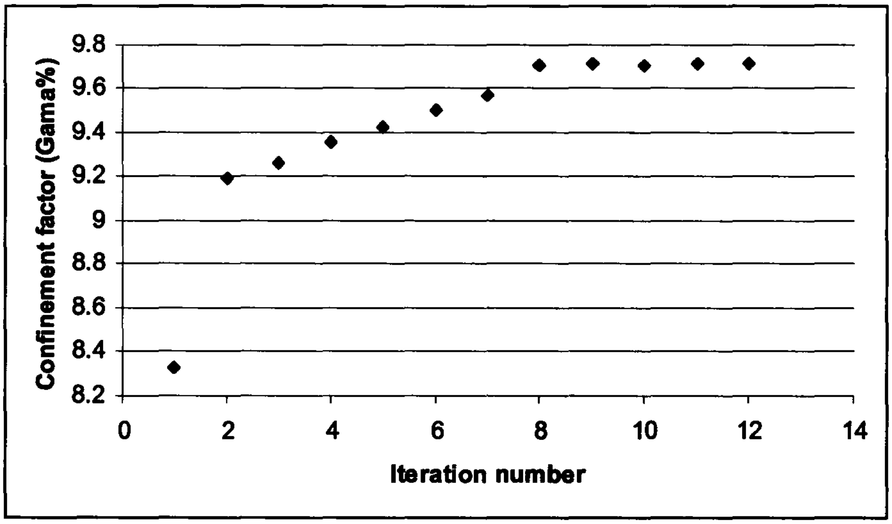

Figure 3.8 Improvement of confinement factor starting from table 3.4

Table 3.5 Optimized structure with two SCH layers

Thickness	Composition
0.2 μm (a_1)	p-InGaAs contact layer
1.36 μm (a_2)	p-InP
0.1 μm (a_3)	p-InP
50 Å (a_4)	p-$In_{0.72}Ga_{0.28}As_{0.61}P_{0.39}$
0.061 μm (a_5)	p-InP
699 Å (a_6)	$In_{0.92}Ga_{0.08}As_{0.18}P_{0.82}$
700 Å (a_7)	$In_{0.86}Ga_{0.14}As_{0.31}P_{0.69}$
199 Å (a_8)	$In_{0.828}Ga_{0.172}As_{0.32}P_{0.68}$
50 Å |	$In_{0.828}Ga_{0.172}As_{0.62}P_{0.38}$
75 Å |	$In_{0.828}Ga_{0.172}As_{0.316}P_{0.684}$
50 Å |	$In_{0.828}Ga_{0.172}As_{0.62}P_{0.38}$
75 Å |	$In_{0.828}Ga_{0.172}As_{0.316}P_{0.684}$
50 Å | (a_9)	$In_{0.828}Ga_{0.172}As_{0.62}P_{0.38}$
75 Å |	$In_{0.828}Ga_{0.172}As_{0.316}P_{0.684}$
50 Å |	$In_{0.828}Ga_{0.172}As_{0.62}P_{0.38}$
75 Å |	$In_{0.828}Ga_{0.172}As_{0.316}P_{0.684}$
50 Å |	$In_{0.828}Ga_{0.172}As_{0.54}P_{0.46}$
199 Å (a_{10})	$In_{0.828}Ga_{0.172}As_{0.32}P_{0.68}$
700 Å (a_{11})	$In_{0.86}Ga_{0.14}As_{0.31}P_{0.69}$
699 Å (a_{12})	$In_{0.92}Ga_{0.08}As_{0.18}P_{0.82}$
0.75 μm (a_{13})	n-InP
n-InP substrate	

Compared with structure #4177, the confinement factor increased about 51.4%. The finalized growth sheet is shown in Appendix A as structure M0446. The cladding layer underneath the etch stop was set to be 0.08 μm compared with 0.061 μm in Table 3.5 in order to guarantee the confinement of the optical field in the active region. The confinement factor for the final growth structure of M0446 is calculated to be 9.19%. Thus the confinement factor of M0446 increased 43.2% compared with wafer #4177.

Three wafers of structure #M0446 were grown at the same time with MOCVD by CPFC. Wafer one was used for measurement of the wavelength of the photo-luminescent (PL) peak. Wafer two was processed at the CPFC using a double section mask, which was designed by the author and is shown in Appendix B. The third wafer was processed by the author in the CEDT cleanroom at McMaster University. PL measurement has two peaks from QWs with two different transition energies: one has a peak at 1324 nm, the other has a peak 1246 nm. It shows the CPFC growth is a success (see Fig. 3.9).

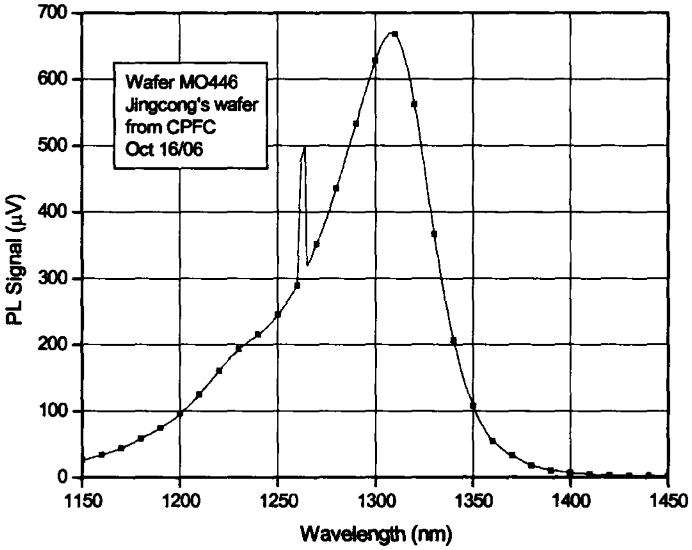

Figure 3.9 PL peak of wafer M 0446

The four-layer mask, which is shown in Appendix B, was designed with ridge widths of 3, 4, 5 and 6 μm. It was shown by near field measurements (see Appendix C) that all of the 1.3 μm SLD are single transverse mode. The mask was designed for a double section ridge-waveguide structure, which is shown schematically in Fig. 3.10. The back section and front section are separated by etching the InGaAs contact layer. Measurements of the power and the spectra will be shown in the next chapter after introduction of the active region design. The spectral measurements show that the double section waveguide structure improves both the power output and the spectral width of an

SLD.

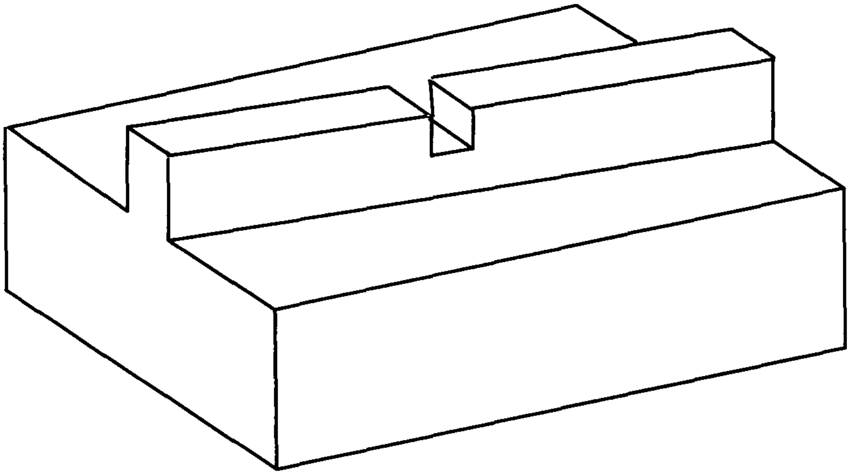

Figure 3.10 Schematic of double-Section Angled-Stripe Structure

To check the effect of optimization of the confinement factor, two devices with the same parameters (both are double section, with front section 750 μm long, back section 400 μm long, and 4 μm ridge width) were cleaved from wafer #M0446 and wafer #4177 and were measured under the same condition. The spectra are shown in Fig. 3.11(a) and (b). The pump current for the back section was 7 mA and the front section driving current was 220 mA. The power was measured under free space with a large area InGaAs detector. It was found that the power for an SLD cleaved from M0446 increased about 95 % (1.04 mW for M0446 and 0.533 mW for 4177) compared with the SLD cleaved from #4177.

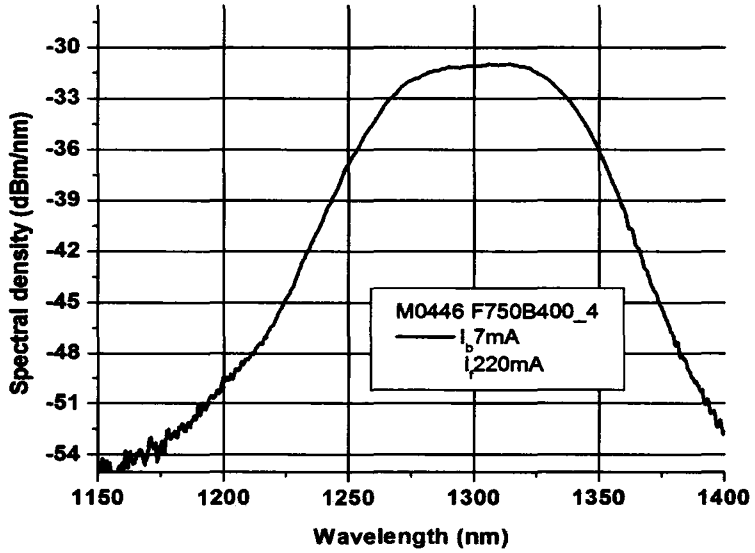

(a)

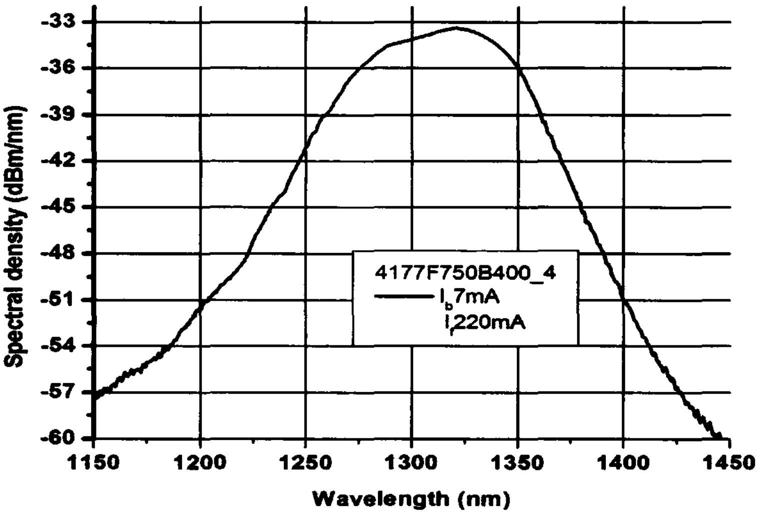

(b)

Figure 3.11 spectrum of double section SLD cleaved from M0446 with power of 1.04mW; FWHM: 75nm. (b)spectrum of double section SLD cleaved from wafer #4177 with power of 0.533mW;FWHM: 75nm.

3.4 Conclusion

Optimization of the SLD waveguide, which targets the maximization of the optical confinement factor, was introduced in this chapter. An effective index method was applied to solve the rectangular waveguide structure. A planar waveguide with arbitrary layers was solved with a transfer matrix method. When the optical field was known, the optimization of the confinement factor was performed by a Marquardt least-square nonlinear fitting method. The confinement factor was increased from 6.4% to 9.2% for the final growth structure. Measurement of SLD output power of devices that were cleaved from the wafer with the old waveguide and with the optimized waveguide showed that the power increased 95%.

Besides the waveguide structure design, another important concern for a high power, broad spectral width SLD is the design of the active region. From the gain calculation of asymmetric multiple quantum well (AMQW) devices, it was found that a broad spectral width is obtained only when transitions from short-wavelength wells and from long-wavelength wells contribute nearly equally to the gain spectrum. This part of my research will be presented in Chapter 4.

4 Active Region Design Considerations for AMQW Broad Spectral Width SLDs and Measurements of SLDs

4.1 Introduction

In this chapter, I describe my work on the design of the active region of asymmetric multiple-quantum-well (AMQW) broad spectral width superluminescent diodes (SLDs) centered at 1.3 μm. Compared with an LED, an edge emitting SLD takes advantage of confinement by an optical waveguide to enhance amplification of the spontaneous emission. However, the facet reflectivities on an edge-emitting SLD have to be minimized to suppress the feedback and the attendant spectral modulation. AR coating of one facet,[54] integrated absorber, angled stripe[55] or a combination of these methods were published in previous research. These works were mainly focused on SLDs with symmetric multiple quantum wells.[27] Some publications, such as those by Yamatoya *et al*[26] and the group of C. F. Lin,[28] used asymmetric multi-quantum wells (AMQW) for SLDs but these papers only reported experimental results. Until now, there has been no theoretical direction for the design of the AMQW active region for a broad spectral width SLD.

The design of the active region for AMQW SLDs in my work is based on simulations of the gain and the emission spectra of AMQW SLDs, and on comparisons with experimental data of two SLD structures: Structure 1 (wafer # 3979) and Structure 2 (wafer #M0446). Structure 1 was a first attempt, based on intuition and experience with AMQW lasers, at the design and fabrication of a broad spectral width SLD. However, measurements showed that devices of this first design would operate with a broad spectral width only at low current. Thus low output power could only be achieved. Structure 2 was then designed based on simulations and taking into account our understanding and results from measurements on devices based on structure 1. The AMQW gain simulations show that there exists a critical carrier density at which the peak gains of the red and blue wells are approximately equal and at this point, the total gain curve is broad and relatively flat. We call this carrier density the transition carrier density (TCD). It was found that the transition carrier density (TCD) for structure 1 was much lower than that of structure 2. It is shown that the simulation, which is based on gain calculations with a Galerkin method, can predict the TCD for different active region designs.

A seven degree tilted-stripe ridge waveguide structure was adopted to reduce the reflectance from the cleaved facet for the SLDs. No AR coatings were applied to the facets. In addition to single section SLDs, double-section devices were processed by etching through the contact layer. An un-pumped back section works as an absorbing volume to reduce further the reflectance of the back facet. However, if one pumps the back section of AMQW SLDs with a couple of milliamperes, the operation of the devices will be enhanced by a broadening of the SLD spectrum at the red side. When the back section is pumped, the short wavelength light that is emitted will be absorbed by the front section; the long wavelength light (i.e., the red light), however, will penetrate through the front section (assuming that the front section is pumped hard and the bands are filled) because the front section is transparent for the long wavelengths. It will be shown that the output power is also increased by pumping both sections.

4.2 AMQW SLD active region design consideration

It was found in our previous research in broadly tunable AMQW InGaAsP/InP lasers[22, 23] that there exits one critical cavity length called the transition cavity length (TCL) and that this TCL plays a crucial role in obtaining broadly tunable operation at a set injection current. The TCL was defined as the cavity length below which a cleaved AMQW laser operates at short-wavelengths at threshold and above which the laser operates at long-wavelengths at threshold. If the laser is cleaved slightly longer than the TCL, the laser can be tuned in a short external cavity over transitions from the short wavelength (blue) wells and from the long wavelength (red) wells of the AMQW active region without changing the injected current. This characteristic makes the AMQW device broadly tunable laser and especially suitable for application to Fourier domain OCT and to synthesized OCT as shown in Chapter 2.[19]

The physics behind the idea of the TCL is the dependence of the gain of an AMQW laser on the carrier density as shown in Fig. 4.1. Because the quasi-Fermi level of the red well is lower than that of a blue well, the red well reaches transparency at a lower carrier density than a blue well. As the carrier density increases, blue wells reach transparency and contribute to the gain. At a particular carrier density, the peak gains of the red and blue wells are approximately equal and the total gain curve is broad and relatively flat. We call this carrier density the transition carrier density (TCD). At higher carrier densities, the gain at short wavelengths is greater than the gain at long wavelengths since the short wavelengths experience gain from both the red and the blue wells.

The TCD plays a similar role in the design of broad spectral width AMQW SLDs. The spectral output of an AMQW SLD with two transition energies is dominated by the low energy transitions for low carrier densities and by the high energy transitions for high carrier densities. In both cases the spectral output is similar in width to that of a symmetric multiple-quantum well SLD (with one transition energy). Only when the device operates near the TCD do transitions from the red and the blue wells contribute nearly equally to produce a broad spectral output. For tunable AMQW lasers the operating carrier density is determined by the threshold condition. However there is no threshold condition for AMQW SLDs; the operating carrier density is restricted only by the operating current density. For an AMQW SLD with two transitions of different energies, there exists a specific current density at which the two transitions contribute equally to the spectral output.

Note that the carrier density that I am referring to is the carrier density in the quantum wells. For InGaAsP/InP AMQW devices, it was shown[22] that the carrier density in the quantum wells decreases from the p-side to the n-side because of the low mobility of the holes caused by the large heterobarriers in the valence bands. Therefore, I refer to the carrier density for the quantum well nearest the p-side. An exponential decay of the carrier density from the p-side QWs to the n-side QWs is assumed. This assumption was found[22] to be consistent with the measured performance of AMQW lasers. The nonuniform carrier density is also the reason why the sequence of the quantum well is important for a specific design of an AMQW laser or an AMQW SLD.

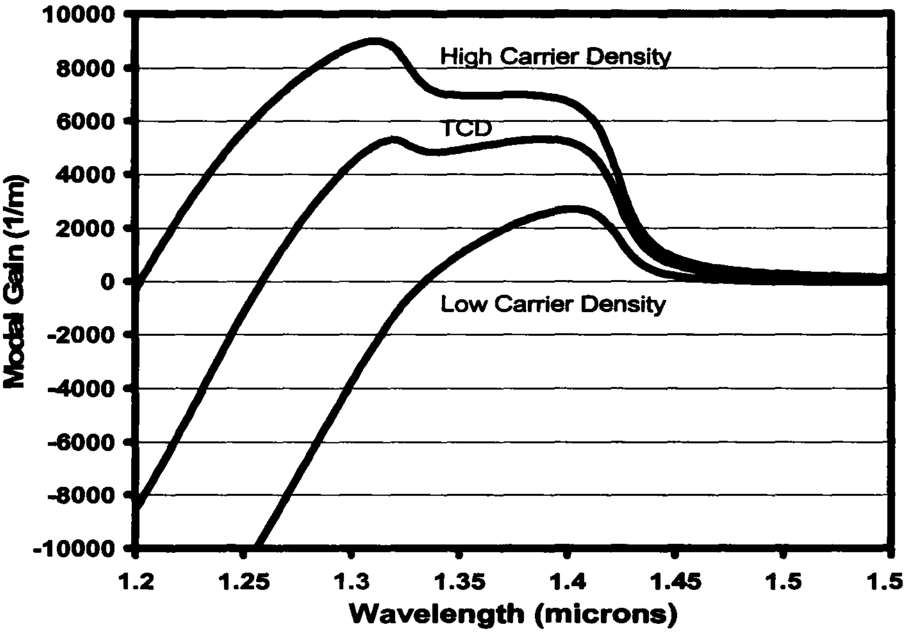

Figure 4.1 Depiction of the transition carrier density concept

The carrier density in the quantum wells is a dynamic parameter. There exists dynamic equilibrium between pumping rate, carrier density, and the radiation density. This equilibrium is usually described by a rate equation.[56] One can get a specific carrier density under steady state conditions. When the device is running under steady state, the carrier density in the quantum wells is a function of the injection current. Once the dimensions of the quantum well are fixed, the terms 'transition carrier density' and 'transition current' can be used interchangeably since the two are related by a rate equation as shown in the next section.

It is shown in the next section that the TCD has to be relatively high to achieve a reasonably high output power. However the TCD should not be too high and unattainable owing to thermal effects or current supply limitations.

4.3 *Model Descriptions*

The AMQW SLD design software[65,67] includes three parts: a gain and spontaneous emission calculator for a given carrier density; an SLD emission spectrum calculator for a given gain spectrum; and a carrier density calculator for given applied current. These three calculators are coupled with each other. Newton's method is applied in the emission spectrum calculator to find iteratively the solution at steady state for an SLD by starting with an initial guess for the carrier density as $10^{22}\,\mathrm{m}^{-3}$ in the quantum well at the p-side. The gain calculator starts with a calculation of the band structure. A 6-band Galerkin method is applied to calculate the band structure and QW transition energies.[24] The Galerkin approach is a powerful tool for calculating band structure as it is both accurate and computationally efficient. Gain and spontaneous emission spectra are then calculated for each QW using the method described by Chuang.[57] In addition to the QW transition energies, the gain and spontaneous emission calculator requires a carrier density to be specified for each QW. An exponential decay with a decay distance x_0 of 30 nm was assumed for the distribution of carriers over the quantum wells from the p-side to the n-side with the total thickness of the active region of 70 nm: $N(x) = N_0 e^{-x/x_0}$. N_0 is the carrier density in the quantum well at the p-side which will be obtained by the carrier density calculator. The individual QW gain and spontaneous emission curves are summed to produce the total gain and spontaneous emission spectra. Then the spectral output calculator (see Eq. (4.1)) takes the gain, spontaneous emission spectra and the physical parameters describing the SLD cavity as inputs. The output spectrum is then calculated using a probability amplitude transfer matrix method described by Morrison *et al*[58] as:

$$I_r = \left| \frac{t_r e^{-jk_0 nL}}{1 - r_r r_l e^{-j2k_0 nL}} \right|^2 \times \frac{1}{2} \left[\begin{array}{l} \dfrac{1 - e^{-2gL}}{g} + \dfrac{|r_l|^2 \, (e^{2gL} - 1)}{g} \\ + \dfrac{2}{k_0 n_R} \left(\Im m(r_l) + \Re e(r_l) \sin(2k_0 n_R L) - \Im m(r_l) \cos(2k_0 n_R L) \right) \end{array} \right] \tag{4.1}$$

The above equation for I_r is calculated by treating the SLD as an amplifier of spontaneous emission. I_r is the total light intensity output at the right facet. $n = n_R + in_I$ is the complex effective index of the SLD waveguide. g is the modal gain which is defined as $k_0 n_I$. L is the cavity length. r_r and r_l are the complex amplitude reflectivity of the facets at the right and left sides. $\Im m(\,)$ and $\Re e(\,)$ are the imaginary and real parts of a complex number. The SLD cavity was modeled as a Fabry-Pérot cavity with estimated front and back facet reflectance of 0.5%. The ridge width was set to 4 μm for all calculations and the cavity length was varied. The third term in the bracket is the cross correlation term which takes into account the interference between the emitted light traveling in two opposite directions[12].

The combination of the Galerkin band structure and QW energy level solver, the gain and spontaneous emission calculator, and the spectral emission calculator permits the output spectra of an AMQW SLD to be calculated given the active region parameters, the cavity parameters, and the carrier densities in the QWs. The final piece of the model is to solve for the carrier densities in the QWs for a given applied current. To do so, we set up a carrier density calculator using a rate equation for each QW as follows:

$$\frac{I_w \eta_w}{V_w e} = \frac{N_w}{\tau_{nr}} + CN_w^3 + \int S_w(\lambda)d\lambda + \sum_{allwells} \int B_w(\lambda)(G_w(\lambda)-1)(1+R(\lambda)G_w(\lambda))d\lambda \qquad (4.2)$$

where w denotes the w^{th} QW, I_w is the current injected into the w^{th} well, η_w is the current efficiency of the w^{th} well, which was set to 0.2 for all wells, V_w is the volume of the w^{th} well, and N_w is the carrier density for the w^{th} well. The N_w/τ_{nr} and CN_w^3 terms account for non-radiative and Auger recombination respectively. The non-radiative recombination lifetime, τ_{nr}, was set to 5 ns and C was set to 3×10^{-41} $m^6 \cdot s^{-1}$. $S_w(\lambda)$ is the total spontaneous emission rate per unit volume for the w^{th} QW into 4π steradians. The fourth term in Eq. (4.2) is the amplified spontaneous emission where $B_w(\lambda)=\beta S_w(\lambda)/g_w(\lambda)$. $g_w(\lambda)$ is the gain coefficient generated by the w^{th} QW and $G_w(\lambda)$ is the single pass gain generated by the w^{th} QW. β is the spontaneous emission factor which gives the fraction of spontaneous photons contributing to the mode. The QW rate equation, Eq. (4.2), is coupled through the photon population and the carrier density in the QW with the gain calculator and the output spectrum calculator Eq. (4.1). Equation (4.2) is solved iteratively using Newton's method to converge to the final solution for the carrier density.

Figure 4.2 shows two active region designs of AMQW 1.3 μm SLDs and illustrates the design ideology of the TCD approach. Appendix A shows the growth sheet of wafer #3979 and wafer #M0446. Both active regions are composed of five 50Å QWs separated by 75Å barriers. In each active region the compositions of the QWs vary to create the asymmetry. For both wafers, the barrier compositions are $In_{0.83}Ga_{0.17}As_{0.32}P_{0.68}$ which induces 0.2% tensile strain. The indium to gallium ratio is also kept constant at $In_{0.83}Ga_{0.17}$ in the QWs for both structures. For structure 1 (wafer# 3979) the arsenic to phosphorous ratio is $As_{0.60}P_{0.40}$ for the p-side well and decreases moving to the n-side of the active region as follows: $As_{0.59}P_{0.41}$, $As_{0.55}P_{0.45}$, $As_{0.53}P_{0.47}$, and $As_{0.525}P_{0.475}$ for the n-side well. For structure 2 (wafer# M0446) the arsenic to phosphorous ratio of the n-side well is $As_{0.54}P_{0.46}$ and the ratio for the other four wells is $As_{0.62}P_{0.38}$.

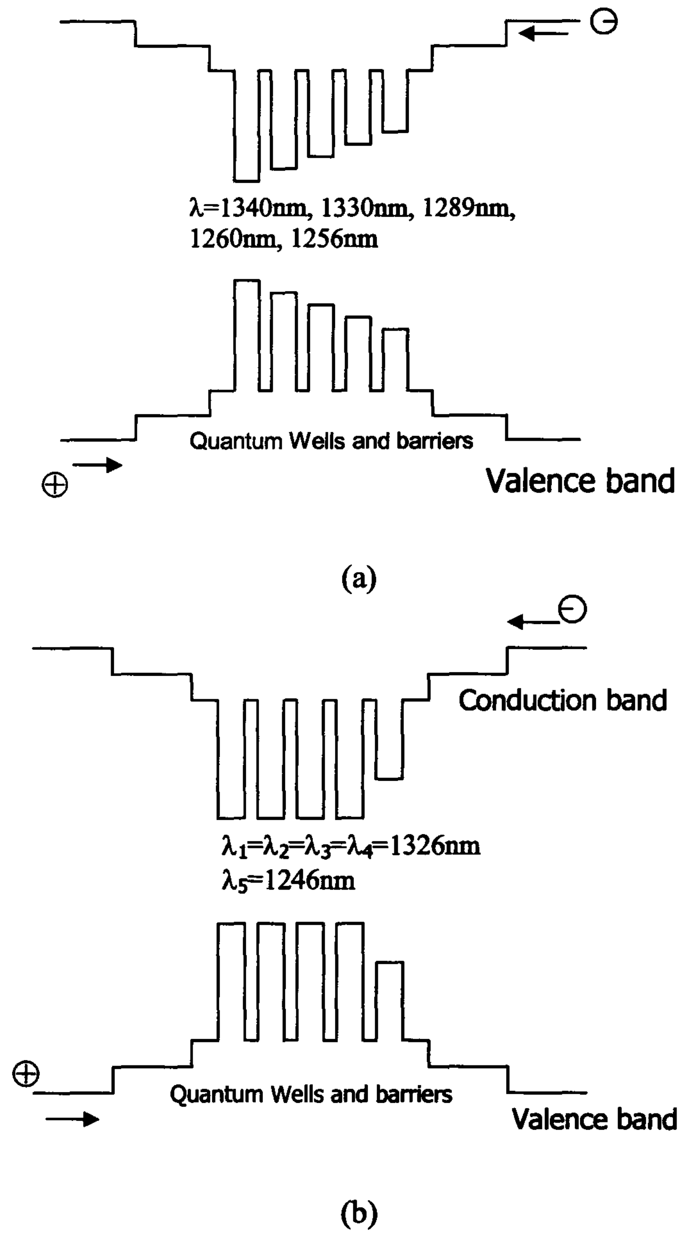

Figure 4.2 AMQW active regions of Structure 1 (a) and Structure 2 (b)

Figure 4.3 and Fig. 4.4 are the modal gain spectra for structure 1 and 2 under three different carrier densities. The solid curve in each plot is at the transition carrier density. The TCD is 4.4×10^{18} cm^{-3} for structure 1. Structure 1 was designed, based on experience with AMQW lasers, by placing 5 QWs with increasing transition energies from the p-side to the n-side. The structure was grown by gas-source, molecular beam epitaxy (MBE), and processed in the cleanroom at McMaster University. Measurements indicated that the SLD of structure 1 reached the TCD at a low current of 50 mA for a device with a

450 μm cavity length and a 4 μm ridge width, and only a low power of 50 μW could be achieved. Based on the experiences with Structure 1, the active region for Structure 2 was designed. Basically we wanted the short-wavelength well to contribute to the gain at high carrier densities only. This can be accomplished by four red wells and one blue well at the n-side. As a result, the TCD for Structure 2 is 8.3×10^{18} cm^{-3}. This was determined by running the gain calculator while adjusting the compositions of the red wells and the blue well to set the center of the gain curve at 1300 nm.

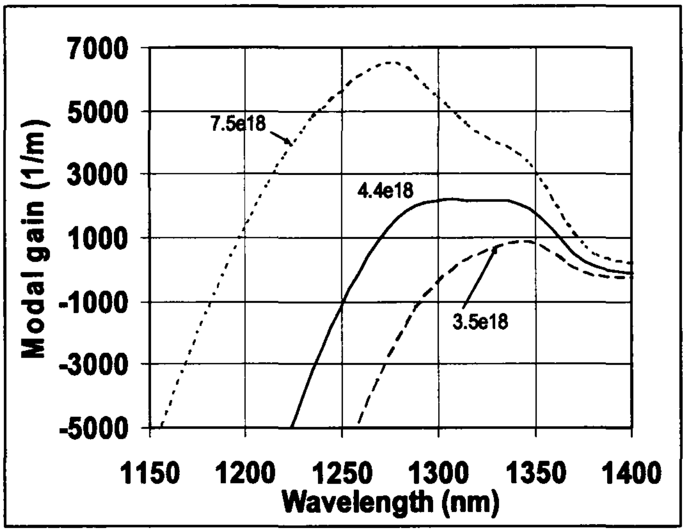

Figure 4.3 Calculated gain spectra for Structure 1 (wafer# 3979) at three carrier densities

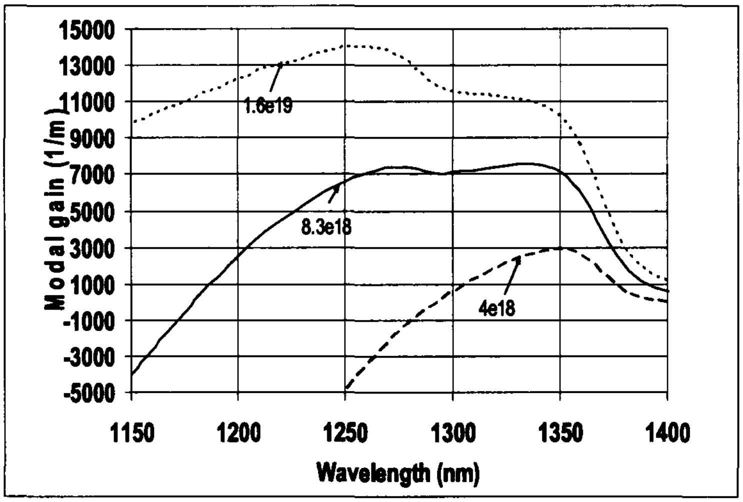

Figure 4.4 Calculated gain spectra for Structure 2 (wafer# M0446) at three carrier densities

Once the cavity parameters of the SLD are fixed, the TCD could be observed from the spectral measurements. There exists an injection current, which could be observed from the output spectrum, with equal contributions from both the red and the blue wells. We call this current the transition current. The carrier density in the QWs is not a parameter that could be measured directly, while the injected current is. For this reason, Fig. 4.5 shows from the carrier density calculator a plot of the carrier density in the p-side QW versus the injection current for Structure 2. For the data shown in Fig. 4.5 the cavity length and ridge width were set to be 250 μm and 4 μm.

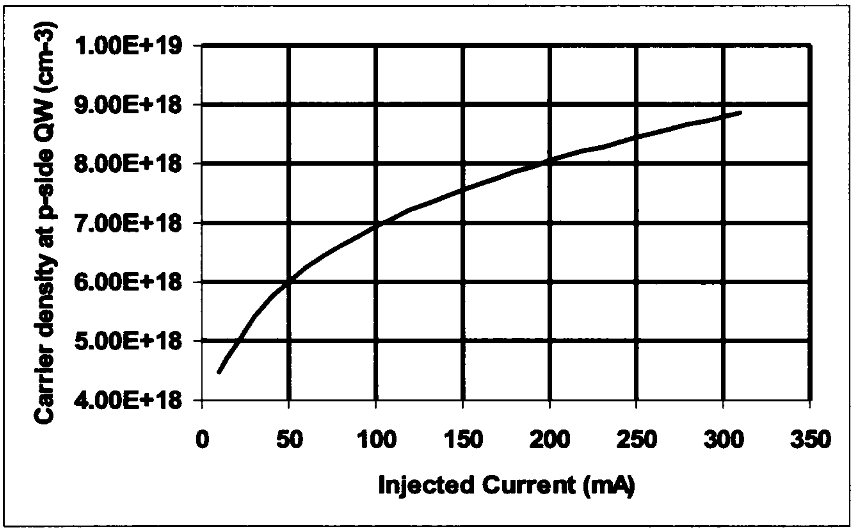

Figure 4.5 Simulated carrier density verse injected current in QW at the p-side for Structure 2

The simulated output spectra for three injected currents are shown in Fig. 4.6 and Fig. 4.7 for Structures 1 and 2 respectively. The ridge width was set to be 4 μm for the calculations. The transition current is 65 mA for Structure 1 with a spectral width of 85 nm, and it is around 200 mA for Structure 2 with a spectral width of around 100 nm.

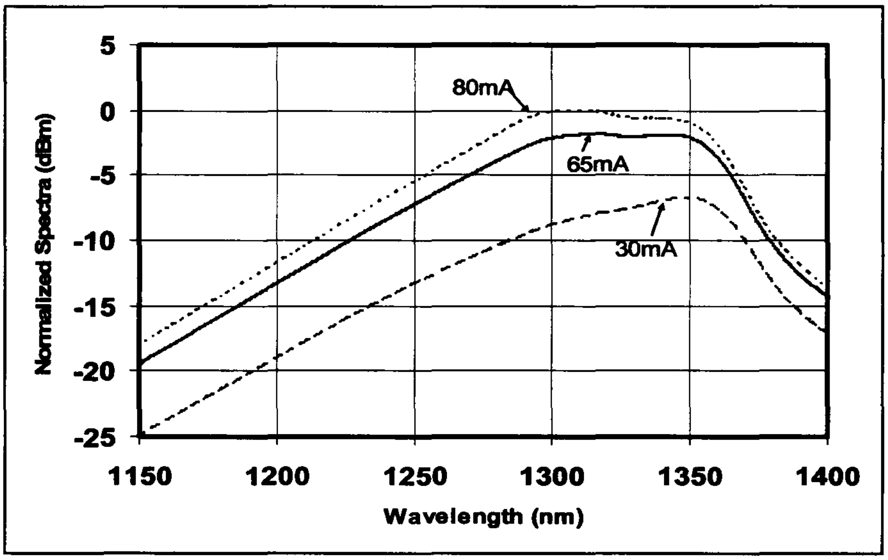

Figure 4.6 Model spectra for Structure 1 with cavity length of 450 μm

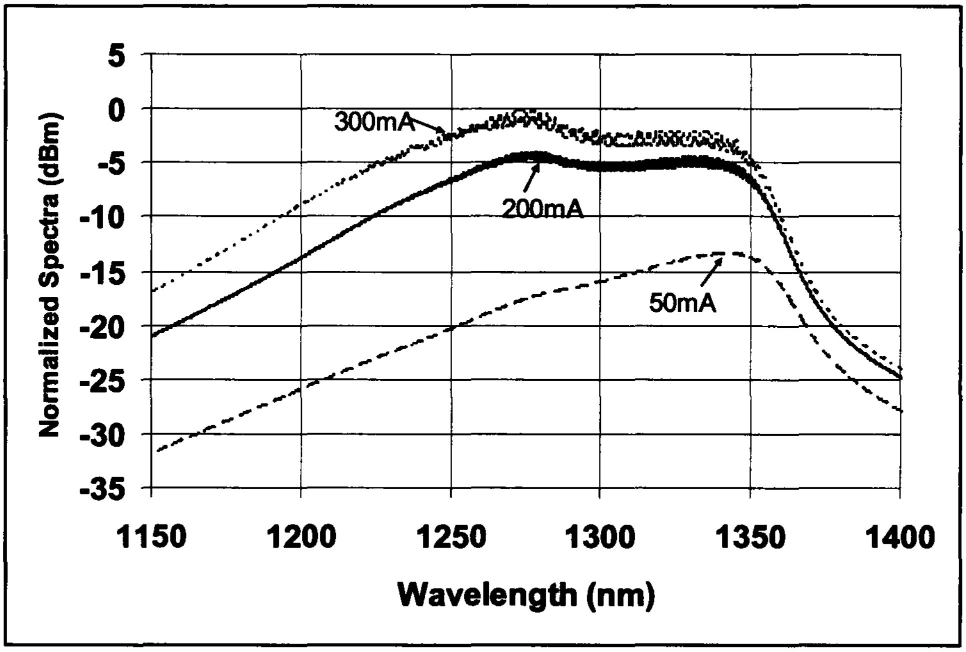

Figure 4.7 Model spectra for Structure 2 with cavity length of 250 μm

For a given AMQW SLD active region design, the TCD is fixed. However, the transition current depends on the cavity length and the ridge width of the SLD. For a longer cavity length device, the transition current will be higher because the volume of the active region is larger (see LHS of Eq. (4.2)). This is verified in both the spectral simulation and the experimental measurements. However, there exists an upper limit for the cavity length. Because a long cavity length will provide more gain for the device, it will cause the SLD to lase. Therefore, it is necessary to find the maximum cavity length at which we could obtain large gain without lasing and could reach the transition current before the thermal roll-off. The lasing threshold is determined by the facet reflectivity. So for lower facet reflectivity, the maximum cavity length will be longer, and vice versa. This effect is shown in the next section for structure 2 for a two section device with the back section working as an absorber to reduce further the facet reflectance.

4.4 Experimental Results

Structures 1 (wafer# 3979) and 2 (wafer# M0446) were processed as seven degree tilted stripe ridge waveguides to minimize the reflectance from the cleaved facet. A seven degree inclined angle of the stripe waveguide could theoretically reduce the facet reflectivity to be $< 10^{-6}$.[59] For Structure 1 the gain curve is predicted to be 85 nm wide, as shown in Fig. 4.3, which is approximately double that of a conventional symmetric quantum well device. The broadened gain leads the designer to believe that an SLD produced from this material will be broadly emitting. Measured spectra are shown for Structure 1 with a ridge width of 4 μm and a cavity length of 450 μm in Fig. 4.8. The transition current of this device is found to be 50 mA. It is a bit lower than the calculated result (this was also found in structure 2), likely due to underestimated parameters in the simulation such as the cavity loss and facet reflectivity. Below and above 50 mA the spectrum is narrow and is dominated either by the low energy transitions or the high energy transitions. It is only near 50 mA, which corresponds to the transition carrier density, that the spectrum is substantially broadened beyond that of a conventional device. The FWHM of the spectral output at the TCD is about 90 nm. However at 50 mA the output power of Structure 1 devices were approximately 50 μW, which is too low to meet OCT system requirements. To attain higher output power in combination with a broad spectral output, the transition carrier density must be increased. Structure 2 was designed based on this experience.

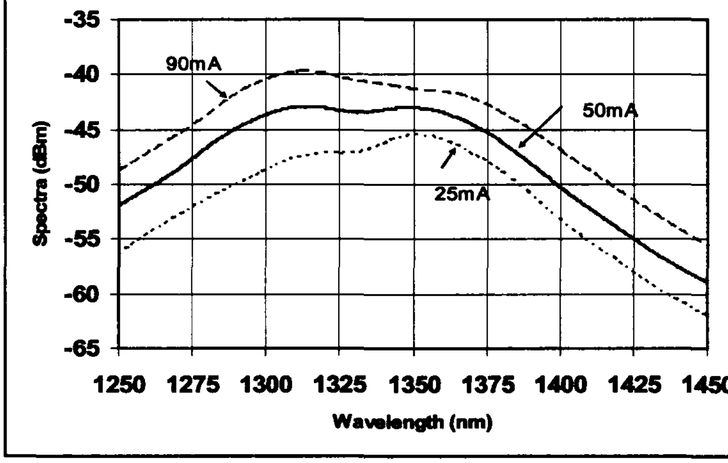

Figure 4.8 Measured Spectra for Structure 1 with 450 μm cavity length

The active region design in Structure 2 increased the TCD by adjusting the blue well to be able to reach the TCD only at very high carrier densities. Figure 4.9 is the measured output spectra for a 450 μm cavity length device with a 4 μm ridge width. The transition current is around 160 mA for this device. The transition from the red wells to the blue well can be observed. Above the transition current, the power will continuously increase but the blue well starts to dominate. The spectral width at 160 mA of structure 2 is about 100 nm centered at 1300 nm as expected from the simulation. The power at this cavity length is about 0.7 mW.

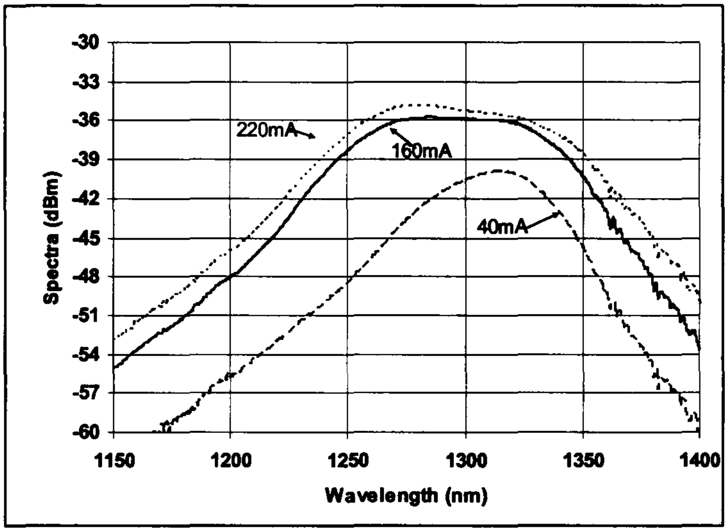

Figure 4.9 Measured output spectra for Structure 2 with 400μm cavity length

The transition current will be higher for longer cavity-length SLDs. The transition current reaches $I_t \approx 200$ mA for a 600 μm cavity length. If the ridge width increases from 4 μm to 6 μm, the transition current increases 5 mA to 10 mA. Since a long device will provide more gain for the light, the devices with cavity lengths over 600 μm will lase even before the transition current is reached. Thus the SLD has to be shorter than 600 μm. The total power for a 600 μm SLD is about 1 mW.

To improve the power of the SLD, Structure 2 was processed as a double section ridge-waveguide structure, which is shown schematically in Fig. 3.11. The back section and front section are separated by etching the InGaAs contact layer and thus the metal contact is separated also. The thickness of the SCH layers, the cladding layers, and the ridge height were designed to optimize the confinement factor as introduced in Chapter 3. This is essential for both diode lasers and SLDs. Only when the light is well confined in the active region can the efficiency of stimulated emission be increased. A transfer matrix method [60] was used to solve for the modes of the two dimensional waveguide and a Marquardt nonlinear fitting [61] method was applied to maximize the confinement factor.

With this double section structure, by pumping the front section only, the back section will work as an absorber and further reduce the reflectivity of the back facet. In this case, the maximum cavity length of the front section could be as long as 750 μm. At this cavity length, the transition current is around 260 mA. Figure 4.10 is the continuous wave (CW) light versus current (LI) curve for the 700 μm-long front section, 400 μm-long back section device by pumping the front section only. The highest power for this device is 1.8 mW. There is a power roll-off for currents higher than 300 mA because of thermal effects.

In Fig. 4.10, the power is higher at a current of 280 mA than at the TCD, but the short wavelengths dominate. By pumping the back section to I_b = 7.2 mA, the red side of the spectrum is lifted up to achieve a flat spectrum at high output power. Figure 4.11 shows the effect of a double section SLD. The dotted line is the spectrum when pumping the back section only (I_f = 0 mA). The red light penetrates the front section but the transitions from the blue well are absorbed by the unpumped front section. The dashed line shows the spectrum when pumping the front section only (I_b = 0 mA). When both sections are pumped, the red side of the spectrum is lifted up and the spectrum is broadened 10 nm as indicated by the solid line. The spectral width is over 90 nm with a flat top. The output power is also increased. The highest power attained by pumping both sections is 2 mW for a 4 μm ridge width. Figure 4.12 shows the ripples on the spectrum of the double section (front section 600 μm / back section 400 μm) device by pumping the front section only. It is as low as 0.1 dB when the back section is working as an absorber. The ripple is 0.3 dB if both sections are pumped and is a little higher because light gets reflected from the cleaved facet of the back section.

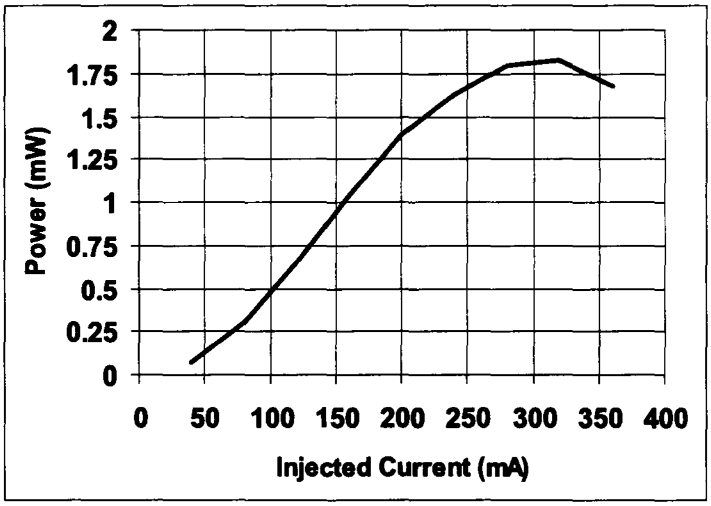

Figure 4.10 LI curve of Structure 2 F700/B400 μm SLD pumping front section

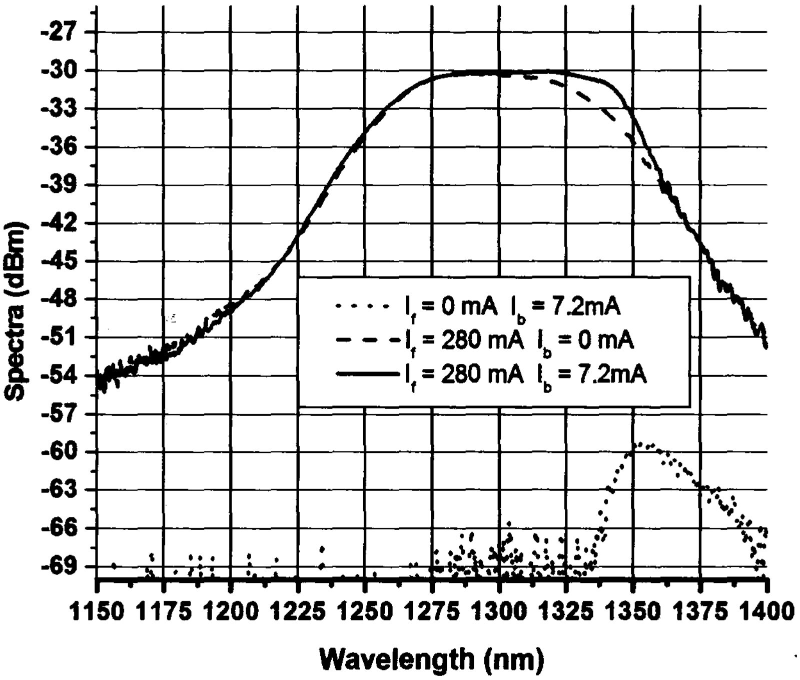

Figure 4.11 Effect of double section SLD (F750μm /B400μm) of Structure 2

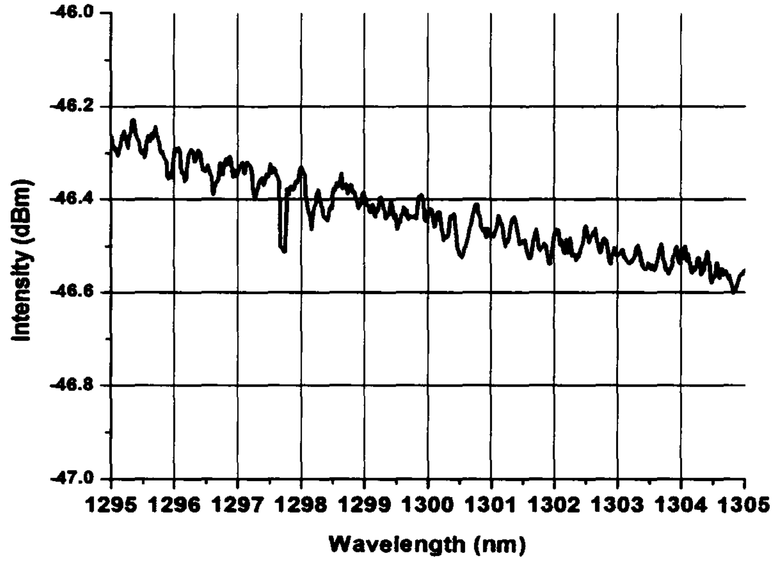

Figure 4.12 Ripple of F750μm /B400μm of Structure 2 by pumping the front section only

4.5 Conclusion

Based on calculations of gain for asymmetric multiple quantum wells and experience, it was discovered that the key design parameter for a broad spectral width SLD is the transition carrier density (TCD). It was shown that high power and broad spectral width is achieved in SLDs only when the transition carrier density is relatively high. At the TCD, broad spectral width SLDs of over 90 nm centered at 1.3 μm were achieved. A double section structure helps to broaden and flatten the SLD spectrum. SLDs centered at 1.3 μm were designed and processed; these 1.3 μm SLDs have application for OCT in ophthalmology. The depth resolution as determined from a test bed OCT instrument, that could be obtained with the SLD of Structure 2 was 7.85 μm in air. The ripple on the spectrum was as low as 0.1 dB for seven degree angled facet two section devices if the back section was used as an absorber. The idea of a transition carrier density (TCD) is not limited to 1.3 μm AMQW SLDs. It is general to all AMQW devices.

In the next chapter I demonstrate and compare measurements of a glass cover slip with time domain OCT, Fourier domain OCT, and synthesized OCT using broad spectral width SLDs centered at 1300 nm and broadly tunable AMQW lasers. Based on the measured data, image enhancement with blind and not blind deconvolution methods is introduced.

5 OCT Measurements and OCT Image Processing

5.1 Introduction

In this chapter, I describe OCT measurements of a glass cover slip using time domain, Fourier domain, and synthesized OCT with our custom-designed AMQW light sources — broad spectral width SLDs and broadly tunable AMQW lasers. The 2D images were created with the Matlab function ImageSC( ). My work on OCT image enhancement with blind/non-blind deconvolution will also be demonstrated. A deconvolution technique can be applied when the OCT system is a linear shift invariant (LSI) system.[5] For a LSI imaging system, the measured image $H(x)$ can be described as the object $W(x)$ convolved with a point spread function (PSF) $S(x)$: $H(x) = W(x) \otimes S(x)$. The point spread functions for the time domain, Fourier domain, and synthesized OCT can be measured by replacing the sample with a mirror. For time domain OCT, the PSF function is the autocorrelation function of the emission of the SLD, under the assumption that the OCT system is perfectly aligned.[5] The Jansson Van Cittert method[62] was applied for the deconvolution of measurements where the PSF could be considered as known. However, an OCT system requires submicrometer alignment of the optics, and drift or aberrations in the optics can lead to a PSF that changes with time or is not identically equal to the autocorrelation function. Furthermore, the autocorrelation function for synthesized OCT is of a complicated format by having secondary peaks, as shown in Fig. 2.7 in Chapter 2. This makes the shape of the PSF more likely to be complex and subject to slow variations with time. Thus, it is concluded that an advanced deconvolution algorithm should be used for the OCT image processing. Based on this consideration, a Richardson-Lucy method[63] was applied as a blind deconvolution algorithm to perform image enhancement for the measurements. The measured point spread functions were taken as the starting points for the blind deconvolution.

5.2 Comparison of OCT Measurements

5.2.1 Time Domain OCT Measurement of a Glass Cover Slip

Figure 5.1 is a schematic of the free-space time domain OCT imaging setup in our lab. A 1.3 μm double-section SLD cleaved from wafer #M0446 was used as the light source. The front section and back section were 750 μm and 400 μm long respectively, and it was driven with 280 mA in the front and 7.2 mA in the back in order to get a flat spectrum. The interference signal was modulated at 1 kHz by placing a chopper in front of the detector and then demodulated with the lock-in amplifier to suppress the noise. The low frequency noise could be caused by the air flow in both or one arm of the interferometer, or vibration of the optical table. The motor in the reference mirror was applied for longitudinal scanning and the motor in the sample arm was used for transverse scanning to build the 2D image.

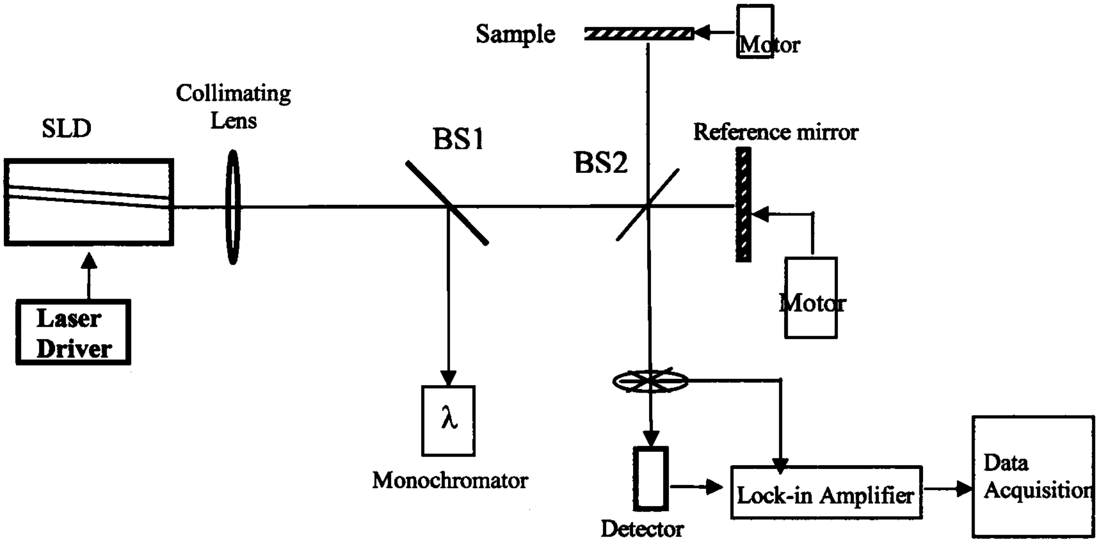

Figure 5.1 Schematic of the time domain OCT

The raw data for one longitudinal scan of a glass cover slip is shown in Fig. 5.2 (a) and its envelope is shown in Fig. 5.2(b), which was obtained by data processing with LabVIEW^{TM} 7.0. This was achieved by processing the raw data with a bandpass filter to suppress the noise, subtracting the mean value of the data, and using the absolute function as a bridge rectifier to flip the negative to the positive. Finally low pass filtering the data resulted in the envelope function. It is known that the optical thickness of the cover glass is ≈ 230 μm in air. If the optical thickness is divided by the refractive index of the glass slide, which is taken to be 1.5, the thickness is found to be 153.3 ±5 μm. The 2D image was constructed with the Matlab function *imageSC()* and the 2D image is shown in Appendix D as Fig. D.1. Figure 5.3 (c) shows the autocorrelation function of this SLD light source. It is shown that the resolution for this light source is around 9.0 μm in air, close to the theoretical expectation of $\delta z = 0.441\, \lambda_o^2 / \Delta\lambda = 7.85$ μm for a 95 nm FWHM spectral width. The envelope of the interferogram of the glass slide was used as the point spread function (PSF) of the time domain OCT system to deconvolve with Jansson-Van Cittert's method.

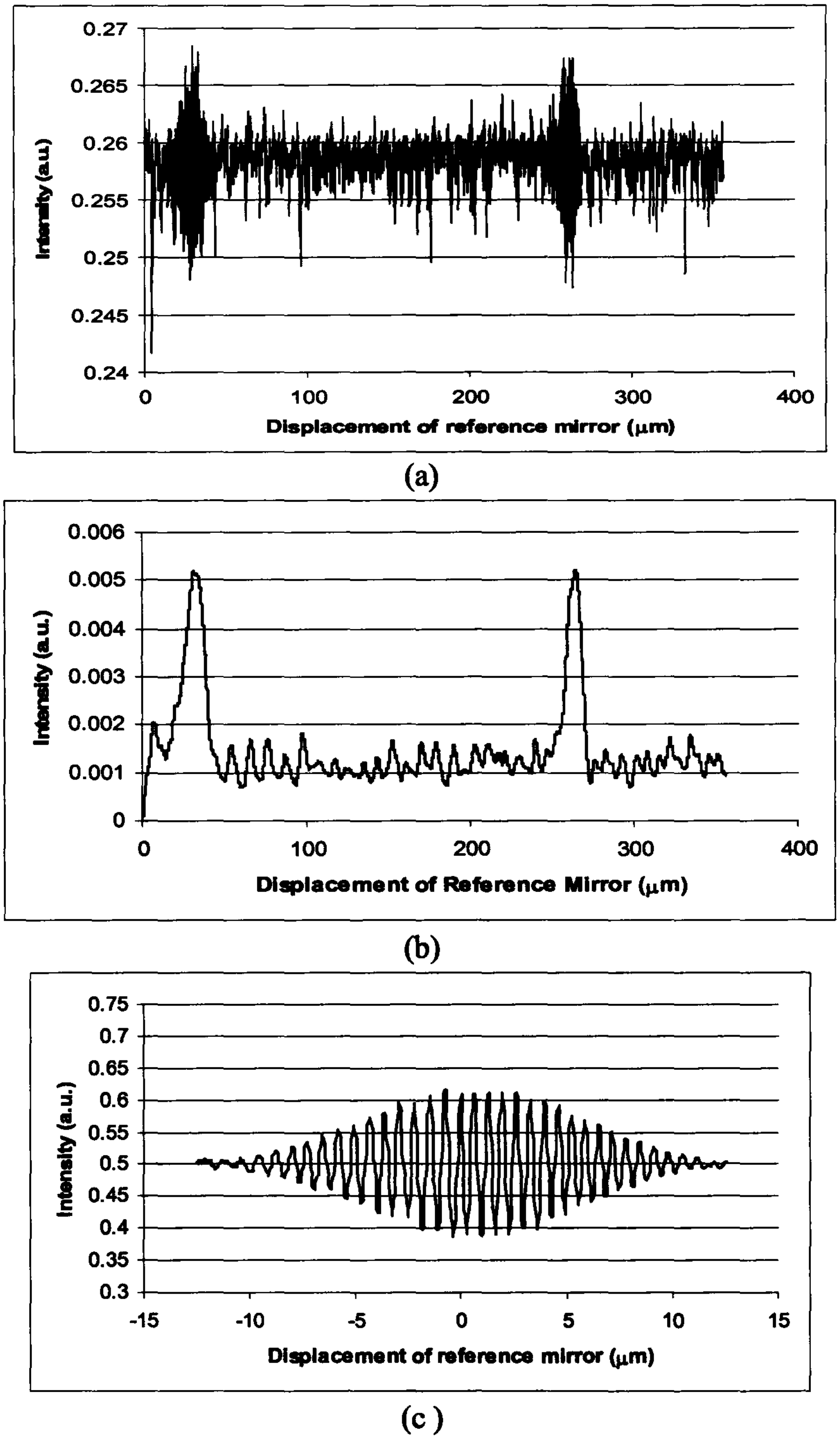

Figure 5.2 (a) One longitudinal scanning of a glass cover slip. (b) Envelope of (a). (c) Autocorrelation function of the 1.3 μm SLD.

5.2.2 Fourier Domain OCT Measurement of Glass Cover Slip

Measurements on a glass cover slip by Fourier domain OCT were performed with a 1.55 μm AMQW tunable laser as demonstrated in Chapter 2. A laser with a longitudinal mode spacing of ~1 nm was used for the measurement, thus the measuring range was ~ 400 μm in glass. Figure 5.3 shows the result of one depth measurement on one point on the glass cover slip. The resolution for this Fourier domain OCT is 13 μm in air which is achieved by tuning the AMQW laser from 1488 nm to 1605 nm (tuning range of 117 nm with a FWHM of ~80 nm). These data were taken at the same time as the work reported in Chapter 2. A 2D image was built with the Matlab function *imageSC( )* and the 2D image is shown in Appendix D as Fig. D.2(a).

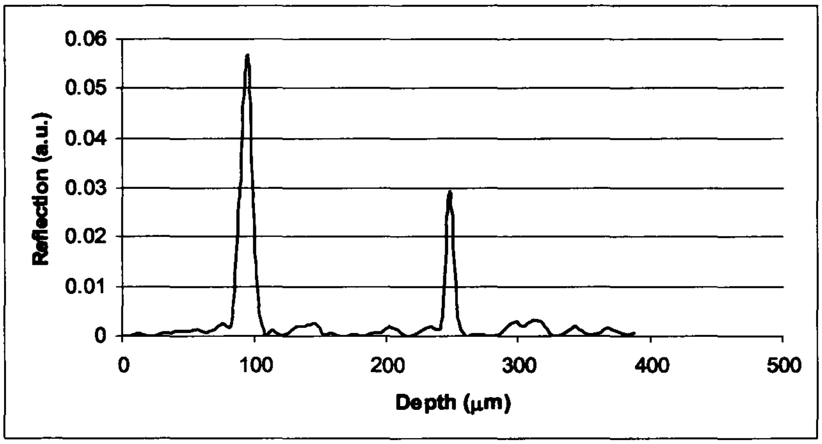

Figure 5.3 Fourier domain OCT measurement of single point on a cover glass slip

5.2.3 Synthesized OCT Measurement of Glass Cover Slip

The raw data for one depth measurement at one point on a glass cover slip with synthesized OCT with the 1.55 μm AMQW tunable light source are shown in Fig. 5.4 (a) and the envelope of the interferogram is shown in Fig. 5.4(b). There are secondary peaks beside the central peak in the interference fringes, due to the secondary peaks in the autocorrelation function of the synthesized light source, as shown in Fig. 5.4 (c). The tunable range of the 1.55 μm tunable laser was from 1497 nm to 1592 nm (95 nm tuning range with FWHM of 65 nm) for this measurement. Thus the resolution for this measurement is around 18 μm as shown in Fig. 5.4 (c). It will be shown that the secondary peaks could be removed by deconvolving the signal with the PSF function of the synthesized OCT, as shown in Section 3 in this chapter. The 2D image built with Matlab^{TM} function *imageSC( )* is shown in Appendix D as Fig. D. 3.

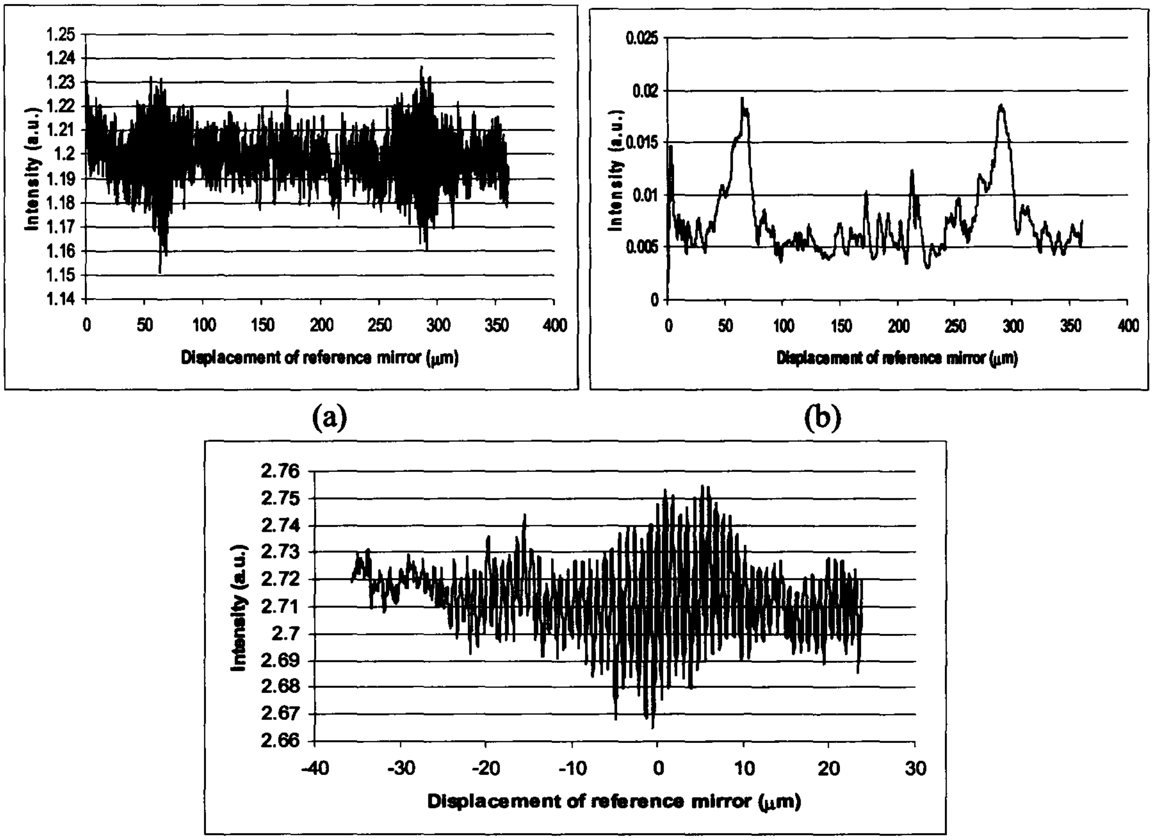

(a) (b)

(c)

Figure 5.4 (a) One longitudinal scanning with synthesized OCT of a cover glass slip (b) Envelope of (a). (c) Autocorrelation function of SOCT with the 1.55 μm tunable laser working as a incoherent source.

5.3 OCT Image Processing—Blind/non-blind Deconvolution

5.3.1 Describing OCT Setup as a Linear Shift Invariant (LSI) System

As derived in Chapter 2, for time domain OCT, the electric fields returning from the reference mirror $a_R E_I(t)$ and the object arm $a_O E_I(t)$ interfere at the detector. The detector performs a time averaging operation for the interference signal. Mechanically scanning the reference mirror generates an alternating component of the detector current which is the cross-correlation of $a_R E_I(t)$ and $a_O E_I(t)$. The cross-correlation $\Gamma_{RO}(\Delta r)$ is a function of the round-trip optical path difference Δr between the reference and sample arms $\Delta r = 2n(r_R - r_o)$. By placing a mirror in the object arm, an autocorrelation function will be detected by scanning the mirror in the reference arm, which is $\Gamma_{RR}(\Delta r)$. The correlation functions are expressed as:

$$\Gamma_{RO}(\Delta r) = \left\langle a_R E_1(t) a_O E_1^*(t + \Delta r / c)\right\rangle$$

$$\text{and } \Gamma_{RR}(\Delta r) = \left\langle a_R E_1(t) a_R E_1^*(t + \Delta r / c)\right\rangle \tag{5.1}$$

Now we treat the OCT system as a linear shift invariant (LSI) system. The point spread function of the LSI system is the autocorrelation function $\Gamma_{RR}(\Delta r)$. Then the measured image, which is the cross-correlation function, can be written as:

$$\Gamma_{RO}(\Delta r) = \Gamma_{RR}(\Delta r) \otimes a_O(r) \tag{5.2}$$

where $a_O(r)$ is the object reflectivity in function of r. In general form, the image $H(x)$ is written as the convolution of the object $W(x)$ and the point spread function $S(x)$:

$$H(x) = W(x) \otimes S(x) \tag{5.3}$$

The point spread function of the time domain OCT system was measured with the same SLD light source. It is shown in Fig. 5.5 (a). The PSF for Fourier domain OCT, which is shown in Fig. 5.5 (b), was measured by replacing the sample with a mirror, tuning the laser to record the interferogram, and then taking the Fourier transform. Figure 5.5 (c) is the PSF function for synthesized OCT by synthesizing the tunable AMQW laser as an incoherent light source. These functions are plotted as a function of data acquisition points so that it is convenient for deconvolution.

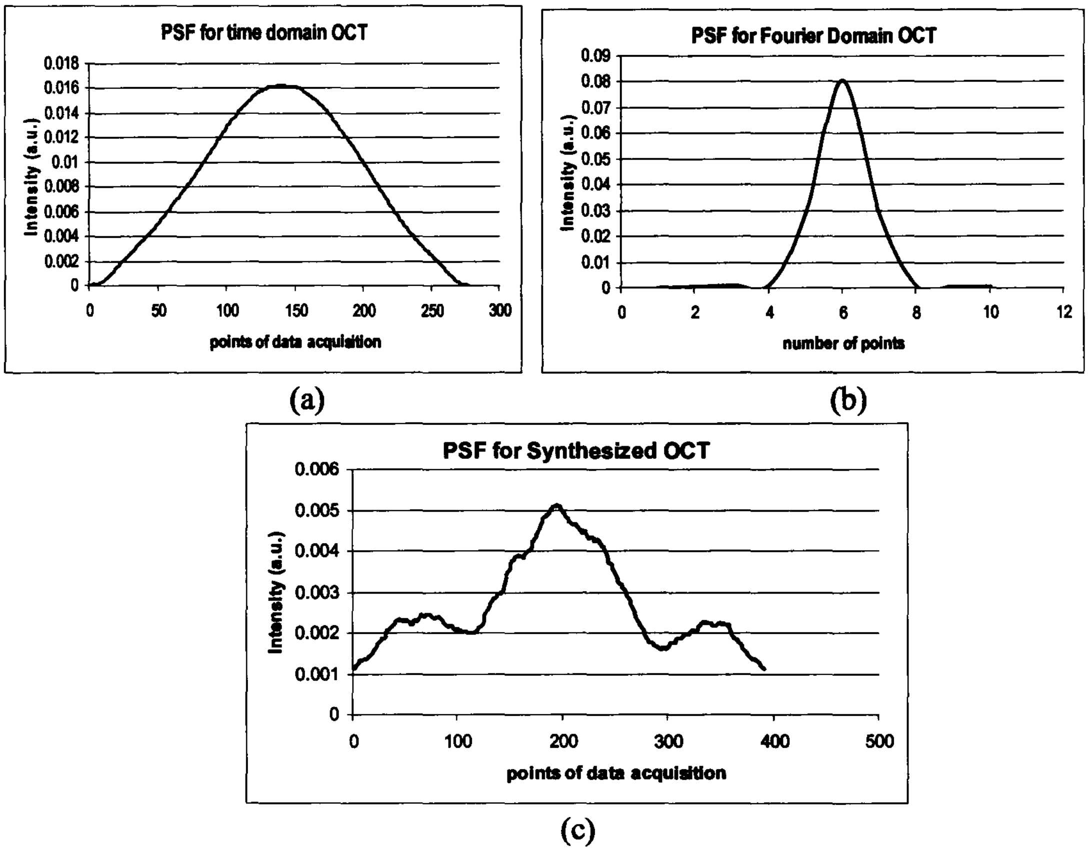

Figure 5.5 Point spread functions for (a) time domain OCT, (b) Fourier domain OCT, and (c) synthesized OCT

5.3.2 Noise Analysis of Our OCT System

The detector current consists of both signal and noise components. The noise of the OCT system includes three terms: relative intensity noise (RIN) of the light source, optical path noise, and shot noise from the detector. The RIN from the light source could be eliminated by dual balanced detection[64]. The optical path noise could introduce low frequency noise to the interference fringes due to air flow, vibrations, or thermal effects in the optical path. I estimate the total noise could be considered as a Gaussian distribution. Because our setup is a free-space OCT and it is expected to have all three types of noise as mentioned above, my work is thus not targeting on obtaining high signal-to-noise ratio. I applied intensity modulation with a mechanical chopper in front of the detector and demodulated with a lock-in amplifier to avoid low frequency noise such as optical path noise and intensity fluctuations from the light source. The purpose of my work is to demonstrate how our AMQW light sources work for OCT and image enhancement.

5.3.3 Deconvolution with Jansson Van Cittert's Method

Van Cittert's method[62] takes the image data $H(x)$ as a first approximation $W^0(x)$ to the object function $W(x)$. Convolving $W^0(x)$ with the PSF of the system $S(x)$, we get $H^0(x) = S(x) \otimes W^0(x)$. The difference between the image $H(x)$ and the convolved result $H^0(x)$ is considered as the error in the estimate of the object, $W(x) - W^0(x)$. Van Cittert's method applies this image-estimated error as a correction to the object estimate, thus producing a new object estimate. One may continue this process by the iteration as follows:

$$W^{n+1}(x) = W^n(x) + [H(x) - S(x) \otimes W^n(x)] \tag{5.4}$$

with the initial guess for the object as $W^0(x) = H(x)$.

Because of the convolution relation of $H(x) = W(x) \otimes S(x)$, a one dimension object $W(x)$ with I points and a point spread function $S(x)$ with J points, the image $H(x)$ will have $K = I+J-1$ points. Therefore in realization of Van Cittert's method, one has to keep cutting the extra points of $(J-1)/2$ on both sides of the calculated object $W^n(x)$ after each iteration.

Unfortunately Van Cittert's method could lead to spurious high frequency components and often gives rise to non-physical results. In my calculation, it was found that the deconvolved object has negative values at some points, which is not physically correct for imaging systems. Jansson (Chapter 4 in Ref. 74) modified Van Cittert's method by adding a constraining term r:

$$W^{n+1}(x) = W^n(x) + r(x)[H(x) - S(x) \otimes W^n(x)] \tag{5.5}$$

In my case, r was chosen to correct those negative points as defined as:

$$r(x) = \begin{cases} 0 & W^n(x) < 0 \\ 1 & others \end{cases} .$$

The deconvolution result with Jansson-Van Cittert's method will be shown in the next section in order to compare it with the Richardson-Lucy algorithm.

5.3.4 Blind Deconvolution with Richardson-Lucy Algorithm

Richardson[65] developed an iterative method of deconvolution from Bayes' theorem. Bayes' theorem gives a way to calculate *a posteriori* probabilities $P(W|H)$ of the event W in terms of *a priori* probability $P(W)$ and the conditional probabilities $P(H|W)$.

$$P(W_i \mid H_k) = \frac{P(H_k \mid W_i)P(W_i)}{\sum_j P(H_k \mid W_j)P(W_i)} \tag{5.6}$$

By using the theorem on the total probability as:

$$P(W_i) = \sum_k P(W_i \mid H_k)P(H_k) \tag{5.7}$$

The object $W(x)$ could be rewritten as:

$$P(W_i) = \sum_k P(W_i \mid H_k)P(H_k) = \sum_k \frac{P(H_k \mid W_i)P(W_i)}{\sum_j P(H_k \mid W_j)P(W_i)} P(H_k) \tag{5.8}$$

Thus the iteration to recover the object based on the known image and the PSF is given by:

$$W_i^{(n+1)} = W_i^{(n)} \sum_k \frac{S_{ki}H_k}{\sum_j S_{kj}W_j^{(n)}} = W_i^{(n)}(x)\left\{\left[\frac{H(x)}{W(x)\otimes S(x)}\right]\otimes S(-x)\right\} \tag{5.9}$$

Because Richardson's technique is based on probability, positivity of the solution is ensured. Thus the nonnegativity constraint is included automatically in Richardson's method.

To demonstrate the deconvolution with Jansson-Van Cittert's method and the Richardson algorithm, a synthesized image and a synthesized PSF were constructed as shown in Fig. 5.6. This PSF was made to have secondary peaks to be comparable with the synthesized OCT point spread function. (Simulations have been performed to make sure that simple PSFs such as a Guassian shape would work well with both deconvolution methods). The synthesized image was built with a small peak which is merged with the third peak from the left side. We could see that both Jansson's method and the Richardson-Lucy algorithm could separate the merged peaks after deconvolution. Jansson's method is noisy at the points close to zero. One more constraint was applied for both Jansson's method and the Richardson-Lucy algorithm to suppress the peculiar peaks at the left side and right side of the deconvolved objects. The constraint is (*I* is the total points of the object *W(i)*):

$$r(i) = \begin{cases} 0.3 + 0.7 * i/8 & i \le 8 \\ 1 & others \\ 0.3 + 0.7 * (I - i)/8 & (I - i) \le 8 \end{cases}$$

This constraint is also applied for the final OCT image blind deconvolution calculations. One hundred iterations were applied for Jansson's method. Two hundred iterations were used for Richardson algorithm because it converges slower than Jansson's method.

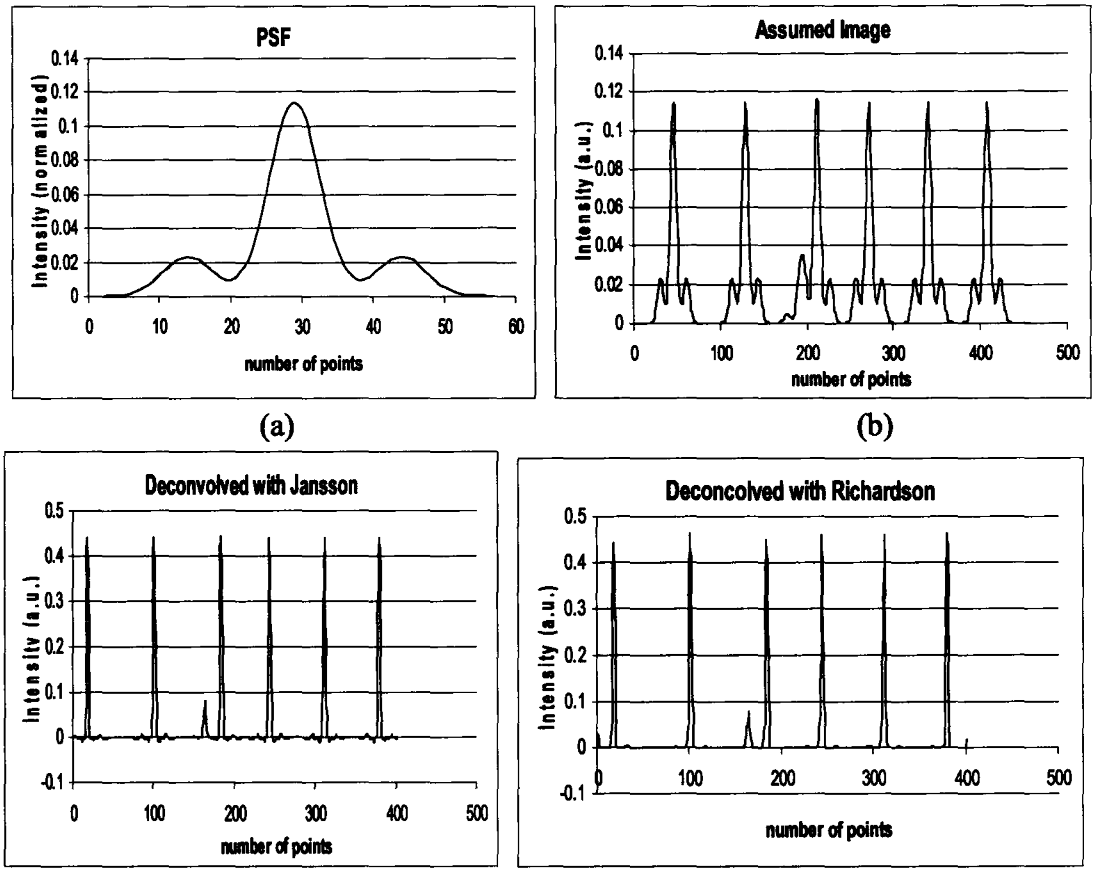

(a) (b)

(c) (d)

Figure 5.6 Demonstration of Jansson's deconvolution method and Richardson-Lucy algorithm. (a) Simulated PSF (b) Simulated blurred image with the third peak merged with a small peak. (c) Deconvolved with Jansson's method. (d) Deconvolved with Richardson-Lucy algorithm.

In Fig. 5.7(a), noise was added to the synthesized image by generation of a random number lying on a Gaussian distribution with the mean of the pixel value and a standard deviation of 0.005. It can be seen from Fig. 5.7(b) and (c) that both methods can separate the merged peaks and the Richardson algorithm could obtain low noise results. Therefore, we could be confident that with real measurement data with noise, the Richardson algorithm would still work.

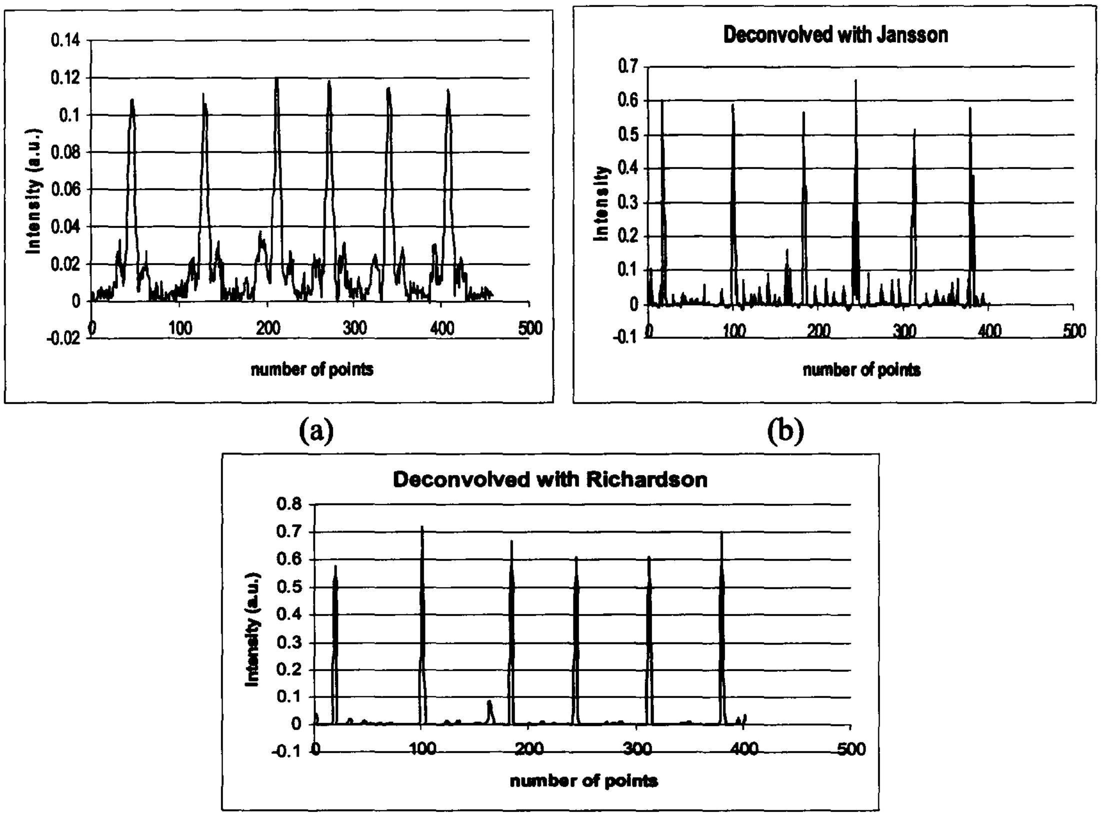

(a) (b)

(c)

Figure 5.7 Deconvolution with Gaussian white noise on the synthesized image. (a) Synthesized image with Gaussian white noise of standard deviation 0.005. (b) Deconvolved with Jansson's method. (c) Deconvolved with the Richardson-Lucy algorithm.

However, the broadening effect of the OCT measurement is more complicated than the autocorrelation function, which could be measured with a Michelson interferometer. One concern is that the light scattered from the different depths of a sample will interfere with each other and this will generate further disturbances on the image. Other effects that cause uncertainties in the PSF function include non-perfect alignment of the two Michelson interferometer arms, phase front distortion by large-scale index variations, multiple backscattering in the sample,[66] index inhomogenities, and unexpected noise in the OCT system. Thus, we believe that an advanced deconvolution algorithm which could calculate the point spread function based on the known image should be used for the OCT image processing. Based on this consideration, a Richardson-Lucy method[63] was investigated in my thesis research as the blind deconvolution algorithm to do the image enhancement for the OCT measurements. The measured point spread functions were taken as the initial guess for the starting point of the blind deconvolution.

In the blind form of the Richardson-Lucy deconvolution algorithm, it is assumed that the PSF function follows the same statistical fluctuation as the signal. By taking the measured autocorrelation function as the initial guess for the PSF $S^0(x)$, at the *n*th iteration, it is assumed that the object is known from the $n-1$ iteration. The PSF $S^n(x)$ is then calculated for a specified number of iterations as follows:

$$S_i^{n+1} = S_i^n(x)\left\{\left[\frac{H(x)}{S_i^n(x)\otimes W^{n-1}(x)}\right]\otimes W_i^n(-x)\right\} \tag{5.10}$$

Equation (5.9) in the blind form will be rewritten as:

$$W_i^{n+1} = W_i^n(x)\left\{\left[\frac{H(x)}{W_i^n(x)\otimes S^{n-1}(x)}\right]\otimes S_i^n(-x)\right\} \tag{5.11}$$

In Ref. 65, Richardson showed how to do the convolution point by point in the format of Eq. (5.10). It could be extended easily to the blind format.

The blind deconvolution with the Richardson-Lucy algorithm was performed for image processing of the time domain, Fourier domain, and synthesized OCT data. The blind-deconvolved 2D images of a cover glass slip are shown in Appendix D in comparison with the original images. The blind-deconvolved point spread functions for the time domain, Fourier domain, and synthesized OCT are shown in Fig. 5.8 (a), (b) and (c) respectively.

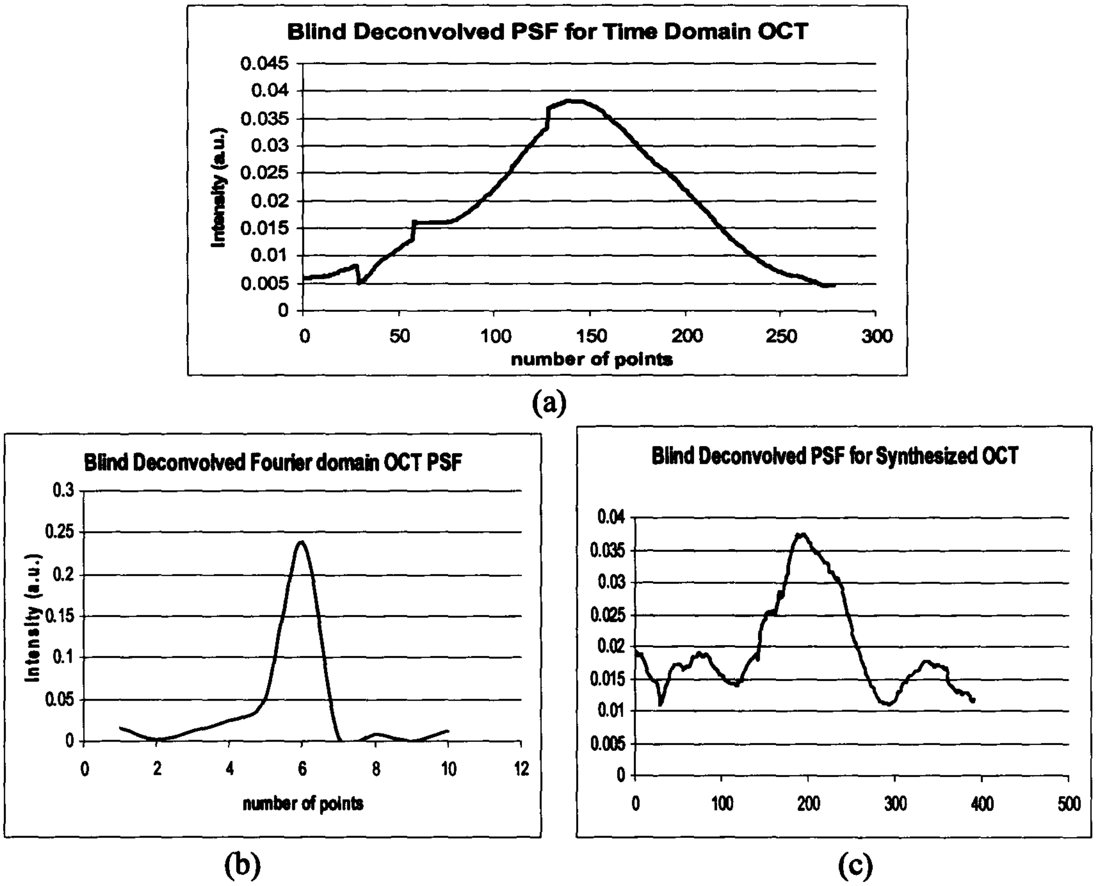

(a)

(b)

(c)

Figure 5.8 Blind deconvolved PSF for (a) time domain OCT. (b) Fourier domain OCT. and (c) Synthesized OCT.

The depth data at one point on a cover glass slip before and after blind deconvolution are shown in Fig. 5.8.

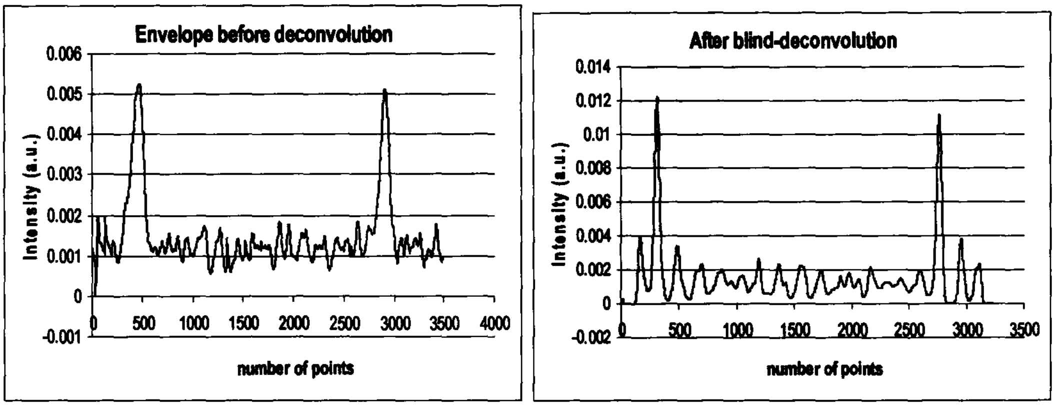

(a) time domain OCT measurement of cover glass slip

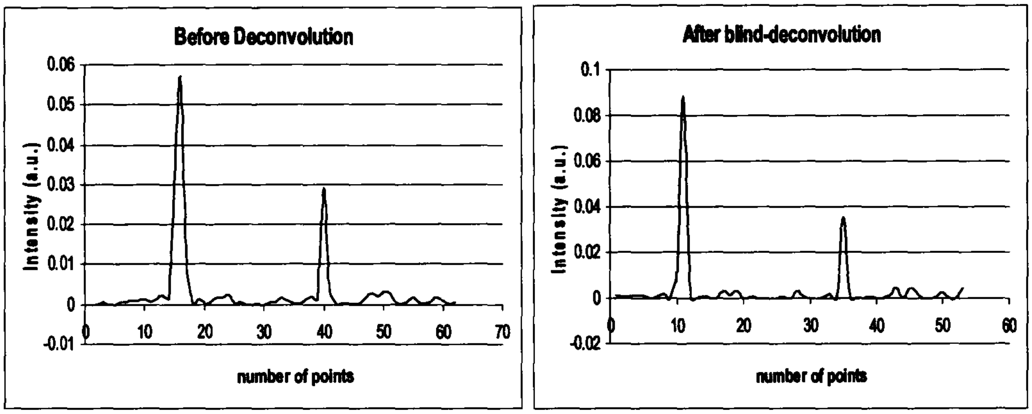

(b) Fourier domain OCT measurement of cover glass slip

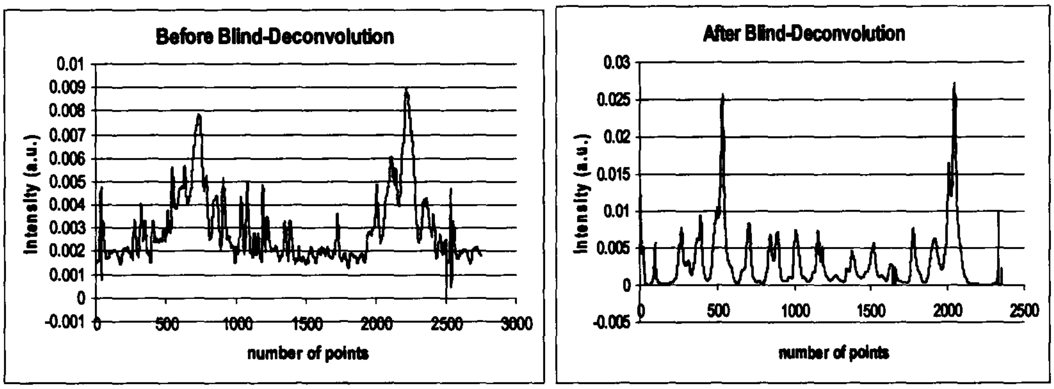

(c) Synthesized OCT measurement of cover glass slip

Figure 5.9 Effect of image enhancement with Richardson-Lucy algorithm.

5.3.5 Discussion

From Fig. 5.8 it can be concluded that deconvolution can enhance the OCT image by narrowing the peaks and improving the image contrast. The blind-deconvolved point spread functions (see Fig. 5.7) show that changes should be made to the measured PSFs, either by introducing bumps on the PSF, (time domain Fig. 5.7 (a) and synthesized OCT Fig. 5.7 (c)) or by changing the slope of one side of the PSF (Fourier domain, Fig. 5.7 (b)). For Fourier domain OCT, the PSF asymmetry is caused by the misalignment of the reference mirror and the sample. My simulations of two beam interference with one arm tilted by an angle as small as 2° cause the slopes on the left side and on the right side of the PSF function to be asymmetric. For the blind-deconvolved PSF of time domain and synthesized OCT, the bumps on the point spread function are explained as the aberration of the optics in the OCT setup. The aberration of the optics in the OCT setup, due to the collimating lens or the beam splitter, could cause the phase distortion in the reference arm or the sample arm, generating non-ideal interference fringes which will be connected to the point spread function of the system. This work has shown that the blind deconvolution is necessary and shows superior performance in the image enhancement of OCT over nonblind deconvolution. This is also indicated in Ref. 67.

From the deconvolved image of the synthesized OCT shown in Fig. 5.8(c), one can see significant suppression of secondary peaks by the deconvolution. The sharp boundaries of the glass border are clearly resolved in the 2D deconvolved image (see Appendix D).

5.4 Conclusion

In this chapter, the application of our custom-designed 1.3 μm AMQW SLD for time domain OCT and a comparison with the results of Fourier domain OCT and of synthesized OCT are shown. The resolution for time domain OCT is 9.0 μm in air, compared with 13 μm for Fourier domain, and 18 μm for synthesized OCT. It was also found in my research that image processing with blind deconvolution is necessary for enhancement of OCT images. Jansson-Van Cittert's method and a Richardson-Lucy algorithm were applied for deconvolution in my work. It was found by the blind deconvolution that the point spread function is different than the measured autocorrelation function in that the blind deconvolved PSFs show asymmetry or bumps in their shapes. I explained this phenomenon as the aberration of the optics and misalignment of the reference mirror. Suppression of secondary maxima in the reconstructed objects of synthesized OCT was shown by deconvolution of the 2D images.

6 Conclusion

6.1 Summary of the Thesis

Optical coherence tomography (OCT) is currently an active area of research in the application of optical technology to the fields of medicine and biology in recent years. I performed research on the application of AMQW InGaAsP/InP tunable lasers and broad spectral width superluminescent diodes (SLDs) as light sources for OCT. For my thesis I investigated three areas. First, I investigated the application of 1.55 μm short external cavity (SXC) AMQW InGaAsP/InP tunable lasers for Fourier domain OCT and for synthesized OCT. A diffractive optical element (DOE) was used as the short external cavity for the AMQW tunable laser. It was shown that the DOE enabled broadly tunable, single longitudinal mode operation over a spectral width of 117 nm, and the most impressive feature for this tunable laser was that the tuning was realized by only linear translation of the DOE. It was shown that the depth resolution for Fourier domain and for synthesized OCT with an SXC AMQW 1.55 μm laser was 13 μm in air. This work should increase interest for DOE enabled broadly tunable lasers in a variety of applications. A DOE SXC could be realized with MEMS and integration with semiconductor lasers could further reduce the size and the cost of broadly tunable diode lasers. The design and realization of a MEMS-based DOE broadly tunable AMQW laser has been suggested to the MEMS research group in our department and some research has been performed toward this goal.

Second, I performed research on a light source for time domain OCT: an AMQW broad spectral width SLD. Both optimization of the waveguide and design of the active region were investigated. The target for the waveguide optimization was to optimize the optical confinement factor of the ridge waveguide. It was shown that by increasing the confinement factor by ~ 40 %, the output power of the SLD was successfully enhanced over 90%. My work on the design of the active region was based on the experience of Dr. Michael Hamp. I demonstrated through measurement that the transition carrier density (TCD) has to be high in order to achieve high output power for an SLD. Double section ridge waveguides were processed and a small pumping current for the back section helped to broaden the spectral width on the long wavelength (i.e., the red) side. Over 90 nm of FWHM bandwidth and a maximum output power of 2 mW were obtained with this 1.3 μm SLD design. The ripple in the spectral output was shown to be as low as 0.1 dB.

The third part of my work was OCT measurements with the custom-designed AMQW SLDs and the broadly tunable SXC AMQW lasers. I constructed and used a free-space OCT test bed based on a Michelson interferometer. A glass cover slip was chosen as the sample to compare measurements with time domain, Fourier domain, and synthesized OCT. By taking the OCT measurement system as a linear shift invariant (LSI) system, I performed image processing with blind/nonblind deconvolution algorithms to improve the image contrast. A Jansson-Van Cittert method and a Richardson-Lucy algorithm were adopted to do this work. It was shown by blind deconvolution calculations that, compared with the measured point spread function, the PSF should include effects due to misalignment and aberrations of the OCT system.

6.2 *Suggestion for Future Work*

6.2.1 1.3 μm Tunable Laser Diode

With the same growth of wafer #M0446, I processed 1.3 μm diode lasers with ridge widths of 2, 3, and 4 μm. It was found that the output power could be as high as 20 mW with a 400 μm cavity length. The high power of this laser is due to the optimization of the waveguide structure by maximizing the confinement factor. Various cavity lengths were cleaved in order to find the transition cavity length of this 1.3 μm AMQW laser. The shortest cavity length that was cleaved was 200 μm, and it lased at a peak wavelength of 1297.1 nm. At a 400 μm cavity length, the laser operated at 1318.8 nm. It would be straightforward to try the 1.3 μm laser with the SXC DOE. I expect over 30 nm tunability and high power, which might make the laser interesting as a light source for low depth resolution Fourier domain and synthesized OCT.

6.2.2 SLD Waveguide with Low Beam Divergence Far Field

In my development of simulations for calculating the optical confinement factor, I also investigated means to achieve low beam divergence for 1.3 μm SLDs. I did not complete the investigation. I think that meaningful results on minimization of the beam divergence could be obtained by simulations and then using one or more growths to validate the simulations. By reducing the beam divergence of the SLD, the coupling efficiency into the optical fiber would be significantly improved. This is a desired property by a fiber-based OCT system. B. Qiu *et al*[68] showed that by adding a new epitaxial layer in the lower cladding layer, which they called the far-field reduction layer, one could reduce the vertical far-field and suppress higher order mode lasing.

6.2.3 FPGA for Blind Deconvolution on OCT Setup

Instead of the image enhancement with the software as introduced in the thesis, a real-time image enhancement with blind deconvolution methods could be realized with a field-programmable gate array (FPGA) based processor. This technique could further improve the image quality of an OCT system. This work is relatively independent and could be assigned as a Master's project.

Based on my Ph. D. research work toward the design and application of AMQW light sources for OCT, I believe that AMQW SLDs are an ideal light source for time domain OCT. The divergence angle of SLDs could be further improved by changing the waveguide design in order to increase the coupling efficiency to the optical fiber. The broadly tunable AMQW laser with DOE as the short external cavity could tune the laser >100 nm would be a good light source for Fourier domain OCT. This is important for real-time Fourier domain OCT imaging. Synthesized OCT has no synchronous requirement, but fast tunability is required to reduce the averaging time of the low pass filter. Fast tunability could be realized with coupled cavity AMQW lasers, or flat-gain coating of AMQW lasers. Both of these devices are currently being investigated in our department. As the conclusion of this thesis work, AMQW devices would be a good choice for OCT light sources.

Appendix A Experimentally Grown SLD Structures

This appendix provides the detailed structure growth parameters for the experimental AMQW SLDs that were grown at McMaster University and at the Canadian Photonics Fabrication Center (CPFC) in Ottawa. Wafer #3979 and Wafer # 4177 were grown by gas-source, molecular beam epitaxy (MBE), with device processing performed on the wafers to produce angled-facet ridge-waveguide SLDs. Wafer # M0446 was grown by metal-organic chemical vapor deposition (MOCVD) and was processed at the CPFC through *CMC Microsystems*. The tabulated data presented in this appendix gives the thickness and composition of each layer in the structure. Varying bandgap In$_{1-x}$As$_x$As$_y$P$_{1-y}$ layers are used to create the separate confinement heterostructure (SCH), barriers, and QW layers.

Table A.1 Wafer # 3979 1.3 µm AMQW SLD Growth Parameters

Thickness	Composition	Doping	Wavelength
0.15 µm (a_1)	p-InGaAs contact layer	$>10^{19}$	
1.25 µm (a_2)	p-InP	1.1×10^{18}	
0.15 µm (a_3)	p-InP	5×10^{17}	
75 Å (a_4)	p-$In_{0.72}Ga_{0.28}As_{0.61}P_{0.39}$	5×10^{17}	
0.15 µm (a_5)	p-InP	5×10^{17}	
800 Å (a_6)	$In_{0.92}Ga_{0.08}As_{0.175}P_{0.825}$	undoped	SCH
300 Å (a_7)	$In_{0.828}Ga_{0.172}As_{0.316}P_{0.684}$	undoped	Barrier
50 Å	$In_{0.828}Ga_{0.172}As_{0.60}P_{0.40}$	undoped	λ_A=1340 nm
75 Å	$In_{0.828}Ga_{0.172}As_{0.316}P_{0.684}$	undoped	Barrier
50 Å	$In_{0.828}Ga_{0.172}As_{0.59}P_{0.41}$	undoped	λ_A=1330 nm
75 Å	$In_{0.828}Ga_{0.172}As_{0.316}P_{0.684}$	undoped	Barrier
50 Å	$In_{0.828}Ga_{0.172}As_{0.55}P_{0.45}$	undoped	λ_A=1289 nm
75 Å	$In_{0.828}Ga_{0.172}As_{0.316}P_{0.684}$	undoped	Barrier
50 Å	$In_{0.828}Ga_{0.172}As_{0.53}P_{0.47}$	undoped	λ_A=1260 nm
75 Å	$In_{0.828}Ga_{0.172}As_{0.316}P_{0.684}$	undoped	Barrier
50 Å	$In_{0.828}Ga_{0.172}As_{0.525}P_{0.475}$	undoped	λ_A=1256 nm
300 Å (a_9)	$In_{0.828}Ga_{0.172}As_{0.316}P_{0.684}$	undoped	Barrier
800 Å (a_{10})	$In_{0.92}Ga_{0.08}As_{0.175}P_{0.825}$	5×10^{17}	SCH
0.6 µm (a_{11})	n-InP	1×10^{18}	
n-InP substrate			

Table A.2 Wafer # 4177 AMQW SLD Growth Parameters

Thickness	Composition	Doping	Wavelength
0.15 μm (a_1)	p-InGaAs contact layer	$>10^{19}$	
1.25 μm (a_2)	p-InP	1.1×10^{18}	
0.15 μm (a_3)	p-InP	5×10^{17}	
75 Å (a_4)	p-$In_{0.72}Ga_{0.28}As_{0.61}P_{0.39}$	5×10^{17}	
0.15 μm (a_5)	p-InP	5×10^{17}	
800 Å (a_6)	$In_{0.92}Ga_{0.08}As_{0.175}P_{0.825}$	undoped	SCH
300 Å (a_7)	$In_{0.828}Ga_{0.172}As_{0.316}P_{0.684}$	undoped	Barrier
50 Å	$In_{0.828}Ga_{0.172}As_{0.62}P_{0.38}$	undoped	λ_A=1326.3 nm
75 Å	$In_{0.828}Ga_{0.172}As_{0.316}P_{0.684}$	undoped	Barrier
50 Å	$In_{0.828}Ga_{0.172}As_{0.62}P_{0.38}$	undoped	λ_A=1326.3 nm
75 Å	$In_{0.828}Ga_{0.172}As_{0.316}P_{0.684}$	undoped	Barrier
50 Å	$In_{0.828}Ga_{0.172}As_{0.62}P_{0.38}$	undoped	λ_A=1326.3 nm
75 Å	$In_{0.828}Ga_{0.172}As_{0.316}P_{0.684}$	undoped	Barrier
50 Å	$In_{0.828}Ga_{0.172}As_{0.62}P_{0.38}$	undoped	λ_A=1326.3 nm
75 Å	$In_{0.828}Ga_{0.172}As_{0.316}P_{0.684}$	undoped	Barrier
50 Å	$In_{0.828}Ga_{0.172}As_{0.54}P_{0.46}$	undoped	λ_A=1246.4 nm
300 Å (a_9)	$In_{0.828}Ga_{0.172}As_{0.316}P_{0.684}$	undoped	Barrier
800 Å (a_{10})	$In_{0.92}Ga_{0.08}As_{0.175}P_{0.825}$	5×10^{17}	SCH
0.6 μm (a_{11})	n-InP	1×10^{18}	
n-InP substrate			

Table A.3 Wafer # M0446 AMQW SLD Growth Parameters

Thickness	Composition	Doping	Wavelength
0.2 μm (a_1)	p-InGaAs contact layer	$>10^{19}$	
1.26 μm (a_2)	p-InP	1.1×10^{18}	
0.20 μm (a_3)	p-InP	5×10^{17}	
50 Å (a_4)	p-$In_{0.72}Ga_{0.28}As_{0.61}P_{0.39}$	5×10^{17}	
0.08 μm (a_5)	p-InP	4×10^{17}	
700 Å (a_6)	$In_{0.92}Ga_{0.08}As_{0.18}P_{0.82}$	undoped	SCH
700 Å (a_7)	$In_{0.86}Ga_{0.14}As_{0.31}P_{0.69}$	undoped	SCH
200 Å (a_8)	$In_{0.828}Ga_{0.172}As_{0.32}P_{0.68}$	undoped	Barrier
50 Å	$In_{0.828}Ga_{0.172}As_{0.62}P_{0.38}$	undoped	λ_A=1326.3 nm
75 Å	$In_{0.828}Ga_{0.172}As_{0.316}P_{0.684}$	undoped	Barrier
50 Å	$In_{0.828}Ga_{0.172}As_{0.62}P_{0.38}$	undoped	λ_A=1326.3 nm
75 Å	$In_{0.828}Ga_{0.172}As_{0.316}P_{0.684}$	undoped	Barrier
50 Å	$In_{0.828}Ga_{0.172}As_{0.62}P_{0.38}$	undoped	λ_A=1326.3 nm
75 Å	$In_{0.828}Ga_{0.172}As_{0.316}P_{0.684}$	undoped	Barrier
50 Å	$In_{0.828}Ga_{0.172}As_{0.62}P_{0.38}$	undoped	λ_A=1326.3 nm
75 Å	$In_{0.828}Ga_{0.172}As_{0.316}P_{0.684}$	undoped	Barrier
50 Å	$In_{0.828}Ga_{0.172}As_{0.54}P_{0.46}$	undoped	λ_A=1246.4 nm
200 Å (a_{10})	$In_{0.828}Ga_{0.172}As_{0.32}P_{0.68}$	undoped	Barrier
700 Å (a_{11})	$In_{0.86}Ga_{0.14}As_{0.31}P_{0.69}$	undoped	SCH
700 Å (a_{12})	$In_{0.92}Ga_{0.08}As_{0.18}P_{0.82}$	undoped	SCH
0.6 μm (a_{13})	n-InP	1×10^{18}	
n-InP substrate		1×10^{18}	

Appendix B Mask design of 7 degree angled-stripe SLD

This is a four layer mask with colors of red, green, magenta, and yellow for the mesa, via, isolation, and metallization mask respectively. The isolation was designed to be 'z' shaped as shown in Fig.B.1 (b) to give more space for wire bonding. This is prepared for extremely short front or back sections.

The ridge width was designed to be 3, 4, 5, and 6 µm. The wafer will be cleaved along the wafer edge. The ratio of the front and back sections will change every other four devices, so that in one SLD bar, we could obtain two-section SLDs with various front to back ratios.

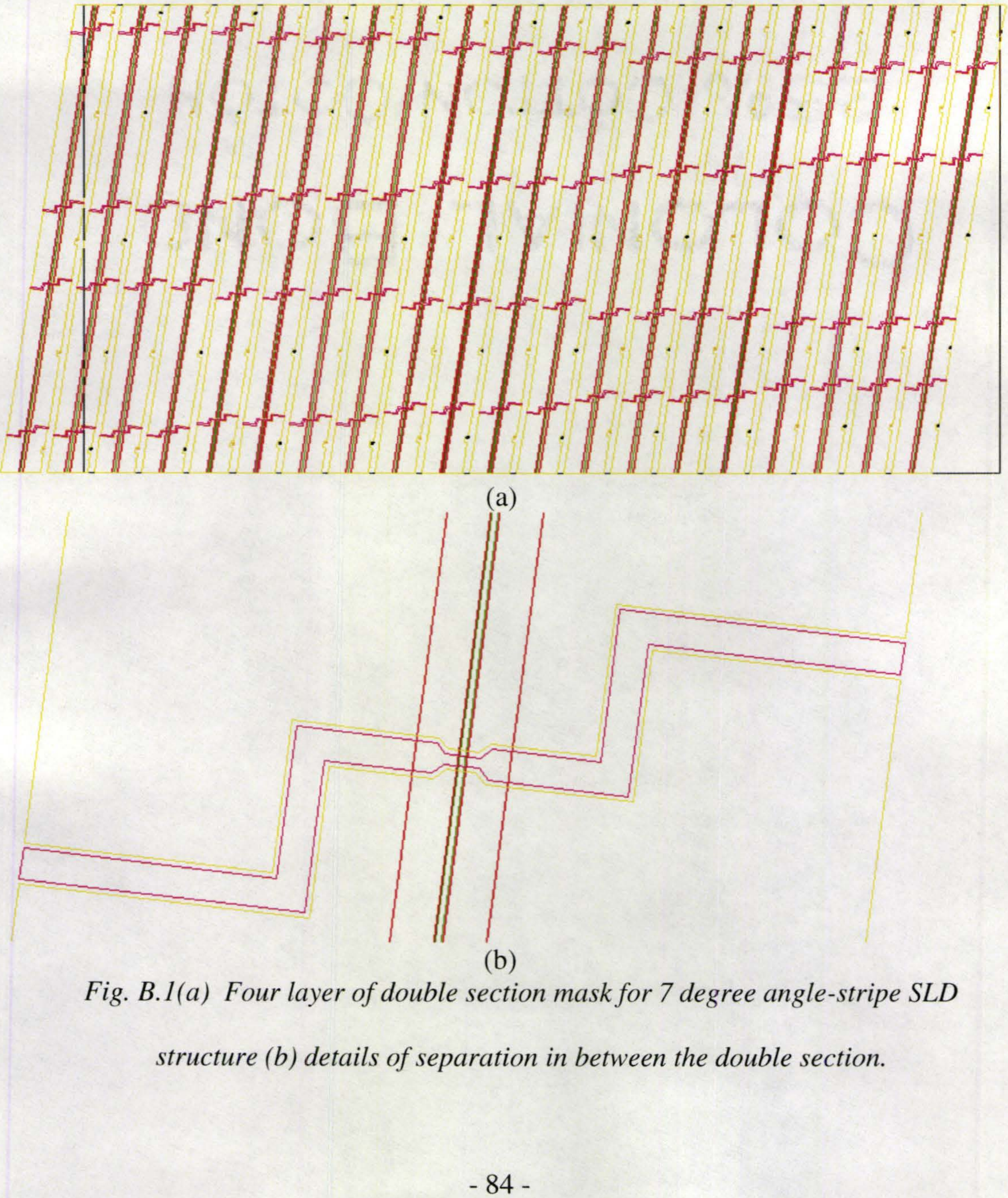
(a)

(b)

Fig. B.1(a) Four layer of double section mask for 7 degree angle-stripe SLD structure (b) details of separation in between the double section.

Appendix C Near field measurement of 7 degree angle-striped SLD

The near field measurements were performed with the help of Dr. Doug Bruce. All the devices were driven under low current to avoid saturation of the detector. It can be concluded that all lasers with varying ridge widths were running in a single spatial mode.

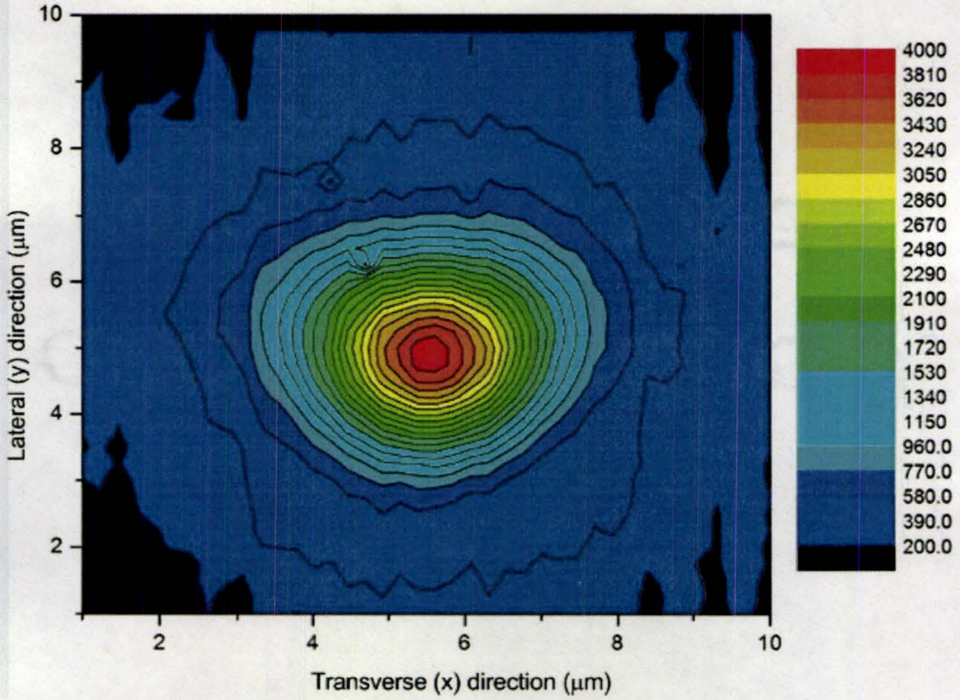

(a)

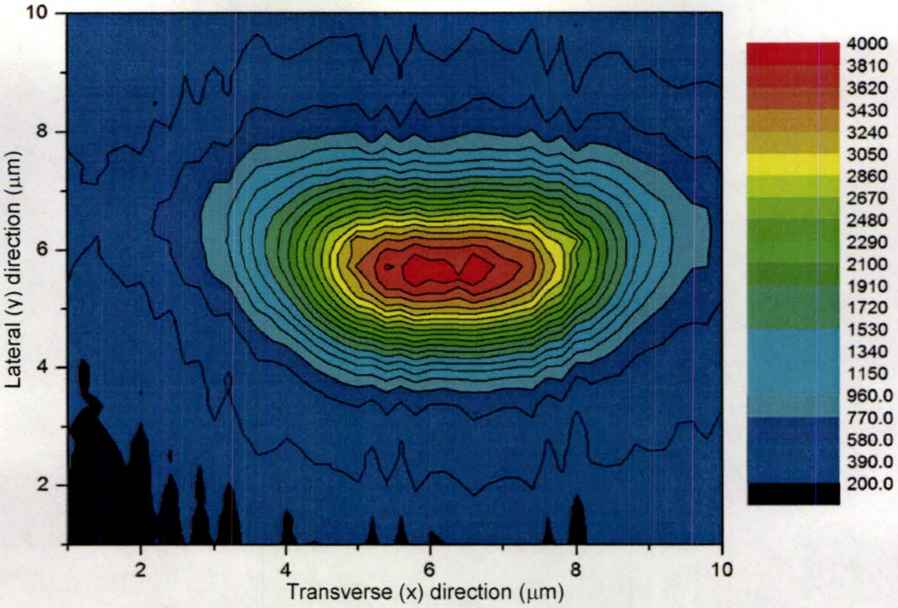
Lateral (y) direction (μm)
Transverse (x) direction (μm)
2
4
6
8
10
4000
3810
3620
3430
3240
3050
2860
2670
2480
2290
2100
1910
1720
1530
1340
1150
960.0
770.0
580.0
390.0
200.0

(b)

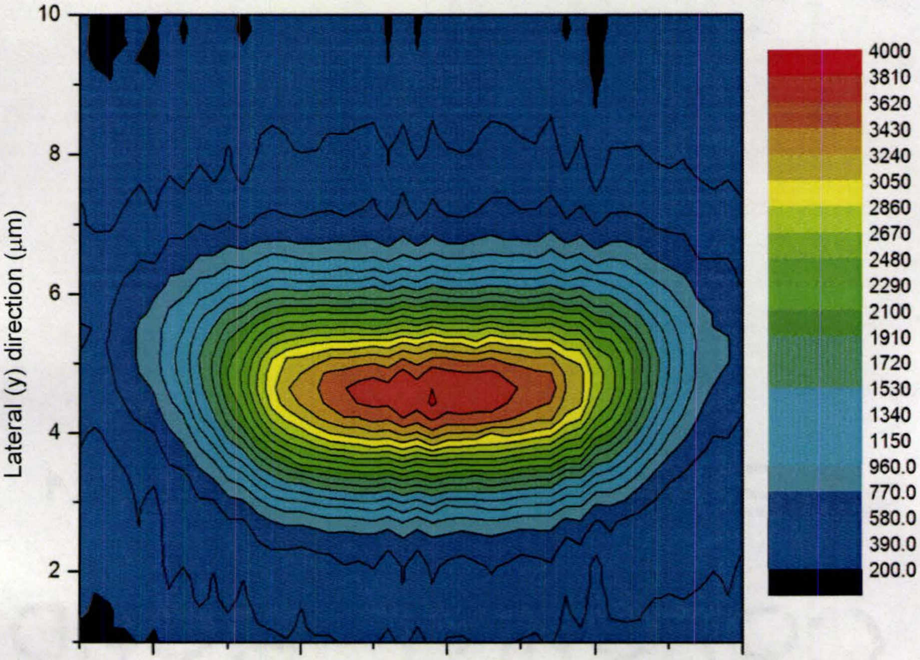
Lateral (y) direction (μm)
Transverse (x) direction (μm)
2
4
6
8
10
4000
3810
3620
3430
3240
3050
2860
2670
2480
2290
2100
1910
1720
1530
1340
1150
960.0
770.0
580.0
390.0
200.0

(c)

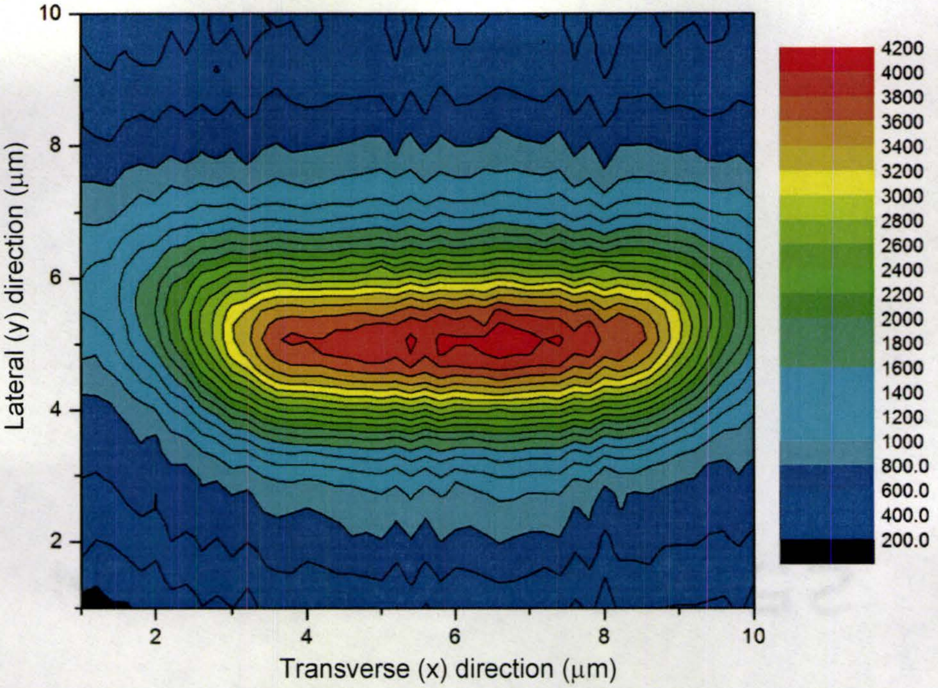

(d)

Fig.C.1 Near field measurement of (a) 3 μm ridge width at 19 mA (b) 4 μm ridge width at 15mA (c) 5 μm ridge width at 17 mA (d) 6 μm ridge width at 16mA. The units for *x* and *y* axes for all figures are micrometer.

Appendix D OCT 2D Images of a Cover Glass Slip

The 2D images are built for a cover glass slip OCT measurement with TD OCT, FD OCT and SOCT respectively. The corresponding deconvolved objects were performed with a Richardson-Lucy blind-decovolution algorithm. The units for x and y axes are the data acquisition number of points.

D.1. 2D image of a cover glass slip with time domain OCT

(a) Image; (b) Blind-deconvolved object with a Richardson-Lucy algorithm.

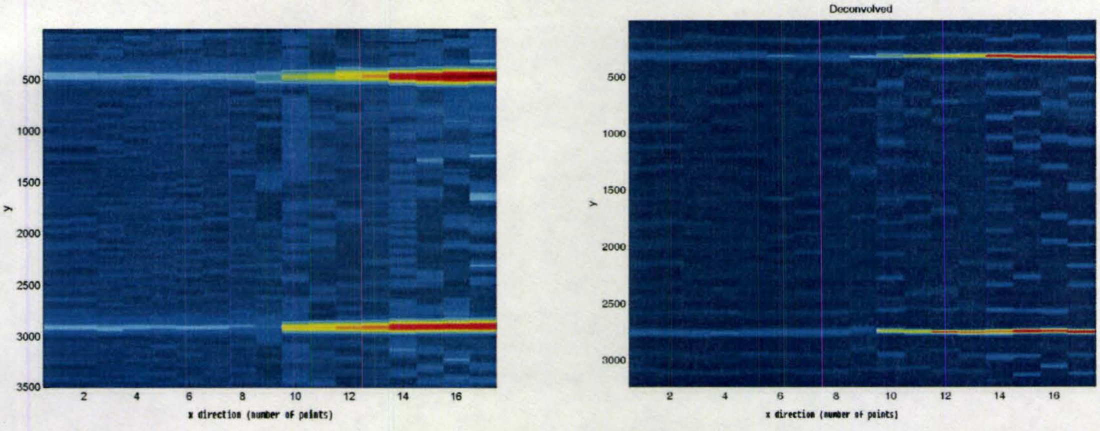

(a) (b)

D.2. 2D image of a cover glass slip with Fourier domain OCT

(a) Image; (b) Blind-deconvolved object with a Richardson-Lucy algorithm

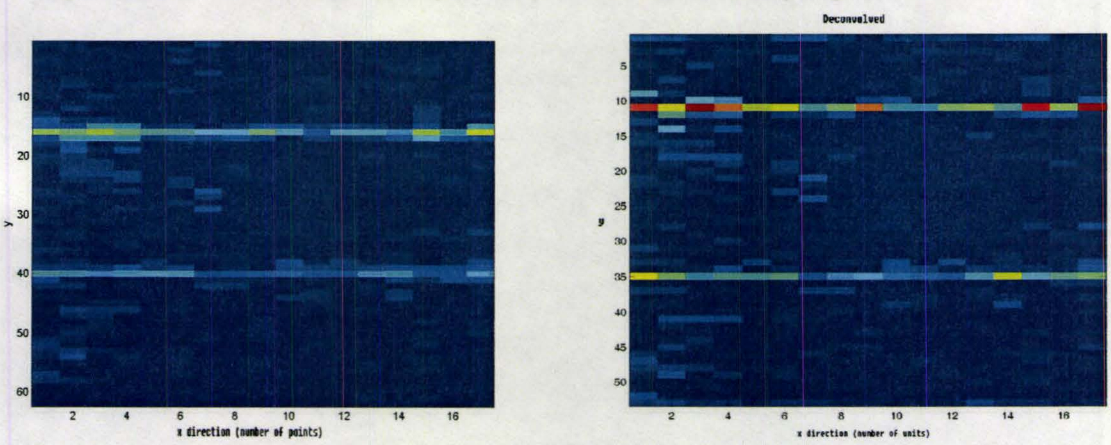

(a) (b)

D.3. 2D image of a cover glass slip with synthesized OCT

(a) Image; (b) Blind-deconvolved object with a Richardson-Lucy algorithm

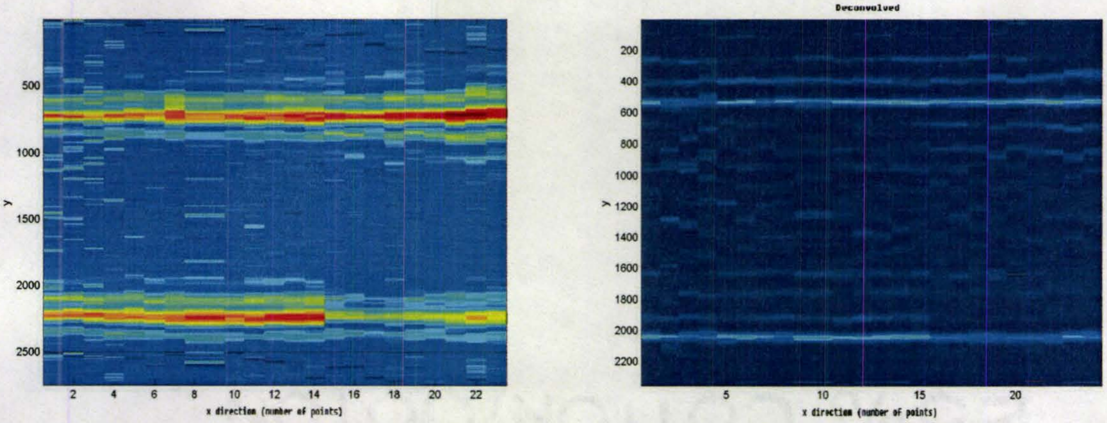

(a) (b)

References:

---

[1] D. Huang, E. Swanson, C. P. Lin, J. S. Schuman, W. G. Stinson, W. Chang, M. R. Hec, T. Hotte, K.Gregory, C. A. Puliafito, and J. G. Fujimoto, "Optical coherence tomography", *Science*, 1991, Vol. 254, pp1178-1181.

[2] R. C. Youngquist, S.Carr and D. E. N. Davies, "Optical coherence-domain reflectometry: A new optical evaluation technique", *Opt. Lett.*, Vol. 22, pp158-160, 1987.

[3] J. G. Fujimoto, M. E. Brezinski, G. J. Tearney, S. A. Boppart, B. Bouma, M. R. Hee, J. F. Southern, E. A. Swanson, "Optical biopsy and imaging using optical coherence tomography", *Nature Medicion*, Vol. 1, No. 9, 1995, pp970-972.

[4] A. F. Fercher, W. Drexler, C. K. Hitzenberger, and T. Lasser, "Optical coherence tomography-principles and applications", *Rep. Prog. Phys.*, Vol. 66, pp239-303, 2003.

[5] Joseph M. Schmitt, "Optical Coherence Tomography (OCT): A Review", *IEEE J. Selected Topics in Quant. Electron.*, Vol. 5, No. 4, pp1205-1215, 1999.

[6] Wolfgang Drexler, "Ultrahigh-resolution optical coherence tomography", *J. Biomed. O*ptics, Vol. 9, pp47-74, 2004.

[7] P. H. Tomlins and R. K. Wang, "Theory, developments and applications of optical coherence tomography", *J. Phys. D: Appl. Phys.*, Vol. 38, pp 2519-2535, 2005.

[8] M. Wirtitsch, O. Findl, R. Menapace, V. Petternell, B. Kiss, C. K. Hitzenberger, A. F. Fercher, and W. Drexler, "Effect of dorzolamide on corneal thickness in humans with low endothelial cell count," *Arch. Ophthalmol. (Chicago),* Vol. 121, pp621-625, 2003.

[9] O. Findl, W. Drexler, R. Menapace, C. K. Hitzenberger, and A. F. Fercher, "High precision biometry of pseudophakic eyes using partial coherence interferometry," *J. Cataract Refractive Surg.* Vol. 24, pp1087–1093, 1998.

[10] W. Drexler, O. Findl, L. Schmetterer, C. K. Hitzenberger, and A. F. Fercher, "Eye elongation during accommodation in humans—differences between emmetropes and myopes," *Invest. Ophthalmol. Visual Sci.,* Vol. 39, pp2140–2147, 1998.

[11] B. E. Bouma, G. J. Tearney, C. C. Compton, and N. S. Nishioka, "High-resolution imaging of the human esophagus and stomach *in vivo* using optical coherence tomography," *Gastrointest Endosc,* Vol.51, pp467–474 2000.

[12] B. E. Bouma, G. J. Tearney, H. Yabushita, M. Shishkov, C. R. Kauffman, D. DeJoseph Gauthier, B. D. MacNeill, S. L. Houser, H. T. Aretz, E. F. Halpern, and I. K. Jang, "Evaluation of intracoronary stenting by intravascular optical coherence tomography," *Heart,* Vol. 89, pp317-320, 2003.

[13] M. W. Jenkins and A. M. Rollins, "Biomedical imaging: OCT images the developing heart in vivo", http://www.laserfocusworld.com/display_article/311587/12/ARCHI/none/Feat/BIOMEDICAL-IMAGING:-OCT-images-the-developing-heart-in-vivo.

[14] K. Kincade, "Time domain OCT brings new vision to dental diagnostic" http://www.laserfocusworld.com/display_article/314417/12/ARTCL/none/News/OPTICAL-COHERENCE-TOMOGRAPHY:-Time-domain-OCT-brings-new-vision-to-dental-diagnostic

[15] I. Schneider, "BIOMEDICAL-IMAGING:-MIT-researchers-obtain-3-D-images-of-living-cell", http://www.laserfocusworld.com/display_article/311574/12/ARCHI/none/News/BIOMEDICAL-IMAGING:-MIT-researchers-obtain-3-D-images-of-living-cell

[16] K. J. Resch, P. Puvanathasan, J. S. Lundeen, M. W. Mitchell, and K. Bizheva, "Classical dispersion-cancellation interferometry", *Optics Express*, Vol.15, No.14, 2007, pp8797-8804.

[17] V. X. D. Yang, M. L. Gordon, B. Qi, J. Pekar, S. Lo, E. S. Yue, A. Mok, B. C. Wilson, I. A. Vitkin, "High speed, wide velocity dynamic range Doppler optical coherence tomography: system design, signal processing, and performance", *Opt. Express.*, Vol. 11, pp794-809, 2003.

[18] M. R. Hee, D. Huang, E. A. Swanson, and J. G. Fujimoto, "Polarization-sensitive low-coherence reflectometer for birefringence characterization and ranging," *J. Opt. Soc. Am. A.*, Vol. 9, pp903–908, 1992.

[19] J. Wang, D. T. Cassidy, "Broadly Tunable, Short External Cavity Diode Laser for Optical Coherence Tomography", *IET Optoelectronics*, Vol. 2 pp46-54, Feb.2008.

[20] M. A. Choma, M. V. Sarunic, C. Yang, J. A. Izatt, "Sensitivity advantage of swept source and Fourier domain optical coherence tomography", *Optics Express*, Sept. 2003, Vol. 11, pp2183-2189.

[21] Stefanie G. Schuman, Ellen Hertzmark, James G. Fujimoto, and Joel S. Schuman, "Wavelength Independence and Interdevice Variability of Optical Coherence Tomography", *Ophthalmic Surg Lasers Imaging*. 2004, Vol. 35, pp316–320.

[22] M. J. Hamp and D. T. Cassidy, "Critical Design Parameters for Engineering Broadly Tunable Asymmetric Multiple-Quantum-Well Lasers," *IEEE J. Quantum Electronics.*, Vol. 36, pp978-983, 2000.

[23] S. C. Woodworth, D.T.Cassidy, and M. Hamp, "Experimental analysis of a broadly tunable InGaAsP laser with compositionally varied quantum wells", *IEEE J. Quantum Electron.*, 2003, Vol. 39, pp426-430

[24] S. C. Woodworth, G. B. Morrison, H. Wang, D. T. Cassidy, "Galerkin Method for calculating valence-band wavefunctions in quantum-well structures using exact envelope theory", *IEEE J. Quantum Electron.*, 2004, Vol. 40, pp222-230

[25] D. T. Cassidy, M. J. Hamp, "Diffractive optical element used in an external feedback configuration to tune the wavelength of uncoated Fabry-Perot diode lasers", *J. Mod. Opt.*, 1999, Vol. 46, pp1071-1078

[26] Takeshi Yamatoya, Shota Mori, Fumio Koyama and Kenichi Iga, "High power GaInAsP/InP strained quantum well superluminescent diode with taperd active region", *Jpn. J. Appl. Phys.*, Sept. 1999, Vol. 38, 1999, pp5121-5122

[27] Liwei Fu, Heinz Schweizer, Yanshen Zhang, Lan Li, Andreas M. Baechle, Stephan Jochum, georg C. Bernatz, and Stefan Hansmann, "Design and realization of high-power ripple-free superluminescent diodes at 1300 nm", *IEEE J. Quantum Eletron.*, 2004, Vol.40, No.9, pp1270-1274

[28] Ching-Fuh Lin and bing-Ruey Wu, "Sequence influence of nonidentical InGaAsP quantum wells on broadband characteristics of semiconductor optical amplifier-superluminescent diodes", *Opt. Lett.*, 2001, Vol. 26, No.14, pp1099-1101

[29] S. C. Woodworth, D. T. Cassidy and M. J. Hamp, "Sensitive absorption spectroscopy by use of an asymmetric multiple-quantum-well diode laser in an external cavity", *Appl. Opt.*, 2001, **40** (36), , pp6719-6724

[30] F. L. Pedrotti and L. S. Pedrotti, "Introduction to Optics", Englewood cliffs, New Jersey: Prentice-Hall, 2007 Chapter 13, pp316~318.

[31] N. Trenado, J. F. Palmier, "An efficient and accurate method for gain spectrum calculations in nonidentical multi-quantum-wells", *IEEE J. Quantum Electron.*, 2002, **38**, pp495-499

[32] H. Wang, D. M. Bruce, D. T. Cassidy, "Gain characteristics of Asymmetric multiple quantum well lasers", *IEEE J. Quantum Eletron.*, 2006, **42** (5), pp464-470

[33] N. Tessler, G. Eisenstein, "Modelling carrier dynamics and small-signal modulation response in quantum-well lasers", *Opt. Quantum Electron.*, 1994, **26**, 1994, pS767.

[34] M. J. Hamp, D. T. Cassidy, B. J. Robinson, Q. C. Zhao, D. A. Thompson, "Nonuniform carrier distribution in asymmetric multiple-quantum-well InGaAsP laser structures with different numbers of quantum wells", *Appl. Phys. Lett.*, 1999, **74** (5),

[35] D.T. Cassidy, "Technique for measurement of the gain spectra of semiconductor diode lasers," *J. Appl. Phys.*, Vol. 56, No. 11, pp3096-3099, 1984.

[36] B. W. Hakki, and T. L. Paoli, "Gain spectra in GaAs double-heterostructure injection laser", *J. Appl. Phys.*, Vol. 46, No. 3, pp1299-1305. 1975

[37] J. W. Goodman, "Statistical Optics", Chapter 7, New York: Wiley, 1985.

[38] A. F. Fercher, W Drexler, C.K. Hitzenberger, and T. Lasser, "Optical coherence tomography – principles and applications*"*, *Rep. Prog. Phys.*, 2003, **66**, pp239-303

[39] A. S. Gerges, T.P. Newson, D.A. Jackson, "Coherence tuned fiber optic sensing system, with self-initialization, based on a multimode laser diode", *Appl. Opt.*, Oct. 1990, **29** (30), pp4473-4480

[40] G. Hausler, M. W. Lindner, ""Coherence radar" and "Spectral radar"-new tools for dermatological diagnosis", *J. Biomedical Opt.*, Jan. 1998, **3** (1), pp21-31

[41] B. P Lathi, "Modern Digital and Analog Communication Systems", Chapter 6, Oxford University Press, 1998.
[42] D.T. Cassidy and L.J. Bonnell, "Trace gas detection with short-external-cavity InGaAsP diode laser transmitter modules operating at 1.58 μm", *Appl. Opt., 1988,* **27**, pp2688-2693
[43] B.F. Ventrudo and D.T. Cassidy, "Interference fringes in the far field of short-external-cavity InGaAsP diode lasers: a method for longitudinal mode control", *Appl. Opt.* 1993, **32**, pp6620-6627
[44] M.A.A Neil, R. Juskaitis, T. Wilson, Z.J. Laczik, "Optimized pupil-plane filters for confocal microscope point-spread function engineering", *Opt. Lett.*, 2000, **25** (4), pp245-247
[45] G. P. Agrawal, N.K. Dutta, "Long-wavelength semiconductor lasers", AT&T Bell Laboratories, Murray Hill, New Jersey, 1986, pp172-193,Chapter 5.
[46] Toru Takayama, Osamu Imafuji, Yasuyuchi, Masaaki Yuri, Akio Yoshikawa, Kunio Itoh, "100-mW High-power Angles-stripe Superluminescent Diodes with a new Real Refractive-Index-Guided Self-Aligned Structure", *IEEE J. Quantum Electron.*, Vol.32, No. 11, Nov. 1996, pp1981-1987.
[47] J. Buus and M. J. Adams, Solid State Electron Devices, Vol. 3, pp189, 1979.
[48] B. Broberg, S. Lindgren, "Refractive index of $In_{1-x}Ga_xAs_yP_{1-y}$ layer and InP in the transparent wavelength region", *J. Appl. Phys.*, Vol.55, No.9, pp3376-3381, 1984.
[49] M. Linnik and A. Christou, "Calculations of optical properties for quaternary III-V semiconductor alloys in the transparent region and above (0.2-4.0eV)", *Physica B.*, Vol. 318, pp140-161, 2002.
[50] S. L. Chuang, "Physics of Optoelectronics Devices", Chapter 7, pp270-273, pp.247-256 for slab waveguide solution, John Wiley & Sons. Inc., 1995
[51] Peter S. Zory, "Quantum Well lasers", Chapter 1, pp52-93, Academic Press Inc., 1993
[52] L.M. Walpita, "Solutions for planar waveguide equations by selecting zero elements in a characteristic matrix", *J. Opt. Soc. Am. A.*, Vol.2, No. 4, pp595-602, 1985
[53] Philip R. Bevington, D. Keith Robinson, "Data reduction and error analysis for the physical sciences", Chapter 6, pp96-114 WCB/McGraw-Hill, 1992.
[54] B. D. Patterson, J. E. Epler, B. Graf, H. W. Lehmann, H. C. Sigg, "A superluminescent diode at 1.3 μm with very low spectral modulation", *IEEE J. Quantum Electron.*, Vol. 30, No. 3, pp703-712, 1994.
[55]G. A. Alphonse, D. B. Gilbert, M. G. Harvey, M. Ettenberg, "High power superluminescent diodes", *IEEE J. Quantum Electron.*, Vol. 24, No. 12, pp2454-2457, 1988.
[56] P. W. Milonni, Joseph H. Eberly, "*Lasers*", Chapter 10, John Wiley & Sons Inc., New York,1988, pp294-300.

[57] S. L. Chuang, 1995, *Physics of Optoelectronic Devices*, (New York, NY: John Wiley & Sons), pp337-373.

[58] G. B. Morrison and D. T. Cassidy, "A Probability-Amplitude Transfer Matrix Model for Distributed-Feedback Laser Structures," *IEEE J. Quantum Electron..*, **36**, pp633-640, 2000.

[59] Toru Takayama, Osamu Imafuji, Yasuyuchi, Masaaki Yuri, Akio Yoshikawa, Kunio Itoh, "100-mW High-power Angles-stripe Superluminescent Diodes with a new Real Refractive-Index-Guided Self-Aligned Structure", *IEEE J. Quantum Electron.*, Vol.32, No. 11, Nov. 1996, pp1981-1987.
[60] L.M.Walpita, "Solutions for planar optical waveguide equations by selecting zero elements in a characteristic matrix", *J. Opt. Soc. Am. A*, 2(4), pp595-602, 1985.
[61] P. R. Bevington, D. K. Robinson, "Data reduction and error analysis for the physical sciences", McGraw-Hill, 2nd edition, Chapter 8, pp156-166.
[62] Peter A. Jansson, "Deconvolution: with applications in spectroscopy", Academic Press, INC, 1984. Chapter 3. pp67-92.
[63] D. A. Fish, A. M. Brinicombe, and E. R. Pike, "Blind deconvolution by means of the Richardson-Lucy algorithm", *J. Opt. Soc. Am. A,* Vol.12, No. 1, pp58-65, 1995
[64] S. H. Yun, G. J. Tearney, J.F. de Boer, N. Iftimia, B. E. Bouma, "High-speed optical frequency-domain imaging", Optics Express, Vol. 11, No. 22, pp2953-2963, 2003.
[65] W. H. Richardson, "Bayesian-based interative method of image restoration", *J. Opt. Soc. Am.*, Vol. 62, pp55-59, 1972.

---

[66] J. M. Schmitt, "Optical Coherence Tomography (OCT): A review", *IEEE J. Selected Topics in Quantum. Electron.*, Vol. 5, No. 4, pp1205-1215, 1999.
[67] M.D. Kulkarni, C. W. Thomas, and J. A. Izatt, "Image enhancement in optical coherence tomography using deconvolution", Electron. Lett., Vol. 33, No. 16, pp1365-1367. 1997
[68] Bocang Qiu, Stewart D. McDougall, Xuefeng Liu, Gianluca Bacchin, John H. Marshm "Design and fabrication of low beam divergence and high kink-free power lasers", IEEE, J. Quantum Electron., Vol. 41, No.9, pp1124-1130, 2005.